Input Site U1414[1]

R.N. Harris, A. Sakaguchi, K. Petronotis, A.T. Baxter, R. Berg, A. Burkett, D. Charpentier, J. Choi, P. Diz Ferreiro, M. Hamahashi, Y. Hashimoto, K. Heydolph, L. Jovane, M. Kastner, W. Kurz, S.O. Kutterolf, Y. Li, A. Malinverno, K.M. Martin, C. Millan, D.B. Nascimento, S. Saito, M.I. Sandoval Gutierrez, E.J. Screaton, C.E. Smith-Duque, E.A. Solomon, S.M. Straub, W. Tanikawa, M.E. Torres, H. Uchimura, P. Vannucchi, Y. Yamamoto, Q. Yan, and X. Zhao[2]

Chapter contents

[1] Harris, R.N., Sakaguchi, A., Petronotis, K., Baxter, A.T., Berg, R., Burkett, A., Charpentier, D., Choi, J., Diz Ferreiro, P., Hamahashi, M., Hashimoto, Y., Heydolph, K., Jovane, L., Kastner, M., Kurz, W., Kutterolf, S.O., Li, Y., Malinverno, A., Martin, K.M., Millan, C., Nascimento, D.B., Saito, S., Sandoval Gutierrez, M.I., Screaton, E.J., Smith-Duque, C.E., Solomon, E.A., Straub, S.M., Tanikawa, W., Torres, M.E., Uchimura, H., Vannucchi, P., Yamamoto, Y., Yan, Q., and Zhao, X., 2013. Input Site U1414. *In* Harris, R.N., Sakaguchi, A., Petronotis, K., and the Expedition 344 Scientists, *Proc IODP,* 344: College Station, TX (Integrated Ocean Drilling Program). doi:10.2204/iodp.proc.344.104.2013
[2] **Expedition 344 Scientists' addresses.**

Background and objectives

The primary objective of Integrated Ocean Drilling Program Expedition 344 was to sample and quantify the material comprising the seismogenic zone of an erosive subduction margin. Fundamental to this objective is an understanding of the nature of the sediment and oceanic crust entering the seismogenic zone, the hydrologic system, and the thermal state of the igneous oceanic crust. Site U1414 (proposed Site CRIS-19A) serves as a secondary reference site on the flank of the subducting aseismic Cocos Ridge.

Site U1414 is located within the 3-D seismic volume along Line 2497 and crossing Line 2562 (Fig. **F1**) and is ~1 km seaward of the deformation front offshore the Osa Peninsula and Caño Island (Fig. **F2**). This site was chosen for multiple reasons. First, a clear seismic record of the plate stratigraphy is present at this site. The seismic section shows a 400 m thick sediment section resting on reflective basement interpreted as Cocos Ridge igneous crust. Second, the sedimentary section is thought to be composed of pelagic and hemipelagic sediments that may record the interval missing at Site U1381. Third, a reflector of interest exists about two-thirds of the way through the sediment column. Finally, this site presents an opportunity to collect igneous basement.

Primary science goals at Site U1414 included (1) documenting the presence or absence of the hiatus observed at Site U1381, (2) documenting the presence or absence of tephras during the 9–11 m.y. hiatus documented at Site U1381, and (3) documenting the alteration state of basement. Finally, because of oblique convergence of subduction at the Middle America Trench, sediments at Site U1414 likely correspond to the sediments now being subducted under seismic Line BGR99-7. Documenting the physical state and water content of these sediments was also important.

Sediment thickness along the inline seismic transect (southwest–northeast) is variable and reflects the relief of the Cocos Ridge basement.

Operations

Transit to Site U1414

After a 5.8 nmi transit from Site U1412, the vessel stabilized over Site U1414 (proposed Site CRIS-19A) at 0015 h on 3 December 2012. The position reference used for dynamic positioning was a

doi:10.2204/iodp.proc.344.104.2013

combination of GPS signals and an acoustic beacon, which was deployed at 0010 h. During the transit, an advanced piston corer (APC)/extended core barrel (XCB) bottom-hole assembly (BHA) was assembled with a nonmagnetic drill collar and the drill string was lowered to 1858 meters below rig floor (mbrf).

Hole U1414A

Upon arrival, the drill string was lowered to just above the seafloor, and Hole U1414A (8°30.2304′N, 84°13.5298′W; 2459 m water depth) was spudded at 0805 h on 3 December 2012. Cores 344-U1414A-1H through 22H were taken with the APC from 0 to 200.1 meters below seafloor (mbsf) (Table T1). Nonmagnetic core barrels and the FlexIT orientation tool were used with all APC cores. Advanced piston corer temperature tool (APCT-3) formation temperature measurements were taken with Cores 3H, 5H, 7H, and 9H. The coring system was switched to the XCB system after having to drill over Core 22H. Cores 23X–35X were taken with the XCB from 200.1 to 311.9 mbsf, by which point penetration rates and recovery had decreased drastically. The decision was made to stop XCB coring, drop a free-fall funnel (FFF), change the XCB coring assembly to a rotary core barrel (RCB) assembly, and reenter Hole U1414A. The hole was swept with a 30 bbl high-viscosity mud sweep, and the bit was pulled back to 113.7 mbsf. The FFF and subsea camera were deployed at 0025 h. The remainder of the drill string was pulled from the hole while the camera recorded the position of the FFF on the seafloor and the bit as it cleared the FFF. The drill string was then raised to the surface, with the bit clearing the rotary table at 0740 h on 5 December. An RCB BHA was assembled with a new bit, and the BHA was lowered to just above the seafloor by 1415 h. The subsea camera was deployed, and after searching for the FFF for ~1.5 h, Hole U1414 was reentered at 1543 h. The bit was slowly lowered into the hole without encountering any obstruction, and coring resumed. RCB Cores 36R–44R recovered sediment from 311.9 to 374.6 mbsf. Basement was contacted with Core 45R at ~375.25 mbsf. Coring continued through Core 63R at 471.6 mbsf until coring time expired.

In preparation for logging, the hole was swept clean with mud and the bit was released. The end of the drill string was set at 96 mbsf, and the logging tools were rigged up. The first logging run was with the triple combination (triple combo)–Ultrasonic Borehole Imager (UBI) tool string and reached 421 mbsf, where it encountered an obstruction. The second logging run was with the Formation MicroScanner (FMS)-sonic tool string, and it reached the same depth. Logging activities were completed by 1200 h on 10 December. The drill string cleared the rig floor at 1955 h on 10 December, ending Site U1414. The vessel began the 95 nmi transit to Puntarenas, Costa Rica, at 2015 h. First line ashore was at 0502 h on 11 December 2012, ending Expedition 344.

A total of 63 cores were recovered at this site: 22 APC, 13 XCB, and 28 RCB. The APC cored interval was 200.1 m, with 206.2 m recovered (103%). The XCB cored interval was 111.8 m, with 94.1 m recovered (84%). The RCB cored interval was 159.7 m, with 84.5 m recovered (53%). Overall recovery for Site U1414 was 81%. Total time spent on Site U1414 was 191.0 h or 8 days.

Lithostratigraphy and petrology

Site U1414 was drilled to investigate the lithostratigraphy and pore water of the sedimentary sequence on top of the oceanic basement and in the uppermost portions of the underlying igneous basement. In Hole U1414A, 375.25 m of sediment and 96.35 m of oceanic basement were recovered. The cored interval was divided into three major sedimentary units with four subunits and eight igneous basement units (Fig. F3; Table T2). Overall core recovery was 86%: 96% for APC coring, 86% for XPC coring, and 34% for RCB sediment coring.

The top of Hole U1414A is characterized by a predominantly monotonous sequence of soft, light greenish gray hemipelagic silty clay to clay. The uppermost part of Unit I (Subunit IA) contains several thin sand layers, whereas calcareous nannofossils gradually increase in the lower part (Subunit IB). Unit I contains terrigenous material (lithic fragments, glass shards, and minerals) that decreases with depth. Biogenic material such as foraminifers and radiolarians is abundant. Tephra layers make up ~1% of Unit I and are distributed into 16 well-sorted, discrete tephra horizons. The Unit I/II boundary at 145.34 mbsf (Section 344-U1414A-17H-1, 94 cm) is marked by a change from greenish gray nannofossil-rich clay sediment to brownish to whitish nannofossil-rich calcareous ooze.

Unit II (145.34 mbsf; Sections 344-U1414A-17H-1, 94 cm, to 35X-CC, 29 cm) is a 164.03 m thick, moderately consolidated, white to dark grayish to yellowish brown clayey to silty interval that is divided into two subunits. Unit II is generally composed of nannofossil-rich calcareous ooze and variable amounts of sponge spicules, foraminifers, and diatoms. Subunit IIA (145.34–200.01 mbsf; Sections 344-U1414A-17H-1, 94 cm, to 22H-CC, 30 cm) is dominated by calcareous nannofossil ooze, whereas Subunit IIB is characterized by meter-scale alternating calcareous nannofossil ooze and biosilica-rich calcareous ooze.

Tephra layers comprise ~1% of the unit and are found throughout Unit II. Ten dark brown to gray and sometimes light gray tephra horizons are preserved as discrete layers or individual and/or layered ash pods.

Unit III is a 65.88 m thick interval between 309.37 and 375.25 mbsf (Sections 344-U1414A-35X-CC, 29 cm, to 45R-1, 65 cm). It is a sequence of lithified, calcareous, and siliceous cemented silt- and sandstone with well-preserved original sedimentary structures such as bedding and bioturbation. The biogenic components in this unit have been lost, most likely because of diagenetic remobilization. Tephra layers and pods comprise <1% of this interval, and nine dark brown layers are recorded here.

Based on preliminary descriptions of igneous basement at Site U1414, one thin flow unit (4) and six massive flow units (1–3, 5, 6, and 8) separated by intercalated sediment (Unit 7) were identified. Subunits were defined based on changes in grain size, vesicle abundance, textural relationships, and phenocryst variation. Unit distribution is summarized in Figures F3 and F4, with greater detail on definitions in "Lithostratigraphy and petrology" in the "Methods" chapter (Harris et al., 2013b). Detailed textural description, mineralogy, and their relationships throughout basement were not possible on the ship because of time constraints that prevented analyses such as thin sections, inductively coupled plasma spectroscopy analyses, and X-ray diffraction (XRD). However, thin sections were made and analyzed following the expedition, and the results are incorporated into this report.

Description of units

Cores recovered from Hole U1414A are divided into three sedimentary and eight basement lithostratigraphic units (Fig. F3; Table T2). These units comprise the 375.25 m cover sequence above igneous basement and 96.35 m of basalt.

Unit I

Interval: Sections 344-U1414A-1H-1, 0 cm, to 17H-1, 94 cm
Thickness: 145.34 m
Depth: 0–145.34 mbsf
Age: early Pleistocene to recent
Lithology: soft silty clay with sand to calcareous nannofossil-rich clay

Unit I is massive dark greenish gray soft (silty) clay sediment with variable proportions of clay, silt, and sand and variable concentrations of calcareous nannofossils. Unit I is divided into two subunits based on compositional changes. Subunit IA contains centimeter-sized, normally graded sand layers and a relatively high component of terrigenous material, mainly lithic fragments, quartz, and feldspar (Fig. F5). Subunit IB contains abundant calcareous nannofossils within the silty clay, whereas terrigenous components such as quartz and feldspar are much diminished relative to Subunit IA (Fig. F6). The 16 disseminated tephra layers in Unit I range between 1 and 71 cm in thickness (Fig. F7).

Subunit IA (0.00–78.3 mbsf)

In addition to greenish gray silty clay, Subunit IA contains centimeter-sized, normally graded sand layers (Fig. F5). The sandstone layers contain abundant foraminifers that are very poorly consolidated. Smear slides, together with XRD analyses, indicate a large quantity of terrigenous material dominated by lithic fragments, quartz, and feldspar but also common to abundant amphibole, pyroxene, chlorite, glauconite, and chert. Biogenic components such as radiolarians, sponge spicules, foraminifers, and diatoms are common. Four mostly gray to dark gray tephra layers, ranging in thickness from 1 to 68 cm, were found in Subunit IA, and they appear to become more common in the sediment just above the boundary with Subunit IB.

Subunit IB (78.3–145.34 mbsf)

Subunit IB consists of light greenish gray calcareous nannofossil-rich silty clay (Fig. F6). Smear slides and XRD analyses show that abundances of lithic fragments, quartz, and feldspar decrease with depth. Components such as chert, chlorite, pyroxene, amphibole, opaque minerals, calcite, glauconite, and glass are also much reduced compared to Subunit IA. In contrast, biogenic material and fragments such as radiolarians, foraminifers, and sponge spicules become more dominant in the matrix. Twelve well-sorted, light gray to gray tephra layers ranging in thickness from 1 to 10 cm are present in normally graded layers.

Unit II

Interval: Sections 344-U1414A-17H-1, 94 cm, to 35X-CC, 29 cm
Thickness: 164.03 m
Depth: 145.34–309.37 mbsf
Age: late to early Miocene
Lithology: nannofossil calcareous ooze with sponge spicules

Unit II is distinguished from Unit I by its abundant biogenic content, also reflected in the change from dark greenish gray to light greenish gray or white and yellowish brown sediment color. The sediment contains >70% biogenic components, such as spicules,

diatoms, radiolarians, and nannofossils, but calcareous components decrease with depth. The abundance of clay, siliceous biogenic material, and silica cement (opal) partly increases with depth, but from Core 344-U1414A-31R downward, only diagenetic silica is observed in the smear slides. Mineral components that occur in trace amounts include feldspar, pyroxene, calcite, and opaque minerals. Ten tephra horizons, ranging from 1 to 49 cm in thickness, are soft to moderately lithified, show normal gradation from medium sand to silt, and occur as discrete layers, individual ash pods, or ash pod layers. The glass shards are mainly transparent, and preliminary observations suggest they are felsic in origin and contain heavy mineral assemblages dominated by amphibole and biotite.

Subunit IIA (145.34–200.01 mbsf)

Subunit IIA consists of strongly bioturbated, massive, light green calcareous ooze (Fig. **F8**). Abundant pyrite is disseminated throughout the sediment, and the most common detrital grains are quartz and feldspar. Common discoloration indicative of glauconite and sometimes glauconite agglomerated grains can also be found throughout Subunit IIA. XRD analyses of Subunit IIA indicate this subunit contains the last significant occurrences of smectite and zeolite, specifically heulandite and clinoptilolite, before they become absent in the underlying sedimentary sequences. Five tephra layers are distributed throughout the sedimentary interval.

Subunit IIB (200.01–309.37 mbsf)

Subunit IIB consists mainly of dark grayish greenish to yellowish brown, soft to hardened silty clayey calcareous ooze alternating with calcareous ooze containing abundant sponge spicules (Fig. **F9**). The amount of foraminifers is variable in both types of ooze. Detrital grains (quartz and plagioclase), sponge spicules, radiolarians, diatoms, and zeolite and smectite gradually fade out. Although the biogenic material (radiolarians and nannofossils) shows evidence of recrystallization during the uppermost tens of meters of Subunit IIB, diagenetic opal increases remarkably. Five mostly dark gray to reddish gray tephra layers, ranging in thickness from 1 to 49 cm, were found in Subunit IIB.

Unit III

Interval: Sections 344-U1414A-35X-CC, 29 cm, to 45R-1, 65 cm

Thickness: 65.88 m

Depth: 309.37–375.25 mbsf

Age: early Miocene

Lithology: calcareous and siliceous cemented silt- and sandstone

The boundary between Units II and III is marked by a noticeable increase in the lithification state of the sediment, a change to a dark reddish brown color, and the occurrence of preserved sedimentary structures, such as bedding and bioturbation, and deformational features like foliation and faults (Figs. **F10, F11**). The matrix of the strongly lithified calcareous and siliceous (chert?) silt- to sandstone is replaced by cement, and the sediment is often crosscut by calcite veins. Bedding and foliation planes are also filled by calcite, although foliation is evident from the flow of matrix around (siliceous) clasts. Biogenic material is absent. The main mineralogic components appear to be the recrystallized sedimentary components of former silt and sandstones. Nine tephra horizons, ranging from 2 to 11 cm in thickness, are mostly lithified, show normal gradation from medium sand to silt, and occur as discrete layers, individual ash pods, or ash pod layers. Next to some tephras dominated by brownish glass shards, the glass shards in the majority of tephras are mainly transparent with a high amount of pyrite between the shards and growing on the glass shard surfaces, making the entire tephra layer dark gray to black. In Section 344-U1414A-42R-CC, a sharp inclined contact to completely lithified limestone breccia made out of centimeter-sized clasts is nicely preserved (Fig. **F12**). Apart from dolomite grains, rare pyrite, and other chert-like components, smear slide observations and XRD analyses do not show evidence of other detrital or biogenic components.

Tephra layers

Evaluating whether volcanism shut down because of the arrival of the Cocos Ridge and how volcanism evolved in Central America was a major goal at Site U1414; thus, recovering the tephra records between the mid- to late Pleistocene and mid-Miocene that were missing at Site U1381 (see **"Paleontology and biostratigraphy"** in the "Input Site U1381" chapter [Harris et al., 2013a]) was important. Onboard biostratigraphic results (see **"Paleontology and biostratigraphy"**) indicate that sediment cored within this time interval was recovered, along with ~20 felsic tephra layers. These tephra layers will give new insights into Central American volcanism during this time period.

A total of 35 intercalated tephra layers are recognized throughout Hole U1414A. Unit I contains 16 well-defined tephras, Unit II has 10 tephra layers, and Unit III contains 9 tephras. Individual tephra layers range in thickness from 1 to 71 cm. Unconformable and/or inclined bedding is rare. Most tephra layers are well sorted and have a sharp basal contact to

underlying sediment but a gradual transition with overlying ash-bearing sediment. Below Subunit IIA, tephra layer horizons become more disseminated and smeared because of drilling disturbance. Normal grading is commonly observed in both the tephra horizons and the larger ash pods. Some tephra layers are well lithified (Figs. **F13, F14**). In some cores, localized bioturbation is observed at tephra layer boundaries.

Compositions of the 36 identified tephra layers are variable and show mainly gray to pinkish and some gray to brown-black colors. Nearly all tephra layers are dominated by transparent glass shards that are fresh with few signs of alteration and by pumiceous clasts. Devitrification structures within glass shards increase with depth, reflecting differing levels of alteration. In Unit III, pyrite can be identified as an alteration product growing on and between the transparent glass shards. Grain size ranges from very fine to coarse ash (up to several millimeters in size). Mineral assemblages consist of plagioclase, pyroxene, hornblende, and biotite. Plagioclase is the dominant phenocryst phase, but some tephras are dominated by amphibole and biotite.

X-ray diffraction analysis

Preliminary XRD analysis of sediment samples from Hole U1414A suggests that there are gradational variations from one lithostratigraphic unit to another (Figs. **F14, F15**).

X-ray diffractograms of Unit I indicate that the major mineral components are phyllosilicates, including chlorite and smectite, plagioclase, and quartz. Calcite, zeolite (heulandite and laumontite), amphibole (hornblende), and pyrite peaks are also present. Relative peak intensities of silicates decrease throughout Subunit IB, whereas those of calcite increase. Glauconite is present in some samples in Subunit IB, mainly in the lower part of the unit.

Samples from Unit II produce spectra dominated by calcite. Chlorite and amphibole are not detected in the unit. Relative peak intensities of quartz, plagioclase, zeolite, and smectite decrease throughout Subunit IIA, but these minerals are absent in Subunit IIB. In the lower part of Subunit IIB, calcite is the only significant mineral and is associated with silica (most likely opal) and minor pyrite. Zeolite (clinoptilolite type) has been identified, sometimes in large amounts, in few samples.

X-ray diffractograms of Unit III indicate the major mineral component is dolomite. It is associated with calcite, silica (most likely opal), and zeolite (clinoptilolite type).

Igneous basement

In Hole U1414A, igneous basement was recovered from 375.25 to 471.6 mbsf (0 to 96.4 meters subbasement [msb]), of which 61.6 m was recovered (66%).

Recovered basement broadly comprises aphyric to highly phyric massive basaltic flows and thin flows that are divided into seven units, with one additional unit of intercalated calcareous sandstone. Igneous lithologic units were defined based on changes in lava morphology, flow boundaries, texture, and phenocryst occurrence. The distribution of lithologic units is summarized in Figure **F4.** Greater detail regarding how units are defined may be found in **"Lithostratigraphy and petrology"** in the "Methods" chapter (Harris et al., 2013b).

Lithostratigraphy

Massive and thin sheet flow units (Units 1–6 and 8) were divided based on changes in phenocryst abundance, the presence of olivine, grain size, vesicle abundance, and the presence of chilled margins. Vesicle infill is described in **"Basement alteration."** Unfortunately, actual contacts between flows were not recovered. Within a given unit, the lack of chilled margins or structures associated with rapid cooling or separate flows (sharp textural changes), together with textural similarities above and below unrecovered intervals, was interpreted as indicating a continuous individual flow.

Unit 1, from Section 344-U1414A-45R-1, 65 cm (375.25 mbsf), to 46R-2, 124 cm (378.74 mbsf), is a 3.5 m thick massive basaltic lava flow that ranges from sparsely phyric to moderately phyric with a groundmass that consists of plagioclase, clinopyroxene, Fe-Ti oxides, and ~3% olivine. Textures observed include intersertal and intergranular. Grain size ranges from cryptocrystalline to microcrystalline, and cryptocrystalline groundmass is restricted to mesostasis between plagioclase and clinopyroxene grains (intersertal). Although intersertal texture occurs throughout Unit 1, it is most prevalent near the top and bottom. Vesicles occur discretely throughout Unit 1 but are least abundant in the central portion (Section 344-U1414A-45R-2). Phenocrysts (in increasing order of abundance) include rare olivine, clinopyroxene, and plagioclase and range in size from 0.1 to 0.7 mm. Phenocrysts are most abundant in the uppermost 40 cm (10% by volume) and lowermost 30 cm (1.5% by volume) of Unit 1. Subunits 1a and 1b were defined by the relative paucity of phenocrysts (~0.1%–2% abundance) below 375.5 mbsf. Chilled margins within a rubble interval at 378.74 mbsf define the bottom of Unit 1.

Unit 2, from Section 344-U1414A-46R-2, 125 cm (379.04 mbsf), to 49R-2, 54 cm (395.94 mbsf), is a 16.9 m thick massive basaltic lava flow. Groundmass composition is similar to Unit 1, with phenocryst abundances that range from aphyric to porphyritic. Texture throughout Unit 2 is typically massive and intersertal but also includes vesicular, subophitic, and intergranular. Variolitic and glassy textures were observed in the uppermost 5 cm of Unit 2. Vesicle abundance varies from absent to 30% vesicles within interval 344-U1414A-47R-1, 13–97 cm, and is highest in the upper 8 m of Unit 2. Phenocrysts include olivine, clinopyroxene, and plagioclase and range in size from 0.1 to 3 mm. Phenocryst abundance broadly increases from 1% at the top of Unit 2 to 55% within Section 344-U1414A-48R-4 but then sharply decreases to ~2% overall abundance at the bottom of Unit 2. Subunits 2a–2c were broadly defined based on the change from sparsely phyric (Subunit 2a), aphyric to sparsely phyric and vesicular (Subunit 2b), to fine-grained highly phyric to porphyritic and sparsely vesicular (Subunit 2c). Upper and lower contacts were not recovered; however, a chilled margin observed at the bottom of Subunit 2c is inferred to represent the bottom of Unit 2.

Unit 3, from Section 344-U1414A-49R-2, 54 cm (395.94 mbsf), to 51R-2, 114 cm (405.9 mbsf), is a 9.69 m thick massive flow that exhibits intersertal, hypocrystalline, and seriate textures. In addition, intergranular texture was observed in thin section. Phenocryst abundance ranges from sparsely phyric to aphyric and consists of clinopyroxene and plagioclase. Overall phenocryst abundance decreases toward the middle of Unit 3 (Section 344-U1414A-50R-2; 400.9 mbsf). A slight increase in plagioclase phenocryst size and abundance is observed toward the bottom of Unit 3. Olivine is absent from Unit 3. Vesicles are rare (0.2% by volume of core) throughout and absent in the central portion of Unit 3 (396.71–401.91 mbsf). The upper and lower contacts of Unit 3 were not recovered.

Unit 4 (Sections 344-U1414A-51R-3, 0 cm, to 51R-1, 91 cm; 405.9–409.41 mbsf) is a 3.51 m thick "thin" flow that exhibits porphyritc texture throughout. Unit 4 is microcrystalline to fine grained with a groundmass that comprises plagioclase, clinopyroxene, and Fe-Ti oxides. Intersertal, seriate, and hypocrystalline textures are observed in thin section. Phenocrysts make up ~30% of the groundmass and consist of plagioclase (2.5 mm in size; 23% of groundmass) and clinopyroxene (0.8 mm in size; 7% of groundmass). Olivine is absent from both the phenocrysts and groundmass. Vesicle abundance ranges from 1% in the top of Unit 4 (Section 344-U1414A-51R-3) to 0.1% in the lowermost 1 m of Unit 4. No contacts were recovered.

Unit 5 (Sections 344-U1414A-52R-1, 91 cm, to 54R-5, 83 cm; 409.41–423.87 mbsf) is defined as a 14.46 m thick massive basaltic lava flow. Groundmass grain size is microcrystalline and comprises plagioclase, clinopyroxene, Fe-Ti oxides and ~3% olivine. Groundmass textures observed in thin section include intersertal, seriate, subophitic, and intergranular. Phenocryst abundance ranges from 0.6% to 1.3% (sparsely phyric) and phenocrysts comprise olivine (in Core 344-U1414A-54R), clinopyroxene, and plagioclase. Phenocryst size and abundance gradually increase throughout Unit 3. An isolated piece in interval 344-U1414A-54R-1, 0–11 cm, comprises 30% phenocrysts and exhibits textures similar to Unit 4; thus, it has been interpreted as a dropstone from the above unit. Vesicles are rare in Unit 5, and overall vesicle abundance decreases from 0.1% to 0.05% from top to bottom, respectively. The upper and lower unit contacts were not recovered.

Unit 6 (Sections 344-U1414A-55R-1, 0 cm, to 58R-1, 10 cm; 423.87–437.7 mbsf) is a 13.83 m thick massive basaltic lava flow composed of plagioclase, clinopyroxene, and Fe-Ti oxides arranged in a groundmass of variable textures. Textures observed in hand specimen and thin section include intersertal, intergranular, and seriate in Section 344-U1414A-55R-1 to porphyritic intergranular in the center of Unit 6 (424.42–429.91 mbsf) and seriate holocrystalline massive at the bottom of Unit 6 (429.91–437.69 mbsf). Phenocrysts include clinopyroxene and plagioclase (with plagioclase most abundant), and their abundance varies from 1.6% at the top of Unit 6 (423.87 mbsf) to 25% between 427.9 and 429.91 mbsf. Between 429 and 437.7 mbsf, phenocryst abundance decreases to 0.5%. Olivine is absent in both phenocrysts and groundmass. Vesicles at the top of Unit 6 (Section 344-U1414A-55R-1) make up 40% by volume of recovered material; however, their abundance rapidly decreases below 424.29 mbsf to 2% and then gradually falls to 0.5% at the bottom of Unit 6. Unit contacts were not recovered; however, a chilled margin observed at 437.6 mbsf (interval 344-U1414A-58R-1, 0–2 cm) is inferred to represent the base of the lava flow.

Unit 7 (Sections 344-U1414A-58R-1, 10 cm, to 58R-2, 33 cm; 437.7–439.37 mbsf) is a partially recrystallized intercalated calcareous silty sandstone with 5%–10% baked benthic foraminifers. Layered schlieren of greenish sandstone and reddish calcareous siltstone and rare clay horizons are observed. Unit 7 is partially to strongly foliated with a preferred orientation observed within the groundmass. Normal faults, present at the bottom of Section 344-U1414A-58R-1, are filled with carbonate veins. The lowermost 10 cm of Unit 7 is silicic in composition and

exhibits relatively strong recrystallization compared to the upper and middle portion of Unit 7. No unit contacts were recovered.

Unit 8 (Sections 344-U1414A-58R-2, 32 cm, to 63R-4, 29 cm; 439.37–466.24 mbsf) is at least 26.87 m thick and is defined as a massive basaltic lava flow. Texturally, Unit 8 ranges from massive, spherulitic in the uppermost 8 cm to intersertal, seriate, subophitic, and intergranular in the remainder of Unit 8. Grain size in the uppermost 17 cm is cryptocrystalline but then grades to microcrystalline (439.54 mbsf) and fine grained by 461.9 mbsf. Clinopyroxene and plagioclase phenocryst abundance is variable (0%–8%). Two intervals (439.45–451.42 and 457.06–465.95 mbsf) within Unit 8 exhibit increased phenocryst abundances of 1%–3% and 3%–8%, respectively. Olivine is observed as a phenocryst phase in Section 344-U1414A-62R-1, 6 cm (457.03 mbsf). Large "megacrysts" of plagioclase as large as 20 mm are observed between 457 and 464.75 mbsf. Within Unit 8, vesicle abundance varies from 0% to 15%. Vesicle abundance tends to be higher in intervals that exhibit relatively low phenocryst abundance. A chilled margin with devitrified glass observed at the top of Unit 8 is inferred to represent the flow top, and immediately below the glassy margin is 47 cm of in situ basaltclastic breccia. No other contact was observed below the breccia. Unit 8 is most likely thicker because drilling stopped at 466.24 mbsf because of time constraints.

Petrology

All basement units at Site U1414 were divided into massive lava flows, one thin flow, and one intercalated sediment. A total of 19 thin sections were selected for petrographic analysis. The thin section images are available under Images in the Laboratory Information Management System (LIMS) database (**web.iodp.tamu.edu/UWQ/**). The mineralogy of the thin flow and massive flow units at Site U1414 (Units 1–6 and 8) is typical for seafloor basalt. Units 1, 2, 4, 5, and 8 contain olivine within their groundmass and phenocrysts. However, because the majority of olivine is completely replaced by secondary minerals (saponite/smectite), identification often relied on the identification of six-sided crystal outlines. For each igneous unit, the variation in texture, principal igneous textures, and distribution of mineralogy, where recovered, are interpreted to relate to the variation in texture associated with cooling rates and the relative position within a cross section of an individual lava flow. An example could be the central portion of a lava flow, where relatively slow cooling rates permit the formation of larger crystals (coarser groundmass) than crystals formed near the flow boundary that cool rapidly. Figure **F16** demonstrates the relationship between the abundance of phenocrysts and vesicles with units in Hole U1414A. Basalt within each flow unit may be broadly termed flow top, flow center, and flow base, an example of which is shown in Figure **F17.**

Recovered basalt inferred to be near or at the flow top of each unit in Hole U1414A typically exhibits the following features:

1. Grain size ranges from cryptocrystalline to microcrystalline.
2. Groundmass textures typically observed include intersertal, variolitic, glassy, spherulitic, and seriate.
3. Phenocryst abundance at the tops of Units 2, 3, 5, 6, and 7 ranges from 0% to 1.6%. Phenocrysts may be composed of prismatic-short plagioclase, subhedral clinopyroxene, and olivine (where present; see **"Phenocryst summary"** for further details). The uppermost portions of Units 1 and 4 exhibit high abundances of phenocrysts (10% and 30%, respectively).
4. Highest vesicle abundance is typically within the upper portion of each unit.

The flow centers for each unit in Hole U1414A are characterized by the following features:

1. Grain size ranges from microcrystalline to fine grained.
2. Groundmass textures include massive, intersertal, intergranular, porphyritic, hypocrystalline, and seriate.
3. Phenocryst abundance ranges from 0.1% to 55%. With the exception of Units 1 and 4, the center of each flow contains the highest abundance of phenocrysts.

Basalt recovered from intervals inferred as being near or in the lowermost portion of the flow typically exhibit the following features:

1. Grain size ranges from cryptocrystalline to microcrystalline.
2. Groundmass textures include holocrystalline, intersertal, and intergranular.
3. Phenocryst abundance is between 0.3% and 1.3%.

Groundmass summary

Basaltic groundmass at Site U1414 varies from hypocrystalline to holocrystalline and is composed primarily of plagioclase and clinopyroxene with minor accessory Fe-Ti oxides and olivine. Plagioclase typically occurs as microlaths, microlites, and acicular crystals. The range of groundmass composition for each igneous unit is given in Table **T3.** However, because composition ranges are based on a limited number of thin sections, further detailed study is

required to resolve the compositional variation of Site U1414A basement. Plagioclase is the most common crystalline phase, comprising between 44% and 63% of the groundmass. Clinopyroxene comprises 14% and 31% of the groundmass and occurs as interstitial growths between plagioclase. Microlaths, microlites, and aggragates of clinopyroxene are common. Anhedral to subhedral microcrysts of olivine that range from partially altered to completely replaced are occasionally present. We estimate olivine to range from 0.1% to 8.6% in abundance. However, these abundance estimates should be treated with caution because of the uncertainty introduced by the extensive replacement of olivine. Mesostasis textures include hyalophitic and intersertal and are present throughout the basement. Spherulitic, variolitic, and glassy textures are rare but present. Almost all mesostasis is typically subject to alteration, resulting in a patchy texture when observed in thin section and hand specimen. Secondary minerals within the groundmass include saponite, smectite, pyrite, rare carbonate, and, in Sections 344-U1414A-48R-4 and 49R-1, rare chlorite. Primary magmatic opaque abundance ranges from 4.2% to 36.2%. Vesicles are typically filled with secondary assemblages (see **"Basement alteration"**).

Phenocryst summary

Phenocrysts at Site U1414 consist of, in order of increasing abundance, olivine, clinopyroxene, and plagioclase (Fig. **F18**). The majority of phenocrysts range in size from 0.1 to 3 mm; however, very large megacrysts of plagioclase as long as 20 mm are present in Unit 8. Plagioclase typically exhibits complex zoning and twinning patterns and may include multiple small inclusions (tecoblasts) within the cleavage planes. Plagioclase can be skeletal within cryptocrystalline and glassy intervals. Minor alteration within cracks and along phenocryst edges is common and ranges from 0% to 15%. Replacement minerals include saponite and smectite. Clinopyroxene, present throughout Hole U1414A, is typically subhedral and smaller than plagioclase, and it typically ranges from 0.1 to 2.5 mm in size. However, between Sections 344-U1414A-48R-4 and 49R-1, larger 5–6 mm clinopyroxene phenocrysts are observed. Crystals are typically anhedral to subhedral, with simple basal twining present throughout. Clinopyroxene is typically intergrown with plagioclase and often occurs as subophitic crystals around plagioclase. Alteration of clinopyroxene phenocrysts varies from 0% to 40%. Replacement minerals include saponite and smectite, and rare chlorite is observed partially replacing clinopyroxene in Sections 344-U1414A-48R-4 and 49R-1. Olivine is present in Units 1, 2, 4, 5, and 8, and its abundance (as a phenocryst phase) varies from 0% to 6.1%. Olivine is almost always replaced by secondary minerals, including saponite and smecite. Rare chlorite is observed partially replacing olivine in Sections 344-U1414A-48R-4 and 49R-1. As indicated earlier, their identification relied on their crystal morphology and textural relationships with surrounding minerals.

Basement alteration

All basement rocks at Site U1414 have been subjected to alteration by interaction with either seawater or modified "hydrothermal" fluids. Alteration varies from slight to high. Basement alteration at Site U1414 is characterized by

- Partial replacement of groundmass mineralogy,
- Partial to complete replacement of phenocrysts by secondary mineral assemblages,
- Fracture filling by secondary minerals to form veins,
- Formation of halos by emplacement of secondary minerals replacing primary phases,
- Partial to complete filling of vesicles with secondary minerals, and
- Brecciation.

An example of each alteration type observed at Site U1414 is shown in Figure **F19.** Macroscopic and microscopic observation of alteration distribution implies an overall slight to moderate alteration intensity in the groundmass, with more intense alteration concentrated around veins and vesicles. Alteration assemblages include saponite, smectite, carbonate, silicates, and sulfides. Zeolite and chlorite are rare.

Only one XRD analysis of secondary clay minerals was made during Expedition 344; thus, most mineralogical descriptions rely on macroscopic and microscopic visual observation only. As a result, the term "smectite" has been used in place of a more definitive mineralogical definition. Future detailed clay mineral identification will be needed to resolve the clay mineral phases at Site U1414, and it is likely that a continuum of expanding clay minerals are present. We therefore describe saponite and smectite together. Saponite is present in Cores 344-U1414A-45R through 53R (374.6–418.2 mbsf). Saponite coloration ranges from black to greenish brown to greenish gray. In microscopic observation, it is typically pale brown. Smectite is observed starting with Core 344-U1414A-46R (376.4 mbsf); however, it is interpreted as ubiquitous from Core 344-U1414A-53R (413.3 mbsf) to the bottom of the hole. Smectite color ranges from black to olive-green to dark green-gray in macroscopic observation and green-brown to green-gray in microscopic observation. Slight to moderate replacement

is pervasive throughout basement, with alteration concentrated around mesostasis forming a patchy texture observed in thin section. In intervals where high alteration is observed, the majority of groundmass is partially to completely replaced, partially obscuring the original igneous textures and mineralogy. Saponite and smectite are the most common phases replacing olivine, and they are the most common secondary minerals filling vesicles and forming veins. Smectite is the most common secondary mineral within breccia.

Pyrite is present throughout Hole U1414A as an accessory phase, although it is most abundant in Sections 344-U1414A-45R-1 through 53R-1 (374.4–413.3 mbsf). It is identified by gold coloration in macroscopic observation and bright yellow in thin sections observed with reflected light. Pyrite occupies veins and alteration halos, but it is also present as a minor phase within some vesicles and background alteration. Crystal structure ranges from blocky to amorphous, and weak cleavage is occasionally observed.

Other mineral phases present throughout Hole U1414A include calcite, zeolite, quartz, and rare chlorite (observed in Sections 344-U1414A-48R-4 and 49R-1). Carbonate, quartz, and zeolite are very rare within the groundmass. Rare chlorite was observed partially replacing mesostasis, olivine, and clinopyroxene.

Alteration features are described in order of alteration intensity. Breccia represents the most intense alteration feature. Veins, followed by vesicles, represent the most ubiquitous alteration features. Halos are the least pervasive form of alteration, flanking relatively few veins and vesicles.

Basalt clastic breccia

In situ basalt-clastic breccia, recovered in interval 344-U1414A-58R-2, 51–97 cm (439.54–440.0 mbsf) (Fig. **F20**), represents 0.7% of the recovered core. Our estimate of the percentage of breccia at Site U1414 likely represents an underestimate of the true breccia proportion because core recovery is likely to favor rheologically stronger lithologies. Breccia consists of highly altered subangular basaltic clasts within a matrix of smectite. Clasts range in size from 1 to 20 mm; on average they are 10 mm. Clast groundmass is microcrystalline to cryptocrystalline and sparsely clinopyroxene plagioclase phyric. Primary textures observed include intersertal, seriate, and spherulitic. Primary igneous mineral phases (in order of decreasing abundance) include plagioclase, clinopyroxene, and Fe-Ti oxides. Phenocrysts make up ~0.5% of the clasts. Alteration with the clasts is high (~55%) and consists of saponite and accessory pyrite throughout the groundmass. Narrow silicate and saponite veins protrude into the clasts and in turn are flanked by a green-brown smectite halo. The intensity of brecciation decreases rapidly in the bottom 10 cm of the brecciated interval to a vein net. This, combined with the compositionally identical subangular clasts, suggests the breccia formed in situ. In addition, the composition and primary igneous texture is similar to the remainder of Unit 4.

Veins

A total of 1159 veins were recorded in the Site U1414 basement. Average vein density is 19.99 veins/m of recovered core, and vein fill makes up 3.5% by volume of the recovered core (Table **T4**). Figure **F21** shows the downhole distribution and abundance of veins. Vein thickness ranges from <0.1 mm to spectacular 70 mm thick veins (Fig. **F19**). Only veins thicker than 0.05 mm that were visible by macroscopic observation on a wet cut surface were recorded. Vein morphology is highly variable with morphologies that range from planar, curved, branching, anastomosing, irregular, en eschelon, and crosscutting. Secondary minerals filling veins include saponite, smectite, carbonate, pyrite, quartz, and zeolite. Additional postcruise study will be required to resolve the mineralogy of the expanding clay minerals (smectite) and zeolite. Veins may be monominerallic or polyminerallic and may contain a combination of any of the above mentioned filling phases. A few veins (5.8%) are flanked by halos.

Saponite and smectite are the most common vein-filling phases, making up 1.7% and 0.9% of the core, respectively; together they make up 73.6% of all veins. Saponite- and smectite-bearing veins range from 0.05 to 70 mm thick and on average are 0.2 mm thick. Saponite and smectite are commonly associated with pyrite, carbonate, and quartz but are observed with all other secondary mineral phases. Saponite veins were identified between 374.6 and 413.3 mbsf. Smectite is observed from 376.4 mbsf downhole but occurs in greater abundance from 403.6 mbsf downhole. Both saponite and smectite are crosscut by all other mineral phases, and they are typically located on the inner flanks of multimineral veins. In larger veins, multiple phases of saponite and smectite precipitation occur and occasionally crosscut each other. Slickenlines within saponite and smectite in some of the larger veins (Fig. **F17**) suggest precipitation during vein opening together with displacement.

Quartz is the next most abundant vein mineral, making up 0.5% of the recovered core and 13.2% of all veins. Veins containing quartz range from 0.5 to 70 mm thick, but veins containing solely quartz are

restricted to a narrow ≤0.1 mm thickness. Quartz typically occurs with and crosscuts saponite, smectite, carbonate, and pyrite. Quartz typically occurs in the central portion of a given multiminerallic vein.

Following quartz, carbonate makes up 0.4% of the total recovered core volume and 11.2% of all veins. Carbonate occurs in veins of all thicknesses, and it is typically located within the central portion and/or within one of the inner flanks of a multiminerallic vein (Fig. F18). In addition, carbonate may occur as monominerallic veins, crosscutting saponite and smectite veins. Crystals are typically elongate and are either angled or perpendicular to the vein wall, indicating crystal growth during fracture expansion.

Pyrite in veins occurs throughout the recovered basement, and it makes up 0.1% of the core (3.6% of all veins). Pyrite is typically observed within multiminerallic veins in conjunction with saponite and smectite but may also occur with carbonate and quartz. Few veins (<0.1%) are 100% pyrite; however, pyrite typically overprints and/or crosscuts saponite. Crystals within veins occur either as discrete irregular to blocky growths or as larger agglomerations filling voids. Pyrite-bearing veins between 375.2 and 376.4 mbsf are often flanked by pale yellow–bearing to dark yellow–bearing halos of varying thickness (see "Halos").

Zeolite occurs in Sections 344-U1414A-51R-1 and 51R-2 only as a minor phase within narrow (0.1–0.2 mm thick) smectite ± quartz veins. Zeolite was not identified in thin section, and there are no XRD analyses available to confirm its presence; thus, its identification relies on macroscopic observation of texture only.

Large veins (Fig. F19) often exhibit pressure-induced brecciated margins, where basement is completely replaced by saponite/smectite and "clasts" are surrounded by numerous carbonate and silica microveins.

Vesicles

All units at Site U1414 contain vesicles, the abundance of which varies from <0.1% to 40%. Typical abundances range from 0.1% to 10%. The abundance of vesicles varies considerably on a unit scale; however, increased vesicle abundances tend to coincide with the tops of unit boundaries (Fig. F16). Vesicle fill ranges from 0% to 100%, with most vesicles ≥90% filled with secondary minerals (saponite, smectite, sulfides, quartz, carbonate, and zeolite) (Table T4). The vast majority of vesicles are 100% filled with saponite/smectite, with either sulfides (pyrite), quartz, or carbonate filling the central portion of the vesicle as a late-stage infill. Common vesicle-filling assemblages, outlined by order of filling, are listed below:

- Saponite and/or smectite or pyrite;
- Saponite and/or smectite, pyrite, or quartz;
- Smectite, pyrite, or quartz;
- Pyrite or quartz; and
- Two phases of smectite and/or saponite.

Variation in vesicle fill, however, is typically restricted to discrete intervals, reflecting perhaps a restrictive fluid regime within Site U1414 basement.

Halos

Halos are present in varying abundance from 0% to 20% (by volume of core) throughout Hole U1414A basement and make up 1.38% (by volume). The abundance of each type of halo versus background is shown in Figure F22. Dark yellow halos are the most abundant, making up 0.6% of Hole U1414A basement. Dark yellow halos are typically associated with pale yellow halos (0.2% of the core by volume) forming a complex halo flanking pyrite-bearing veins. Both dark yellow and pale yellow halos contain pyrite and saponite, but pale yellow halos exhibit higher abundances of pyrite that are typically concentrated as a pyrite-rich halo front (Fig. F19). Pale yellow and dark yellow halos are absent below 374.6 mbsf. Dark gray halos make up 0.5% of the core and occur in small proportions in most Hole U1414A cores, with the exception of Cores 344-U1414A-46R, 52R, 57R, 59R, 61R, and 63R. Dark gray halos flank saponite- and smectite-bearing veins and comprise saponite and smectite alteration of groundmass. Halo widths range from 0.1 to 25 mm. Boundaries are diffuse and irregular. Pale gray halos are present in Core 344-U1414A-54R only, flanking smectite veins as part of a complex 10 mm thick dark gray–light gray halo. No thin section is currently available, so mineralogy is difficult to determine.

Alteration summary

Low-temperature hydrothermal alteration at Site U1414 is typical of a regime in which access to seawater is restricted, giving rise to oxygen-starved alteration (Laverne et al., 1996; Teagle et al., 1996, 2006). Figure F23 provides a tentative summary for the alteration history, outlining the ingress of modified, restricted fluids into Site U1414 basement. No oxidative alteration features or mineralogy were observed either in macroscopic observation or in thin section (Table T4). The extent of alteration is low, and the vast majority of basaltic groundmass is only slightly altered. Secondary minerals in veins, breccia, and vesicles make up 3.8% by volume of the recovered core. Alteration intensity tends to be focused on or near igneous unit boundaries, implying that ingress of seawater and/or modified fluid, secondary

mineral precipitation, and wall-rock interaction is restricted to interflow regions. Localized complex alteration and veins that exhibit multiple episodes of reopening and infill suggest that fluid flow occurred over several episodes, possibly throughout the ~15 m.y. history of Site U1414 basement.

The abundance of pyrite and carbonate within the uppermost portion of basement and the presence of carbonate-bearing veins and silicates in the sediment immediately overlying the basement imply lateral fluid flow at this boundary.

The presence of small amounts of chlorite in Sections 344-U1414A-48R-4 and 49R-1 suggests possible localized upflow or lateral flow of warm modified hydrothermal fluids at subgreenshist facies temperatures. No other hydrothermal mineral phase was observed (e.g., anhydrite, actinolite, prehnite, or epidote). In addition, the chlorite observed at Site U1414 may actually represent a chlorite/smectite mix, which can form at temperatures below 100°C. Chlorite or chlorite/smectite observed in the basement may have formed either early during axial hydrothermal circulation or recently. The relative timing of these fluids is hard to discern because no overprinting or crosscutting relationship with chlorite was observed.

Correlation to Site U1381

The lithology at Site U1414 generally shows a very nice continuous transition from a mid-Miocene mid-ocean ridge crest origin—and subsequent pelagic sedimentation in an abyssal environment—to a step-by-step increasing terrigenous component as the oceanic plate approaches the Central American subduction zone in the Pleistocene. Subunit IA in the sediment cover recovered from Hole U1414A consists of a sequence of hemipelagic silty clay and clay that contains some tephra horizons. This sequence correlates well with the lithology of Unit I from Holes U1381A (Expedition 334 Scientists, 2012) and U1381C (Harris et al., 2013a). The subsequent sedimentary succession (Subunit IB) consists of calcareous silty clay with more felsic ash layers. Together with the major parts of Unit II (nannofossil and sponge spicule–rich ooze), those recovered lithologies represent the missing sediment portion at Site U1381. Both the lithology and biostratigraphy support this hypothesis, which will be investigated in more detail with shore-based studies (see **"Paleontology and biostratigraphy"**).

At Site U1414, recovered basement consists of a series of sheet and massive flows. This finding is in contrast to basement at Site U1381, which consists of 69.6 m of pillow lavas. A lack of features typically associated with pillow lavas (e.g., curved chilled margins, cryptocrystalline to glassy textures, and cooling fractures) and the recovery of massive uninterrupted basaltic sections attests to the dominance of lava flows at Site U1414. Intercalated sediment observed in basement at Site U1414 and Site U1381 may indicate that the timing of lava flow/pillow lava emplacement may be related; however, further investigation is required to define the nature of lava emplacement and its relationship between lavas erupted on the Cocos Ridge (Site U1381) and the ridge–seamount transition (Site U1414). Alteration at Sites U1381 and U1414 is broadly similar, with saponite, sulfides, and quartz forming the major secondary mineral assemblages. In addition, both sites exhibit a lack of oxidative secondary mineral phases (e.g., iron-oxyhydroxide and celadonite), which suggests that basement at Sites U1414 and U1381 shared a similar, restricted fluid regime.

Paleontology and biostratigraphy

The microfossil content of core catcher samples from Hole U1414A was examined and described. Biostratigraphy was based on calcareous nannofossils and radiolarians. Benthic foraminifers were used to characterize paleoenvironmental changes at Site U1414 and provide additional biostratigraphic constraints.

Calcareous nannofossils

Calcareous nannofossils are present in all 39 core catcher samples, with good to moderate preservation throughout. However, an overall increase in recrystallization was observed downhole, becoming more pervasive below Sample 344-U1414A-34X-CC. This site provides a continuous record of sedimentation from the Miocene to the present day.

Samples 344-U1414A-1H-CC through 8H-CC are assigned to Zone NN21, based on the presence of *Emiliania huxleyi* in Sample 344-U1414A-8H-CC. The first downhole occurrence of *Pseudoemiliania lacunosa*, which constrains the transition to Zone NN19, was identified in Sample 344-U1414A-11H-CC. The last downhole occurrence of *Gephyrocapsa* spp. in Sample 344-U1414A-13H-CC, coupled with the first downhole appearance of *Discoaster* spp. in Sample 14H-CC, indicates that the boundary between Zones NN19 and NN18 (1.93 Ma) is located in Core 344-U1414A-14H. The first appearance of the genus *Sphenolithus* was observed in Sample 344-U1414A-15H-CC, which corresponds to Zone NN15 (3.70–3.92 Ma).

Pleistocene assemblages are dominated by *Gephyrocapsa* spp., whereas *Discoaster* spp. and *Sphenolithus* spp. characterize the Pliocene. Miocene assemblages are dominated by *Reticulofenestra pseudoumbilicus*,

Discoaster spp., and *Sphenolithus* spp. Sample 344-U1414A-37R-CC is moderately preserved because of recrystallization, but the presence of *Cyclicargolithus floridanus*, *Calcidiscus tropicanus*, and *R. pseudoumbilicus* constrains the base of the hole to the middle Miocene (Table T5).

Sediment accumulation rates were calculated over two intervals in Hole U1414A. The estimated accumulation rate for the upper interval (0–97.15 mbsf) is 221 m/m.y. The transition from Subunit IB (calcareous nannofossil–rich clay) to Subunit IIA (nannofossil-rich calcareous ooze) coincides with a drastic decrease in the sediment accumulation rate, with an average of 17 m/m.y. from 97.15 mbsf to the bottom of the hole.

Radiolarians

Radiolarians are present in all core catcher samples processed, with the exception of Samples 344-U1414-18H-CC and 21H-CC. The siliceous fraction was dominated by radiolarians and diatoms, with some sponge spicules also present. Radiolarian preservation and abundance was very good to good and abundant to common, respectively.

Radiolarians were exceptionally abundant and diverse (as many as 50 different species) in the upper section of Hole U1414A (Samples 344-U1414A-1H-CC through 6H-CC). This section was estimated to be no older than Zone RN16 because of the presence of *Collosphaera tuberosa*. Samples 344-U1414-8H-CC through 13H-CC are assigned to be no older than Zones RN13–RN14 because of the presence of *Pterocorys minythorax*, a taxa which first appears in Zone RN13 (Kamikuri, 2009). Abundance decreases, and deterioration in preservation is observed in Samples 344-U1414-14H-CC through 21H-CC, rendering age assignment difficult. Despite the low abundance and poor preservation throughout this interval, the radiolarian assemblage in Sample 344-U1414A-16H-CC is tentatively assigned to Zone RN9.

An apparent increase in the biosiliceous fraction is observed in Samples 344-U1414-24H-CC through 29H-CC, where radiolarians are very abundant and well preserved. The planktonic to benthic foraminiferal ratio decreases substantially in this interval (see next section). This interval contains both *Diartus hughesi* and *Diartus petterssoni* and is assigned to Zones RN6–RN7 (Table T6).

Benthic foraminifers

Benthic foraminifers were studied in 34 core catcher samples from Hole U1414A. Benthic foraminifer abundance ranges from common to few and preservation varies from good to moderate in Samples 344-U1414A-1H-CC through 27X-CC, below which the preservation varies between moderate and poor. Some specimens from Samples 344-U1414A-27X-CC through 34X-CC show signs of recrystallization, and consequently, identification to species level is very difficult.

Planktonic/benthic (P/B) ratios exhibit high values (average = 77.1%) in Samples 344-U1414A-1H-CC through 21H-CC. P/B ratios show an overall decrease to <5%–25% from Sample 344-U1414A-23H-CC to Sample 26X-CC. The ratio then recovers to values of ~90% in Samples 344-U1414A-30X-CC through 34X-CC (Table T7). Low P/B ratios cannot be explained by carbonate dissolution because of the dominance of nannofossils and the presence of benthic foraminifers in these samples. The decrease in the P/B ratios coincides with an increase in the abundance of radiolarians, which suggests that low planktonic foraminifer abundance could be caused by a changing environment.

Benthic foraminifers in Hole U1414A are tentatively divided into two assemblages with a transitional zone. The upper assemblage (Samples 344-U1414A-1H-CC through 15H-CC) is characterized by the presence of *Uvigerina auberiana*, *Cassidulina carinata*, and various species of the *Globobulimina* group (including *Globobulimina affinis*, *Globobulimina auriculata*, *Globobulimina* spp., *Praeglobobulimina ovata*, *Praeglobobulimina spinescens*, and *Chilostomella oolina*) (Fig. F24). The lower assemblage (Samples 344-U1414A-21H-CC through 34X-CC) is characterized by high abundances of *Oridorsalis umbonatus*, *Globocassidulina subglobosa*, and various species of the *Cibicides* group (*Cibicides* spp., *Cibicidoides bradyi*, *Cibicidoides pachyderma*, *Cibicidoides mckannai*, *Cibicidoides* spp., and *Fontbotia wuellerstorfi*) and the *Pullenia* group (including *Pullenia bulloides*, *Pullenia quinqueloba*, *Pullenia subcarinata*, and *Pullenia* sp.). The transitional zone is characterized by an increased abundance in *Melonis affinis*, *Uvigerina* cf. *senticosa*, and the *Pullenia* group. The presence of *Planulina renzi* (a species that disappears in the middle Miocene) in the lower sections of Hole U1414A (Fig. F24) correlates well with biostratigraphic estimates for this sedimentary interval.

Structural geology

Cores recovered from Site U1414 consist of a sedimentary sequence (~375 m) and basalt flows (~96 m) from the Cocos Ridge. Between 437 and 439.37 mbsf, a horizon of sediment is intercalated within the basalt. Bedding was determined throughout the sedimentary sequence. The dipping attitude varies from subhorizontal to gentle with a maximum value of 29° (Fig. F25). A single value of 45° was observed close to the contact with Cocos Ridge basalt. Sediment near

this contact shows well-developed foliation and indications of low-grade metamorphic overprint.

Structures within the sedimentary sequence

Dipping is generally subhorizontal throughout the hole, except between 65 and 70 mbsf and between 287 and 289 mbsf, where dipping angles vary between 24° and 29° (Fig. F25). In Unit III, at ~360 mbsf, a single observation of bedding dip angle shows an inclination of 45°. After paleomagnetic correction, strikes of the bedding planes in lithostratigraphic Units I and II trend NNW–northeast (Fig. F26), subparallel to the extension of the Cocos Ridge.

Faults at various dip angles are present throughout the sedimentary sequence (Fig. F25). Some of these faults were identified as high-angle normal faults. Because most of the faults are healed, a determination of sense of shear was not possible. Although the orientations of these faults after the paleomagnetic correction are scattered, an apparent northwest orientation was identified. Given the lack of borehole breakouts at this site (see "Downhole logging"), σ_2 and σ_3 are expected to be close to equal. This supposition is in agreement with the observed distribution of fault plane data. However, given the small number of both corrected structural data and paleomagnetic data from the interval (see "Paleomagnetism"), shore-based analyses will be necessary.

The lower part of Unit III is characterized by well-developed foliation with dip angles ranging from subhorizontal to subvertical (Fig. F25). The foliation is characterized by millimeter-scale spacing. In distinct domains, coarse clasts derived from bioturbation structures are embedded within the fine-grained foliated matrix (Fig. F27). Around these clasts, flow structures, similar to pressure shadows, can be observed. The foliation is crosscut by calcite-filled veins with various orientations. The wall rocks along the veins are often fractured into fragments or even brecciated (Fig. F28). Additionally, high-angle normal faults are associated with the veins.

The sedimentary interval interbedded within the basalt between 437 and 439.37 mbsf is characterized by horizontal to subhorizontal sedimentary structures (lamination and foliation) and a small population of mineral veins. The sediment is mainly composed of asymmetrical sandstone elements embedded in finer grained matrix.

Structures within the basement sequence

Structures in the Cocos Ridge basalt mainly comprise mineralized veins at various orientations. A preferred orientation of strike directions was not observed. Some veins show straight boundaries; others are characterized by irregular geometries. Vein mineralization mainly consists of carbonate, quartz, and pyrite. Quartz is often characterized by the fiber growth of crystals perpendicular to vein boundaries that indicate the direction of extension.

Geochemistry

Inorganic geochemistry

We collected 39 APC whole-round samples (8–20 cm long), 17 XCB whole-round samples (14–30 cm), and 5 RCB whole-round samples (14–36 cm) at a frequency of 1–2 samples per core.

All samples were thoroughly cleaned for drill water contamination. The cleaned samples from all three holes were placed in Ti squeezers and squeezed at gauge forces of <30,000 lb. The inner diameter of the Ti squeezers is 9 cm; thus, the maximum squeezing pressure was 3043 psi (~21 MPa). The pore fluid was collected in syringes and passed through a 0.2 µm filter prior to analysis. The volume of pore fluid recovered varied with lithology and coring technique. Except for one ash layer in Section 344-U1414A-8H-4 from which we collected only 10 mL, the volume of fluid recovered ranges from 36 to 58 mL from the APC samples, 4 to 48 mL from the XCB samples, and 8 to 60 mL from the RCB samples. Because no sulfate–methane transition zone (SMTZ) was encountered at this site, the chemical compositions of the samples could not be corrected for drill fluid contamination. Specific aliquots of the pore fluids were used for shipboard analyses, and the remaining fluid from each sample was sampled for shore-based analyses (see "Geochemistry" in the "Methods" chapter [Harris et al., 2013b]).

Sediment samples from Core 344-U414A-40R to the bottom of the hole were too compacted or cemented to be processed for shipboard pore fluid geochemistry. Therefore, three whole-round sediment samples with lengths ranging from 20 to 30 cm were collected between ~345 and 380 mbsf for shore-based handling and analyses. These samples were cleaned in the same manner as the shipboard interstitial water samples and stored in double vacuum-sealed bags.

Three additional samples were collected for He isotope ratio analysis from Sections 344-U1414A-14H-5, 32X-2, and 39R-1. These samples were handled in the lower tween deck to avoid contamination with gas tank He present in the Chemistry Laboratory. They were cleaned in a N_2 glove bag at 4°C, squeezed as described above, and stored in Cu tubes that were crimped tightly. A quarter of each squeezed cake was frozen for shore-based microbiological studies.

Data for the major element concentrations are listed in Table T8, and Table T9 lists the minor element concentrations. The data are illustrated in Figures F29, F30, F31, and F32.

Salinity, chloride, and alkalis (sodium and potassium)

Downhole profiles of salinity, chloride, potassium, and sodium from Site U1414 are shown in Figure F29. Salinity values decrease slightly with depth to 32.5 between ~50 and 65 mbsf, just below the sulfate minimum at 38 mbsf (Fig. F30). As no lithologic change is observed at this depth (see "Lithostratigraphy and petrology"), the observed salinity decrease most probably reflects the minimum in sulfate and the steep decrease in alkalinity values below the sulfate minimum depth. Below ~65 and ~100 mbsf, salinity is nearly constant, between 33 and 34. Salinity slightly decreases to a minimum of 30 in the lowermost ~40 m of Hole U1414A.

Except for the very slight decrease in concentration from the seawater value to 553 mM in the uppermost ~14 m, Cl concentrations increase with depth to 573 mM at ~85 mbsf, probably because of volcanic tephra hydration to clays. Values remain rather constant to ~280 mbsf. Below this depth, Cl concentrations slightly decrease downhole (Fig. F29) to 555 mM (99% seawater value), likely because of silica phase transformation reactions at depth.

Sodium concentrations are almost constant and slightly below seawater value in the uppermost ~200 m, with values that fluctuate between 460 and 470 mM. Sodium concentrations slowly increase with depth, and at the bottom of the hole they approximately reach the seawater value of 480 mM (Fig. F29).

At and below the seawater/sediment interface, K concentrations are higher than the modern seawater value of 10.4 mM by 1–2 mM. These concentrations were observed at each of the other Expedition 344 drill sites and are most likely related to clay ion exchange reactions. K values fluctuate between 12.0 and 11.0 mM to ~280 mbsf. Below this depth, K concentrations decrease to 7.2 mM (~70% seawater value) at the bottom of the hole (Fig. F29). The significant K decrease below 280 mbsf is likely controlled by clinoptilolite formation, a K-Si–rich zeolite most common in high-silica marine sediments (see "X-ray diffraction analysis").

Alkalinity, sulfate, ammonium, calcium, and magnesium

Sulfate, alkalinity, and ammonium show characteristic organic matter remineralization profiles in the uppermost ~80 m (Fig. F30).

Alkalinity increases from seawater value at the seafloor to a maximum of ~32 mM at ~33 mbsf. Below the maximum concentration, which occurs ~4 m above the sulfate minimum at 37 mbsf, alkalinity decreases steeply to ~80 mbsf, the depth of the lithostratigraphic Subunit IA/IB boundary (see "Lithostratigraphy and petrology") and then more gradually to the bottom of Hole U1414A, where it reaches a minimum of 5.3 mM (Fig. F30). The decrease in alkalinity is mainly caused by carbonate diagenesis, as suggested by the Ca concentration-depth profile. Because of the large volume of pore fluid required for alkalinity analyses, only spot analyses were performed in the deeper sediment of this site.

Similar to other sites drilled in the incoming plate offshore Costa Rica (Site U1381, drilled during this expedition, and Sites 1039 and 1253, drilled during Ocean Drilling Program Legs 170 and 205, respectively, offshore Nicoya), sulfate does not reach zero concentration. No methane production was observed, and no SMTZ was recorded at this site. At Site U1414, sulfate concentrations decrease from seawater value to a minimum of 3.6 mM at ~37 mbsf, followed by an increase to ~15 mM at ~100 mbsf, and then remain remarkably constant between 15.0 and 16.0 mM to 260 mbsf. At this depth, sulfate concentrations steeply decrease with depth to a second minimum of 2.5 mM at ~330 mbsf and increase below that depth to 12.6 mM in the deepest sediment sampled at ~337 mbsf (Fig. F30).

Ammonium concentrations increase steeply from the seafloor, where concentrations are zero, to a maximum of 3.2 mM at ~14 mbsf. Ammonium concentrations then decrease to a minimum of 2.6 mM at 37 mbsf, the depth of the sulfate minimum concentration, and then show a slight increase with depth (Fig. F30). This is unlike typical ammonium concentration-depth profiles that increase with depth and reach a maximum value below the depth of the alkalinity maximum. Below the second ammonium maximum of 4.3 mM at ~150 mbsf, concentrations decrease to ~1.8 mM at the bottom of the hole. The observed coincidence in the depths of the sulfate and ammonium concentration minima suggests that at this site there may be favorable conditions for sulfate-reducing ammonium oxidation, according to the following net reaction described by Schrum et al. (2009):

$$8NH_4^+ + 3SO_4^{2-} \rightarrow 4N_2 + 12H_2O + 5H^+.$$

The second sulfate concentration minimum at ~330 mbsf is atypical and likely reflects lateral flow of sulfate-depleted fluids that originated from oxidation of methane and/or other organic carbon sources landward of Site U1414 and migrated updip through the upper sediment of lithostratigraphic Unit III.

Based on the diffusional profile between the minimum sulfate concentration at ~300 mbsf and the plateau of sulfate concentration of ~15 mM at ~270 mbsf, the bacterial sulfate reduction reaction is currently ongoing at Site U1414. This reaction will continue as long as the bacteria have a supply of carbon, as there is an abundance of sulfate in the pore fluids (Fig. F30). Isotopic and chemical analyses of the fluid recovered from depth at this site will help constrain the nature and timing of this process.

Ca concentrations decrease from seawater value near the seafloor to a minimum of 2.6 mM at ~37 mbsf, the depth of the sulfate concentration minimum (Fig. F30). At about this depth, alkalinity has a maximum that likely triggers diagenetic carbonate precipitation, consuming Ca and some of the other alkaline earth elements, particularly Mg and Sr. There is a marked increase in Ca concentration below this depth, to a maximum of ~13.5 mM (~28% higher than modern seawater value) at ~270 mbsf, most likely caused by silicate weathering reactions. Below this depth to the bottom of Hole U1414A, the Ca concentration profile mimics that of the sulfate profile. This profile is consistent with a second carbonate diagenetic reaction zone caused by ongoing sulfate reduction at this depth interval, whereas a fraction of the low calcium observed may be attributed to the chemical composition of the sulfate-depleted laterally migrating fluid discussed above.

From the shallowest pore water analyzed to approximately the depth of the sulfate reduction zone, we observe a slight decrease in Mg concentrations from ~50 to ~46 mM (Fig. F30), which is most likely caused by the carbonate diagenetic reactions that are also evidenced by the Ca concentration profile. Mg concentrations slightly increase to ~50 mM in the interval from ~70 to 132 mbsf, the depth range of the ammonium maximum, possibly caused by ion exchange reactions in clays. Below this depth, Mg concentrations decrease to the bottom of the hole.

Conspicuous in both the major element profiles discussed above and in the minor element profiles discussed below (Figs. F30, F31) are the pronounced concentration discontinuities at ~195 mbsf, a depth that corresponds to the lithostratigraphic Subunit IIA/IIB boundary (see "Lithostratigraphy and petrology"). These strong discontinuities coincide with the change from APC to XCB cores triggered by APC refusal, as well as a missing 4 m section in the sediment recovered.

Strontium, lithium, manganese, boron, barium, and silica

Downhole distributions of Sr, Li, Mn, B, Si, and Ba are shown in Figure F31. From ~0.56 to 27.9 mbsf, Sr concentrations slightly decrease from 84.5 µM to a low value of 68.8 µM, coincident with the first zone of active sulfate reduction that extends from the seafloor to 37.4 mbsf (Fig. F30). This decrease in Sr concentrations is concomitant with a decrease in calcium and is the result of authigenic carbonate precipitation. Below 37.4 mbsf to the base of Subunit IB at 145 mbsf (see "Lithostratigraphy and petrology"), Sr concentrations gradually increase to 115 µM. Within Subunits IIA and IIB, however, Sr concentrations increase more sharply, reaching 218 µM (~2.5 times seawater value) at the base of Subunit IIB. Lithostratigraphic Subunits IIA and IIB are dominated by nannofossil-rich calcareous ooze, and the large increase in Sr concentrations within this depth range is the result of carbonate recrystallization, as has been observed in other pelagic carbonate-rich sediments (e.g., Site 1039 off the Nicoya Peninsula of Costa Rica; Shipboard Scientific Party, 1997). Across the lithostratigraphic Subunit II/III boundary, there is a sharp increase in Sr concentrations that seems to coincide with a seismic reflector (see "Lithostratigraphy and petrology"), with a maximum value of 908 µM at 328 mbsf (~10 times seawater value). The composition of this fluid is different from that above the boundary, possibly due to more intense diagenetic reactions and a higher degree of carbonate diagenesis.

Li concentrations decrease from 27 µM at 0.56 mbsf to a minimum of 16 µM at 8.9 mbsf, suggesting that Li is controlled by secondary mineral precipitation, probably related to volcanic tephra alteration, and clay ion exchange reactions in the upper sediment column. Below this depth, Li concentrations gradually increase to ~31 µM at the base of lithostratigraphic Subunit IA at ~78 mbsf (Fig. F30). Below this depth, Li concentrations increase more sharply to 170 µM at the base of lithostratigraphic Subunit IIA. The profile through this depth interval reflects diffusion from lithostratigraphic Subunit IIB, where Li concentrations are relatively constant and enriched (170–182 µM; 7 times seawater value). The reason for the elevated Li concentrations is not immediately apparent, considering this unit is dominated by alternating nannofossil-rich calcareous ooze and sponge spicule–rich calcareous ooze (see "Lithostratigraphy and petrology"). Pore fluid samples were preserved for shore-based Li isotopic analyses, which will be critical for interpreting the cause of the Li enrichment within this unit. Below Subunit IIB, Li concentrations decrease to 103 µM at 336.7 mbsf.

Mn concentrations decrease abruptly from 53.1 µM at 0.56 mbsf to 4.8 µM at 3.3 mbsf, reflecting early organic matter diagenesis. Mn concentrations are low and variable from this depth to 52.4 mbsf, ranging from 0.6 to 3.2 µM. This depth interval encompasses the first zone of active sulfate reduction at this site

(Fig. F30). Below this zone, from 60 to 170 mbsf, Mn concentrations increase and are variable, ranging from 1 to 8.5 µM. Deeper in the hole, Mn concentrations are low, not exceeding 1.6 µM, and relatively constant with depth (Fig. F31).

B concentrations increase from near seawater value at the seafloor to a maximum of 642 µM at 27.9 mbsf (~1.4 times seawater value), likely related to clay ion exchange reactions. B concentrations then decrease steadily to 299 µM at ~145 mbsf at the base of Subunit IB. B concentrations increase slightly in Subunit IIA and then remain constant and near seawater value in Subunit IIB. B concentrations are variable and range between 350 and 450 µM in Subunit III (Fig. F31).

The dissolved Si profile at Site U1414 reflects lithology and silicate mineral diagenesis. Si concentrations monotonically increase from 573 µM at 0.56 mbsf to 1032 µM at 150 mbsf, reflecting a gradual increase in the amount of biogenic opal in the sediments from the silty clay/sand dominating Subunit IA through the nannofossil-rich clay in Subunit IB. A sharp decrease in Si concentrations in Subunit IIA reflects the change from the nannofossil-rich clay of Subunit IB to the nannofossil-rich calcareous ooze in Subunit IIA. The marked increase in Si concentrations (Fig. F31) across the lithostratigraphic Subunit IIA/IIB boundary (from 631 µM at 185 mbsf to 1465 µM at 208 mbsf) indicates a change in fluid rock chemistry in Subunit IIB, dominated by the opal-A/dissolved silica equilibrium at the in situ temperature of ~35°–45°C. The distinct decrease in Si concentrations to 612 µM near the base of Subunit IIB (269–288 mbsf), which coincides with a clear decrease in dissolved K concentrations (Fig. F29), suggests that Si within this zone may be controlled by clinoptilolite formation, a K-Si–rich zeolite. Clinoptilolite was not observed in the XRD data between ~150 and 250 mbsf, but it is present within the depth interval depleted in dissolved silica and potassium (see **"X-ray diffraction analysis"**).

Pore fluid Ba concentrations are elevated with respect to bottom water concentration (~0.4 µM), ranging between 0.5 and 2.57 µM from 0.56 to 64.5 mbsf. This elevated Ba may reflect release from barite dissolution at the sulfate minimum. Below ~65 mbsf, Ba concentrations are low and constant to the Subunit II/III boundary, ranging from 0.55 to 1.0 µM. Below ~65 mbsf, the Ba concentration profile is a mirror image of the sulfate profile. It reaches a maximum value of 17.6 µM at 319.5 mbsf and then decreases to 9.4 µM at 336.7 mbsf (Fig. F31). The Ba profile is likely dominated by the stability of the mineral barite ($BaSO_4$). The Ba increase may be the result of in situ barite dissolution or the migration of Ba in the low-sulfate fluid. Postcruise solid-phase Ba analyses will be important for determining the origin of the elevated Ba in Subunit III and the time history of the fluid flow.

Organic geochemistry

Organic geochemistry data for Site U1414 are listed in Table T10, and methane concentrations are plotted in Figure F32. At this site, we detected very low concentrations of methane (2–40 ppmv), consistent with our observation that sulfate does not reach depletion. C_{2+} was not detected.

Organic and inorganic carbon distributions are illustrated in Figure F33 and listed in Table T11. Total carbon, inorganic carbon, and $CaCO_3$ abruptly increase at the base of lithostratigraphic Unit I at 145 mbsf, where concentrations change from ~2 to 5 wt%, 0.5 to 10 wt%, and 2 to 88 wt%, respectively. Total organic carbon concentrations in lithostratigraphic Unit II decrease slightly from ~2.0 to <0.8 wt%. At the boundary between lithostratigraphic Units II and III, total organic carbon values increase to 2.2 wt%. Total nitrogen decreases from 0.20 to 0.01 wt% in lithostratigraphic Units I and II and increases to 0.16 wt% in Unit III. The calculated C/N ratio is ~9 in Unit I and >10 and variable in lithostratigraphic Units II and III.

Physical properties

At Site U1414, physical properties measurements were made to characterize lithostratigraphic units. After sediment cores reached thermal equilibrium with ambient temperature at ~20°C, gamma ray attenuation (GRA) density, magnetic susceptibility, and *P*-wave velocity were measured using the Whole-Round Multisensor Logger (WRMSL). After WRMSL scanning, whole-round sections were logged for natural gamma radiation (NGR). For soft-sediment cores, thermal conductivity was measured using the full-space method prior to core splitting. Following core splitting, color reflectance and magnetic susceptibility were measured on archive-half cores using the Section Half Multisensor Logger (SHMSL). Moisture and density were measured on discrete samples collected from the working halves of split sediment cores, generally one per section. For indurated sediments, thermal conductivity was measured on split cores. *P*-wave velocity and strength were measured on the working halves of split cores.

Density and porosity

Bulk density values in Hole U1414A were determined from both GRA measurements on whole-round cores

and mass/volume measurements on discrete samples from the working halves of split cores (see **"Physical properties"** in the "Methods" chapter [Harris et al., 2013b]). Wet bulk density values determined from discrete samples range between 1.4 and 2.2 g/cm^3, and trends generally agree with the whole-round GRA density (Fig. **F34**). Grain density measurements were determined from mass/volume measurements on dry discrete samples within the sedimentary sequence. Site U1414 grain density values are relatively constant between the seafloor and 200 mbsf (Unit I–Subunit IIA), with an average value of 2.70 g/cm^3. Grain density values are more variable within Subunit IIB and Unit III, with average values of 2.63 and 2.62 g/cm^3, respectively.

Porosity data show gradual compaction within Unit I, with values decreasing to 69% at 145 mbsf. Compaction greatly increases within Subunit IIA, and porosity values reach a local minimum of 54% between 185 and 190 mbsf. Porosity then gradually increases to >75% near 225 mbsf in Subunit IIB before decreasing to the base of the hole. Porosity values are scattered within Unit III.

Magnetic susceptibility

Volumetric magnetic susceptibilities were measured using the WRMSL, and point measurements were made on the SHMSL for all core sections longer than ~20 cm (Fig. **F35**). Magnetic susceptibility values measured by these two methods are in good agreement. Background magnetic susceptibility values generally decrease with depth, reaching near- to subzero values below 350 mbsf. Excursions to high magnetic susceptibility values generally correspond to tephra layers recovered in the cores.

Natural gamma radiation

NGR counting periods for sediment cores were 10 min with measurement spacing of 20 cm (Fig. **F36**). NGR values increase to ~21 cps in the uppermost 30 m and remain approximately constant to 110 mbsf. Between 110 and 130 mbsf, NGR values rise to a peak at 130 mbsf and then decrease to below 10 cps at the Unit II/III boundary. NGR values are scattered in Unit III, with peak values near 340 and 360 mbsf.

P-wave velocity

P-wave velocities from the WRMSL show similar trends but higher values than measurements taken on the working halves of sediment split cores using the *P*-wave caliper (Fig. **F37**). *P*-wave velocities from split cores decrease in the uppermost 25 m and then gradually increase with depth. Overall, measured *P*-wave velocities in Unit I and Subunit IIA are low, averaging 1520 m/s. A local maximum at ~170 to 190 mbsf corresponds to a bulk density maximum and porosity minimum (Fig. **F34**). Few reliable *P*-wave velocities could be obtained from the split core in Unit IIB. Between 300 and 340 mbsf, *P*-wave velocities average 1850 m/s and then sharply increase below 340 mbsf to values as high as 3260 m/s.

Thermal conductivity

Thermal conductivity measurements were conducted on soft-sediment whole-round cores using the needle-probe method and on lithified split cores using the half-space method (Fig. **F38A**). Thermal conductivity trends generally correlate to those observed in bulk density and mirror those observed in porosity (Fig. **F34**). Thermal conductivity increases from 0.85 to 1.0 W/(m·K) within Unit I. In Subunit IIA, thermal conductivity increases rapidly with depth. Between ~200 (the transition from Subunit IIA to IIB) and 240 mbsf, thermal conductivity decreases with depth. Below ~240 mbsf, thermal conductivity steadily increases to reach values >2.5 W/(m·K) at the base of the sediment column.

Downhole temperature and heat flow

Four successful downhole temperature measurements between 16 and 73 mbsf were taken using the APCT-3. The four measurements yield a least-squares best-fit gradient of 168°C/km (Fig. **F38B**). Thermal conductivity throughout the depth interval of the temperature measurements is nearly constant, and the mean thermal conductivity of 0.89 W/(m·K) from 0 to 85 mbsf yields a heat flow of 149 mW/m^2.

We use the measured thermal conductivities and the estimated heat flow value of 149 mW/m^2 to extrapolate temperatures at greater depths using the Bullard (1939) method (see **"Physical properties"** in the "Methods" chapter [Harris et al., 2013b]). This method assumes steady-state conductive heat flow in the sediments. A least-squares fit yielded values of 3.22° and 53.51°C, respectively, for the sediment/water interface and the top of the basalt in Hole U1414A (Fig. **F38B**).

Sediment strength

Sediment strength was measured both by the automated vane shear and pocket penetrometer (Fig. **F39**). To compare the two measurement types, unconfined shear strength can be estimated as one half of unconfined compressive strength (Blum, 1997). Both shear and compressive strength values generally increase with depth in the uppermost 200 m to 200 and 400 kPa, respectively. A few needle penetrometer measurements between 200 and 250 mbsf

suggest that there may be a slight compressive strength decrease that corresponds to the observed high porosities within Subunit IIB.

Color spectrophotometry

Reflectance L* values are stable around 40 in Subunit IA and gradually increase to 50 with depth in Subunit IB (Fig. F40). In Subunit IIA, values increase more sharply, and then they fluctuate within Subunit IIA and Unit III with peaks exceeding 70. After some increase near the seafloor, reflectance a* and b* values are generally constant throughout Units I and II. In Unit III, a* values increase to a maximum of ~5 at ~350 mbsf and b* values decrease to the base of the sediment column.

Electrical conductivity and formation factor

Formation factor was obtained from electrical conductivity measurements in the *y*- and *z*-directions on the split core for APC cores from Hole U1414A (Fig. F41). No systematic anisotropy is observed. After a sharp rise in the upper several meters, values increase slightly with depth, mirroring the general trend of decreasing porosity.

Igneous basement

The limited time available following basalt recovery made resaturation and measurements on discrete samples infeasible. As a result, physical properties measurements were limited to those on the WRMSL and SHMSL. NGR counting periods for basalt cores were increased as much as possible (30–60 min) based on core recovery and penetration rate. Resulting data show variations that can potentially be correlated to the nature of emplacement and the degree of alteration of the igneous basement (Figs. F42, F43). The data are displayed using a modified depth scale that accounts for unreasonable core overlaps caused by tides (see core recovery in Table T1). Because of the variable size of the rock pieces, volumetric effects should be considered when interpreting the NGR, magnetic susceptibility, and GRA density data. The elevated values of NGR at ~440 mbsf correspond to recovered sediment within the igneous basement.

Paleomagnetism

Cores 344-U1414A-1H through 22H were cored with the APC and oriented with the FlexIT tool. Cores 344-U1414A-23X through 35X were cored using the XCB. Cores 344-U1414A-36R through 63R were cored with the RCB using a nonmagnetic core barrel. Pass-through magnetometer measurements were made on the entire set of archive-half cores at 5 cm intervals for the sedimentary cores and 2.5 cm intervals for the basement cores. Archive-half cores were subjected to stepwise alternating field (AF) demagnetization up to 40 mT and then measured in the pass-through superconducting rock magnetometer. We demagnetized 55 discrete samples collected from the working halves with AF demagnetization up to 120 mT, with the main objective of recognizing the characteristic remanent magnetization (ChRM).

Natural remanent magnetization of cores

Natural remanent magnetization (NRM) intensity, inclination, and declination were measured at demagnetization steps of 15, 30, and 40 mT. Magnetic properties of recovered sediments from Site U1414 show different coercivity components, which are probably related to consistent variations in the quality and quantity of magnetic minerals. The silty clay and sand of Subunit IA (0–78.3 mbsf; see **"Lithostratigraphy and petrology"**) have NRM intensities between 1.3×10^{-3} and 5.1×10^{-1} A/m, with a mean of 1.5×10^{-2} A/m. We recognize several peaks of higher NRM intensity values in the upper part of Subunit IA between 0 and ~3 mbsf. The high-intensity peaks were maintained even after 40 mT AF demagnetization (Fig. F44), which means that these high-intensity layers are likely related to changes in magnetic properties instead of being caused by drilling-induced remagnetization. NRM intensity for the calcareous nannofossil–rich clay of Subunit IB (78.30–145.34 mbsf) is similar to that of Subunit IA, with the exception of the upper part, which has a peak in NRM intensity between ~75 and ~85 mbsf. NRM intensity shows a steplike increase across the Subunit IIA/IIB boundary. NRM for Subunit IB ranges from 1.0×10^{-3} to 1.7×10^{-1} A/m, with a mean of 7.8×10^{-3} A/m. Paleomagnetic measurements show that the nannofossil-rich clay and ooze in Subunit IIA (145.34–200.01 mbsf) have NRM intensities ranging from 7.7×10^{-4} to 1.5×10^{-2} A/m, with a mean of 3.2×10^{-3} A/m. In Subunit IIB, cores recovered from 200.01 to 309.37 mbsf are alternating nannofossil-rich calcareous ooze and sponge spicule–rich calcareous ooze. NRM intensities of these sediments vary between 1.5×10^{-4} and 4.8×10^{-1} A/m, with a mean of 1.5×10^{-2} A/m, with a broad peak in NRM intensity between ~200 and ~230 mbsf. Unit III, which is composed of calcareous and siliceous cemented silt and sandstones, shows a minimum NRM intensity value of 1.2×10^{-5} A/m and a maximum value of 4.8×10^{-1} A/m, with an average of 6.1×10^{-3} A/m.

We observe a strong correlation between the variations in magnetic susceptibility and the variations in NRM intensity (see **"Physical properties"**).

Natural remanent magnetization of basement rocks

The lowermost ~96 m of recovered materials from Hole U1414A consist mainly of basaltic rock. We selected a slower tray speed mode for the pass-through measurements at every 2.5 cm and AF demagnetized core sections to 40 mT. Basement Units 1–3 show NRM intensities ranging from 3.2×10^{-1} to 18.7 A/m, with an average of 6.3 A/m. NRM intensity shows downhole variation that can be correlated to the alteration states of the rocks. The fresh part of the basalt is characterized by stronger NRM intensity. Both normal and reversed polarities were observed, but no further data analyses could be done because of a lack of time at the end of the expedition.

Magnetic noise in superconducting rock magnetometer

Several flux jumps appeared at various steps and lithologies and occurred in the intervals ~90–100, ~115–125, and ~240–290 mbsf. Major and persistent flux jumps also occurred for most of the 40 mT AF demagnetization steps. Therefore, the data are unreliable in the intervals ~25–110 and ~165–290 mbsf.

Paleomagnetic demagnetization results

The recovered sediment sections were AF demagnetized at steps of 15, 30, and 40 mT. The magnetization of the drilling overprint was usually successfully eliminated by the first AF demagnetization step (15 mT). ChRM directions, because of the flux-jump artifacts, cannot be reliably recognized from the pass-through measurements.

The remanent magnetization of 55 discrete samples from lithostratigraphic Units I–III was investigated using stepwise AF demagnetization. We were able to isolate the ChRM for most of the samples after removal of the drilling-induced overprint (Fig. **F45**). However, we were not able to demagnetize some samples, which suggests the presence of a stronger magnetic component with a higher coercivity.

Magnetostratigraphy

We were able to correct the declination of the APC cores (0–200 mbsf) to geographic coordinates using the FlexIT orientation data.

We analyzed ChRM inclinations and declinations (for APC cores) from both discrete and pass-through measurements using principal component analysis to define magnetic polarity sequences. We recognize several magnetozones defined as intervals with multiple consecutive samples with polarities that are distinctly different from neighboring intervals.

The upper part of Hole U1414A is characterized by a short interval with normal polarities and then a longer reversed interval followed by three normal intervals (Fig. **F44**). The Brunhes Chron, if present, is very short or condensed in the uppermost ~10 m. Between 94 and 114 mbsf, four samples with homogeneous characteristics confirm the presence of a normal polarity interval. However, most of the samples from the middle part of Hole U1414A show reversed polarity. The lower part of the hole (below 282 mbsf) includes six samples with normal polarity, separated by only one sample with reversed shallow inclination. Inclination values are very shallow, <20°, which is consistent with the expected paleolatitude for this site.

Downhole logging

Logging operations

Coring in Hole U1414A ended at 1205 h on 9 December 2012 (all times are local Costa Rica time, UTC – 6 h). Hole U1414A was cored and reentered without problems, and a wiper trip was deemed unnecessary. Ten barrels of heavy mud were pumped to the bottom to stop backflow, the RCB bit was dropped in the hole, and the pipe was raised to logging depth. Rig-up of the wireline system started at 1645 h. Two tool strings were run into Hole U1414A: a triple combo–UBI followed by a FMS-sonic combination. For an illustration of the tool strings deployed in Hole U1414A, explanation of the acronyms, and details on the wireline tools, see the **"Methods"** chapter (Harris et al., 2013b).

The triple combo–UBI string included (from top to bottom) the Enhanced Digital Telemetry Cartridge (EDTC), Hostile Environment Natural Gamma Ray Sonde (HNGS), Hostile Environment Litho-Density Sonde (HLDS), High-Resolution Laterolog Array, General Purpose Inclinometry Tool (GPIT), and UBI. Hole U1414A was drilled with an APC/XCB BHA (11 7/16 inch bit) from the seafloor to 312 mbsf. The hole was then reentered with a FFF and drilled to 472 mbsf with an RCB BHA (9 7/8 inch bit). Because of expected differences in hole diameter, we planned three passes with different UBI settings. Pass 1 covered the entire open hole interval with the UBI set for a 9 7/8 inch bit size, a vertical resolution of 0.4 inches, and 180 samples/revolution. Pass 2 was run in the lower part of the hole drilled by RCB with the same settings as in Pass 1 but with a higher vertical resolution of 0.2 inches. Finally, Pass 3 spanned the upper part of the hole drilled by APC/XCB with the UBI set for an 11 7/16 inch bit size, a vertical resolution of 0.4 inches, and 140 samples/revolution. The lower number of samples/revolution allows for a longer time window to pick the borehole wall reflection. The UBI frequency was set to 250 kHz in all passes.

The triple combo–UBI tool string started down the hole at 1915 h on 9 December. The seafloor was detected on the gamma ray log at ~2470 mbrf, but the measured natural radioactivity values were very low, and the seafloor could be 1–2 m shallower. In the Hole U1414A cores, there is a sharp transition from sediment to basalt at 375 mbsf (see **"Lithostratigraphy and petrology"**). A seafloor pick of 2469 mbrf is the same as the driller's seafloor depth and puts the sediment/basalt boundary at 375 mbsf in the logs. Hence, the mbsf depths in the Hole U1414A logs have been converted from seafloor depth to 2469 mbrf (this corresponds to the wireline log depth below seafloor [WSF] depth scale; see the **"Methods"** chapter [Harris et al., 2013b]).

After the triple combo–UBI exited the drill pipe at 94 mbsf, its descent stopped when an obstruction was encountered with the base of the tool string at 411 mbsf (61 m above the total depth of the hole). Repeated attempts to pass the obstruction were unsuccessful, and at 2147 h we started to log up. The first pass ended with the base of the tool string at 139 mbsf, which put the top of the triple combo–UBI just below the base of the pipe. The tool string was then lowered back to the obstruction at the bottom. A second pass with a higher vertical resolution was started from 417 mbsf and ended at 311 mbsf, where the borehole became too large to collect useful UBI data. We then moved the tool string down to 331 mbsf, set the UBI to image the larger APC/XCB borehole, and started the third pass at 0038 h on 10 December. During recovery, high tension forced us to stop with the base of the tool string just inside the drill pipe. After pumping to wash the tool string of debris, we were able to resume recovering the tools. The triple combo–UBI reached the rig floor at 0400 h and was rigged down at 0540 h.

The FMS-sonic tool string included (from top to bottom) the EDTC, HNGS, Dipole Sonic Imager, GPIT, and FMS. We planned two passes: a first pass covering the smaller diameter RCB interval at the bottom of the hole followed by a full second pass. The FMS-sonic tool string was rigged up and started down the hole at 0640 h on 10 December. As in the previous run, the obstruction at the bottom was reached with the base of the tool string at 417 mbsf, and we started the first pass at 0905 h. The first pass ended just above the top of the RCB hole at 306 mbsf, and we returned to the bottom for a full second pass. At the end of the second pass, the drill pipe was reentered without problems and the FMS-sonic tool string returned to the rig floor at 1132 h. The wireline system was fully rigged down at 1300 h, ending logging operations for Expedition 344.

Downhole log data quality

The downhole log data collected in Hole U1414A were processed to convert to depth below seafloor and to match depths between different logging runs. The resulting depth scale is wireline matched depth below seafloor (WMSF; see the **"Methods"** chapter [Harris et al., 2013b]), and from here on "mbsf" denotes the WMSF depth scale.

A key factor that influences downhole log data quality is the size and irregularity of the borehole. Measurements of the diameter of Hole U1414A are summarized in Figure **F46.** The LCAL track in this figure is measured by a single caliper arm on the HLDS tool (triple combo–UBI tool string), and the C1 and C2 tracks are the hole diameters measured in two orthogonal directions by the two pairs of arms that support the microresistivity pads on the FMS tool (FMS-sonic tool string). As noted earlier, Hole U1414A was drilled with an APC/XCB bit (11 7/16 inches) to 312 mbsf and then continued to total depth with an RCB bit (9 7/8 inches). The hole is nearly in gauge below 338 mbsf and is as much as ~4 inches larger than the bit diameter in the interval 185–338 mbsf. Above 180 mbsf, the hole is locally enlarged beyond the maximum diameter measurable by the HLDS caliper (~18 inches). In this enlarged hole interval, measurements that rely on good contact with the formation, such as HLDS density, are likely to be unreliable. The notable differences between the hole diameters measured in the two logging runs above ~200 mbsf are discussed below.

The overall quality of the logging data can also be assessed from the match between measurements acquired in different runs or passes. In general, the downhole log data acquired in Hole U1414A show excellent repeatability. Total gamma ray logs measured in different passes of the same tool string are very similar (Fig. **F46**), and spectral gamma ray data are also consistent (Fig. **F47**). The only differences are observed where the borehole diameter changed between different logging runs (e.g., around 160 mbsf), and these are discussed next.

Changes in borehole size

Above ~200 mbsf, there are several narrow borehole intervals with obvious differences between the hole diameters measured by the HLDS tool in the triple combo–UBI tool string and the FMS in the FMS-sonic tool string (Fig. **F46**). These hole size measurements were taken ~11 h apart. The differences in hole size and the observation that the hole diameter is smaller than the bit in these narrow hole intervals suggest that the formation was actively swelling and spalling off. For example, the hole restriction at ~160 mbsf

became narrower between the first and second run, and the sharp hole restriction at ~200 mbsf that was measured in the FMS-sonic run was not present in the earlier triple combo–UBI run. Another restriction observed in the triple combo–UBI run at ~145 mbsf disappeared in the subsequent FMS-sonic run, implying that pieces of the swelling formation fell into the hole. These marked changes in hole diameter affected the natural radioactivity measurements: for example, the small total gamma ray peak observed at ~160 mbsf in the triple combo–UBI runs became much more prominent in the FMS-sonic measurements, likely because of the decreased distance between the borehole wall and the detector. Similar changes attributable to changes in borehole diameter can be observed at ~145 and ~200 mbsf both in the total gamma ray (Fig. **F46**) and spectral gamma ray data (Fig. **F47**).

Log characterization and logging units

The logging measurements acquired in Hole U1414A are summarized in Figure **F48.** The total gamma ray data measured by the HNGS (track HSGR in the figure) generally correlate with NGR measurements made on cores. The total gamma ray values measured by the HNGS are expressed in an American Petroleum Institute (gAPI) scale based on a standard artificial formation built to simulate about twice the radioactivity of a typical shale and conventionally set to 200 gAPI (Ellis and Singer, 2007). The units of the NGR measurements made on whole-core sections are in counts per second (cps; for a detailed description of the NGR apparatus, see Vasiliev et al., 2010). The comparison of log and core natural gamma ray measurements in this figure shows that their curves overlap if 1 cps equals ~1 gAPI. The figure also shows tracks of measured bulk density, electrical resistivity, compressional and shear wave velocity, and FMS images. The density, resistivity, and elastic wave velocities show very similar patterns because the variation of these physical properties is similarly controlled by changes in formation porosity and lithology.

We distinguish four logging units in the interval logged in Hole U1414A. Logging Unit 1 (94–259 mbsf) is characterized by total gamma ray values that decrease from between ~40 gAPI at 120 mbsf to ~10 gAPI at the base of the unit. Bulk density, resistivity, and elastic wave velocities are generally low in this unit and show a decreasing trend toward the base of the unit, where bulk density is 1.5 g/cm^3, resistivity is 0.5 Ωm, and compressional and shear velocities are 1.6 km/s and 0.4 km/s, respectively. As noted earlier, the low and variable densities observed above 185 mbsf are likely unreliable because of the enlarged borehole. Logging Unit 2 (259–335 mbsf) displays an increase with depth of bulk density (1.6–1.8 g/cm^3), resistivity (0.5–1 Ωm), compressional velocity (1.7–2.1 km/s), and shear velocity (0.5–0.7 km/s). Natural gamma ray values are generally 10–30 gAPI. Logging Unit 3 (335–375 mbsf) contains larger variations in physical properties, with gamma ray values ranging between 20 and 60 gAPI, bulk densities between 1.8 and 2.2 g/cm^3, resistivities between 1 and 10 Ωm, compressional velocities between 2 and 4 km/s, and shear velocities between 0.5 and 2.7 km/s. Finally, Logging Unit 4 (375–410 mbsf) corresponds to the volcanic basement (see **"Lithostratigraphy and petrology"**). This basalt interval features very low natural radioactivity (10 gAPI or less) and high bulk density (2.3–2.8 g/cm^3), resistivity (2–100 Ωm), compressional velocity (3.2–6.7 km/s), and shear velocity (1.7–3.8 km/s).

Borehole images

Borehole images displaying FMS microresistivity data collected in two runs and UBI reflection amplitudes (related to the small-scale roughness of the borehole wall) are shown in Figure **F49.** These images span the lower interval logged in Hole U1414A, containing the consolidated sediments in Logging Unit 3 and the basalt of Logging Unit 4. In the sediment interval (340–375 mbsf), the FMS and UBI images show a sedimentary formation with generally horizontal layers, except for an interval between 360 and 370 mbsf where there is evidence of a westward dip. The UBI image also shows vertical fractures oriented ESE–WNW, which could be drilling-induced tensile fractures (Zoback et al., 2003). The top of a steep fracture intersecting the borehole is also visible at 354–355 mbsf. The base of the sediment column at ~375 mbsf is marked by a thin (<0.5 m) borehole enlargement, which has also been measured by the caliper logs (Fig. **F46**). In the basalt (375–410 mbsf), the image logs show a complex set of fractures.

References

Blum, P., 1997. Physical properties handbook: a guide to the shipboard measurement of physical properties of deep-sea cores. *ODP Tech. Note,* 26. **doi:10.2973/odp.tn.26.1997**

Bullard, E.C., 1939. Heat flow in South Africa. *Proc. R. Soc. London, Ser. A,* 173(955):474–502. **doi:10.1098/rspa.1939.0159**

Ellis, D.V., and Singer, J.M., 2007. *Well Logging for Earth Scientists* (2nd ed.): Dordrecht, The Netherlands (Springer).

Expedition 334 Scientists, 2012. Site U1381. *In* Vannucchi, P., Ujiie, K., Stroncik, N., Malinverno, A., and the Expedition 334 Scientists, *Proc. IODP,* 334: Tokyo (Integrated Ocean Drilling Program Management International, Inc.). **doi:10.2204/iodp.proc.334.106.2012**

Harris, R.N., Sakaguchi, A., Petronotis, K., Baxter, A.T., Berg, R., Burkett, A., Charpentier, D., Choi, J., Diz Ferreiro, P., Hamahashi, M., Hashimoto, Y., Heydolph, K., Jovane, L., Kastner, M., Kurz, W., Kutterolf, S.O., Li, Y., Malinverno, A., Martin, K.M., Millan, C., Nascimento, D.B., Saito, S., Sandoval Gutierrez, M.I., Screaton, E.J., Smith-Duque, C.E., Solomon, E.A., Straub, S.M., Tanikawa, W., Torres, M.E., Uchimura, H., Vannucchi, P., Yamamoto, Y., Yan, Q., and Zhao, X., 2013a. Input Site U1381. In Harris, R.N., Sakaguchi, A., Petronotis, K., and the Expedition 344 Scientists, *Proc. IODP,* 344: College Station, TX (Integrated Ocean Drilling Program). **doi:10.2204/iodp.proc.344.103.2013**

Harris, R.N., Sakaguchi, A., Petronotis, K., Baxter, A.T., Berg, R., Burkett, A., Charpentier, D., Choi, J., Diz Ferreiro, P., Hamahashi, M., Hashimoto, Y., Heydolph, K., Jovane, L., Kastner, M., Kurz, W., Kutterolf, S.O., Li, Y., Malinverno, A., Martin, K.M., Millan, C., Nascimento, D.B., Saito, S., Sandoval Gutierrez, M.I., Screaton, E.J., Smith-Duque, C.E., Solomon, E.A., Straub, S.M., Tanikawa, W., Torres, M.E., Uchimura, H., Vannucchi, P., Yamamoto, Y., Yan, Q., and Zhao, X., 2013b. Methods. In Harris, R.N., Sakaguchi, A., Petronotis, K., and the Expedition 344 Scientists, *Proc. IODP,* 344: College Station, TX (Integrated Ocean Drilling Program). **doi:10.2204/iodp.proc.344.102.2013**

Kamikuri, S., Motoyama, I., Nishi, H., and Iwai, M., 2009. Neogene radiolarian biostratigraphy and faunal evolution rates in the eastern equatorial Pacific ODP Sites 845 and 1241. *Acta Palaeontol. Pol.,* 54(4):713–742. **doi:10.4202/app.2008.0076**

Kirschvink, J.L., 1980. The least-squares line and plane and the analysis of palaeomagnetic data. *Geophys. J. R. Astron. Soc.,* 62(3):699–718. **doi:10.1111/j.1365-246X.1980.tb02601.x**

Laverne, C., Belarouchi, A., and Honnorez, J., 1996. Alteration mineralogy and chemistry of the upper oceanic crust from Hole 896A, Costa Rica rift. *In* Alt, J.C., Kinoshita, H., Stokking, L.B., and Michael, P.J. (Eds.), *Proc. ODP, Sci. Results,* 148: College Station, TX (Ocean Drilling Program), 151–170. **doi:10.2973/odp.proc.sr.148.127.1996**

Schrum, H.N., Spivack, A.J., Kastner, M., and D'Hondt, S., 2009. Sulfate-reducing ammonium oxidation: a thermodynamically feasible metabolic pathway in subseafloor sediment. *Geology,* 37(10):939–942. **doi:10.1130/G30238A.1**

Shipboard Scientific Party, 1997. Site 1039. *In* Kimura, G., Silver, E., Blum, P., et al., *Proc. ODP, Init. Repts.,* 170: College Station, TX (Ocean Drilling Program), 45–93. **doi:10.2973/odp.proc.ir.170.103.1997**

Teagle, D.A.H., Alt, J.C., Bach, W., Halliday, A.N., and Erzinger, J., 1996. Alteration of upper ocean crust in a ridge-flank hydrothermal upflow zone: mineral, chemical, and isotopic constraints from Hole 896A. *In* Alt, J.C., Kinoshita, H., Stokking, L.B., and Michael, P.J. (Eds.), *Proc. ODP, Sci. Results,* 148: College Station, TX (Ocean Drilling Program), 119–150. **doi:10.2973/odp.proc.sr.148.113.1996**

Teagle, D.A.H., Alt, J.C., Umino, S., Miyashita, S., Banerjee, N.R., Wilson, D.S., and the Expedition 309/312 Scientists, 2006. *Proc. IODP,* 309/312: Washington, DC (Integrated Ocean Drilling Program Management International, Inc.). **doi:10.2204/iodp.proc.309312.2006**

Vasiliev, M.A., Blum, P., Chubarian, G., Olsen, R., Bennight, C., Cobine, T., Fackler, D., Hastedt, M., Houpt, D., Mateo, Z., and Vasilieva, Y.B., 2011. A new natural gamma radiation measurement system for marine sediment and rock analysis. *J. Appl. Geophys.,* 75:455–463. **doi:10.1016/j.jappgeo.2011.08.008**

Zijderveld, J.D.A., 1967. AC demagnetization of rocks: analysis of results. *In* Collinson, D.W., Creer, K.M., and Runcorn, S.K. (Eds.), *Methods in Palaeomagnetism:* Amsterdam (Elsevier), 254–286.

Zoback, M.D., Barton, C.A., Brudy, M., Castillo, D.A., Finkbeiner, T., Grollimund, B.R., Moos, D.B., Peska, P., Ward, C.D., and Wiprut, D.J., 2003. Determination of stress orientation and magnitude in deep wells. *Int. J. Rock Mech. Min. Sci.,* 40(7–8):1049–1076. **doi:10.1016/j.ijrmms.2003.07.001**

Publication: 11 December 2013
MS 344-104

Figure F1. Seismic traveltime section of Line 2497, showing the location of Site U1414.

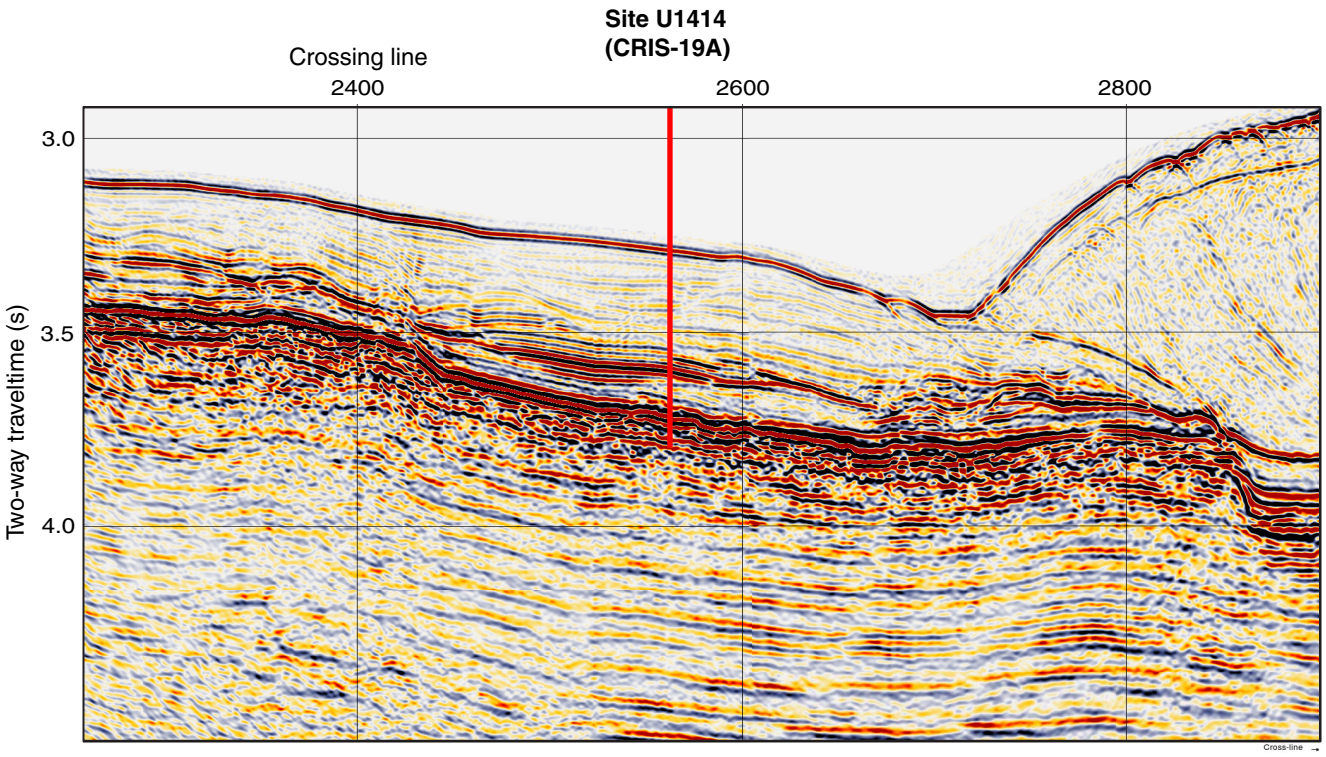

Figure F2. Location of Expedition 344 drill sites. Red diamonds denote Expedition 344 sites (U1380, U1381, and U1412–U1414), and yellow diamonds denote Expedition 334 sites not occupied during Expedition 344 (U1378 and U1379). Red lines = 3-D seismic survey, black lines = seismic reflection lines. Numbers along the short and long axes of the 3-D survey represent inlines and crosslines, respectively.

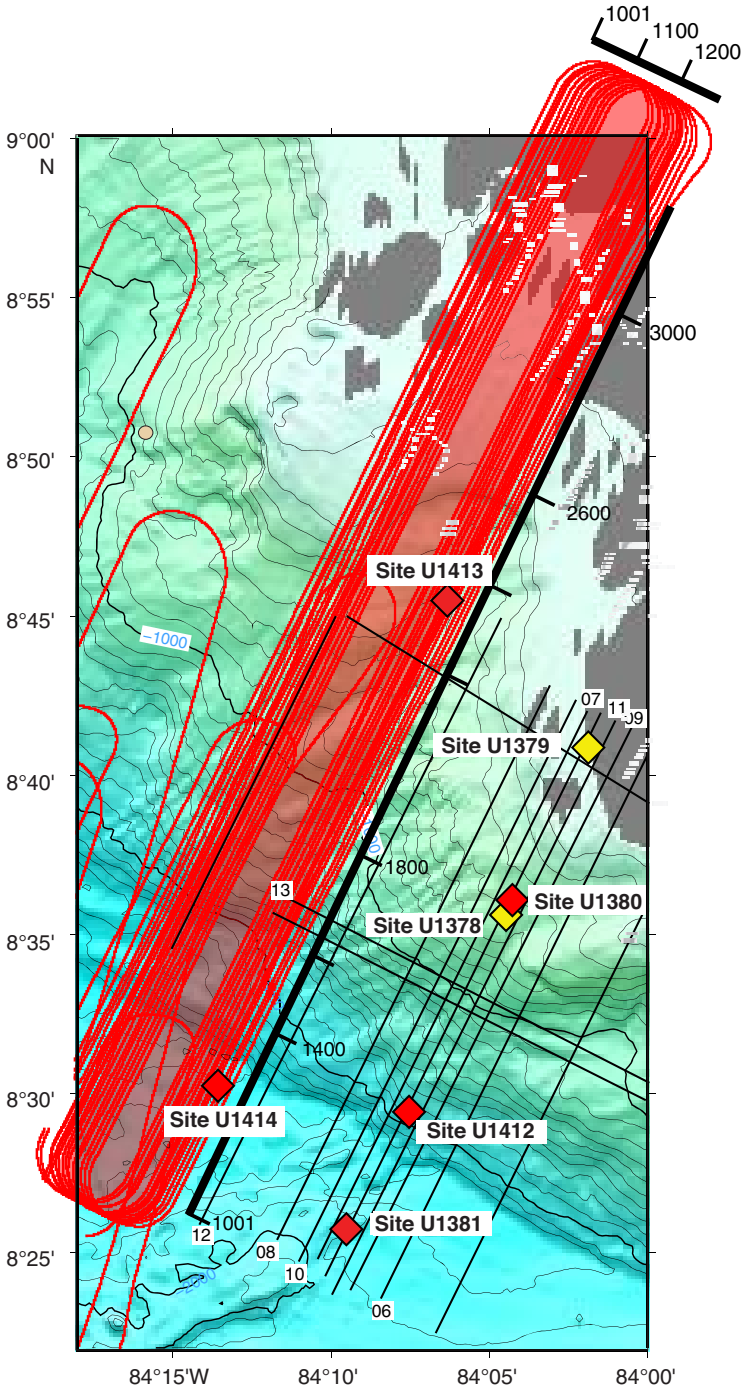

Figure F3. Lithostratigraphic summary, Hole U1414A.

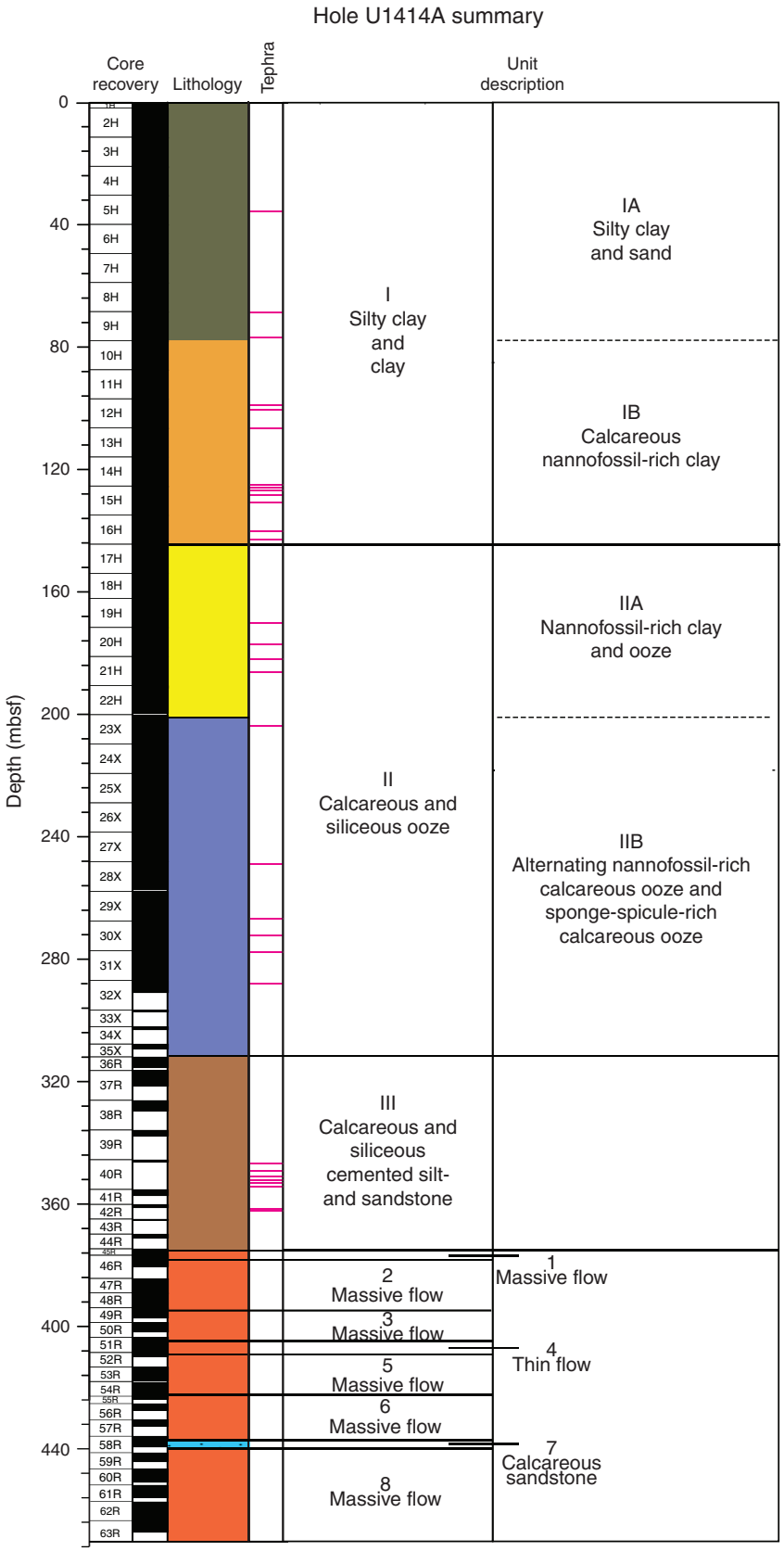

Figure F4. Basement lithostratigraphic summary, Hole U1414A.

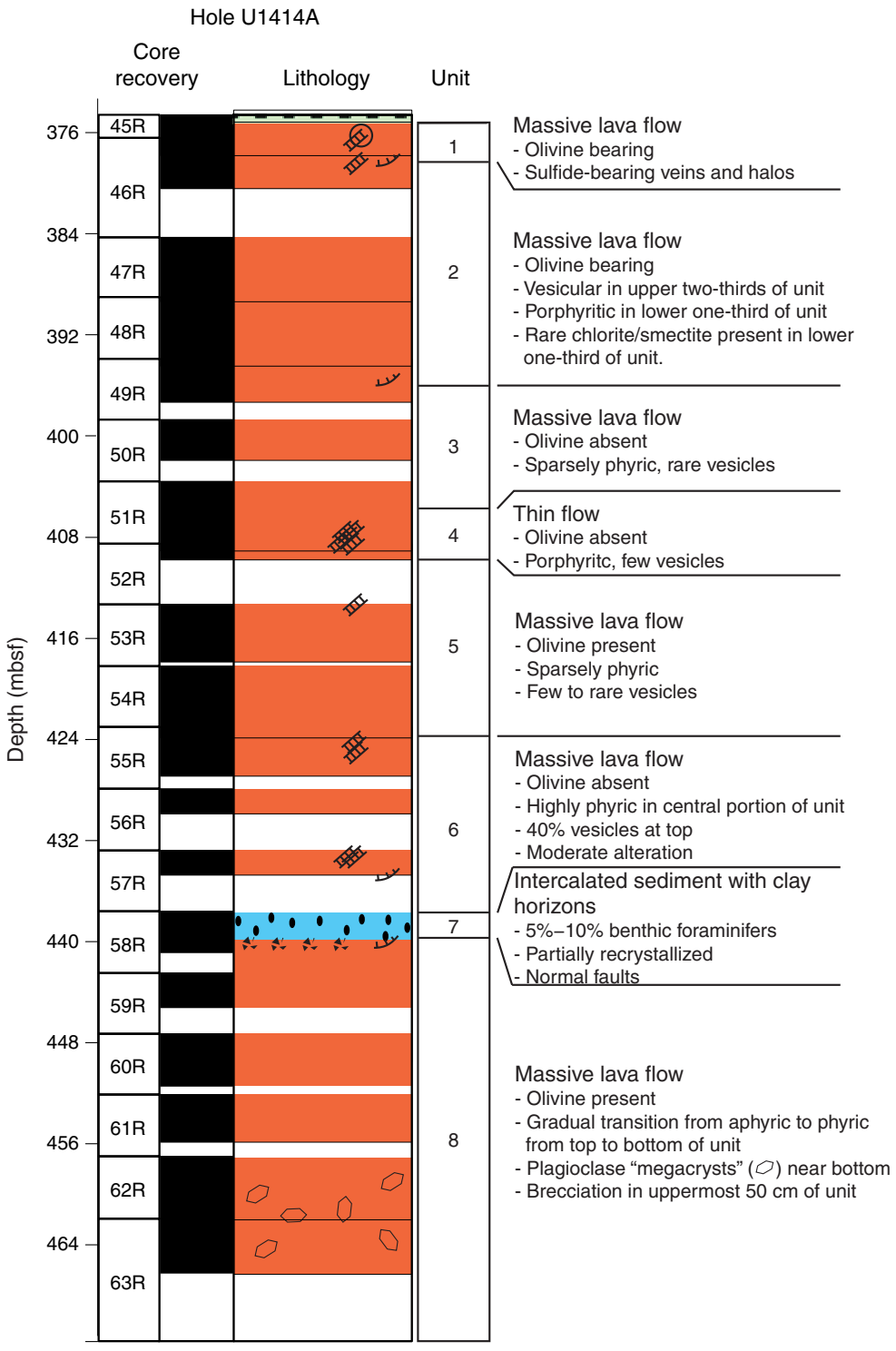

Figure F5. Representative digital image of lithostratigraphic Subunit IA, showing grayish green massive silty clay with common sand lenses and pyrite smudges (interval 344-U1414A-2H-2A, 50–65 cm).

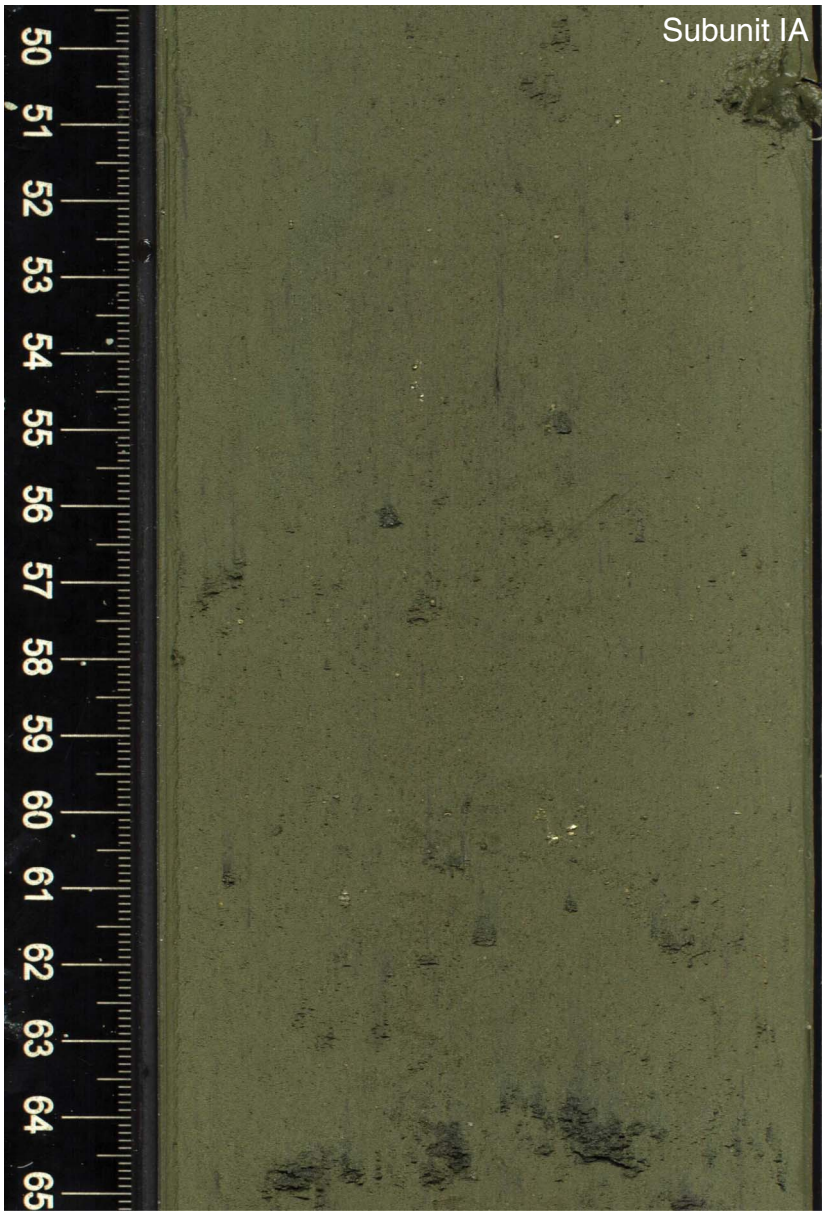

Figure F6. Representative digital image of lithostratigraphic Subunit IB, showing light greenish gray massive calcareous nannofossil-rich clay with pyrite smudges (interval 344-U1414A-10H-2A, 45–60 cm).

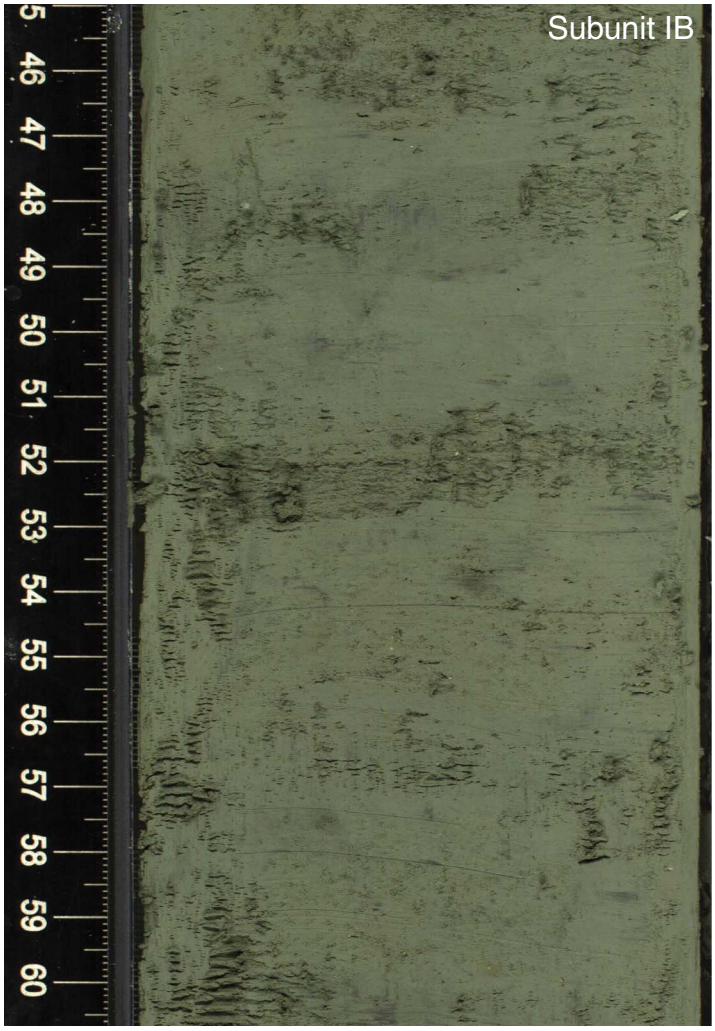

Figure F7. Digital image of a ~66 cm thick pinkish gray felsic tephra layer (interval 344-U1414A-8H-4A, 96 cm, to 8H-5A, 46 cm). Contacts are sharp but curved at the base because of drilling disturbance and irregular at the top (dashed line) representing small-scale reworking in the soupy transition to the background sediment. The tephra layer contains medium sand–sized ash that grades normally upward to fine silt–sized ash. Tephra components are mainly transparent glass shards, feldspar, amphibole, and biotite.

Figure F8. Representative digital image of lithostratigraphic Subunit IIA, showing whitish greenish massive calcareous nannofossil calcareous ooze with pyrite smudges (interval 344-U1414A-17H-2A, 30–45 cm).

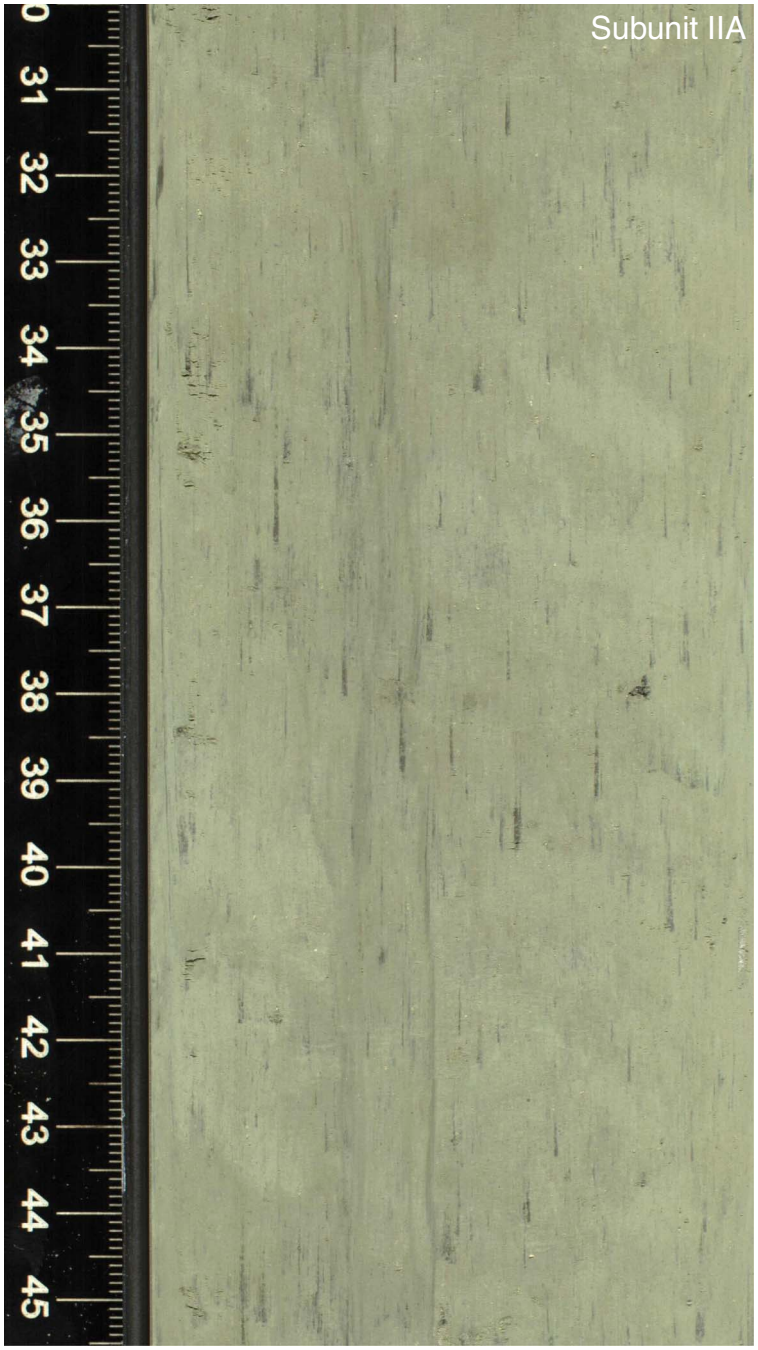

Figure F9. Representative digital image of lithostratigraphic Subunit IIB, showing white massive calcareous nannofossil ooze with abundant sponge spicules (see photomicrograph inset) and some disseminated glauconite clasts and horizons (interval 344-U1414A-28X-5A, 50–65 cm).

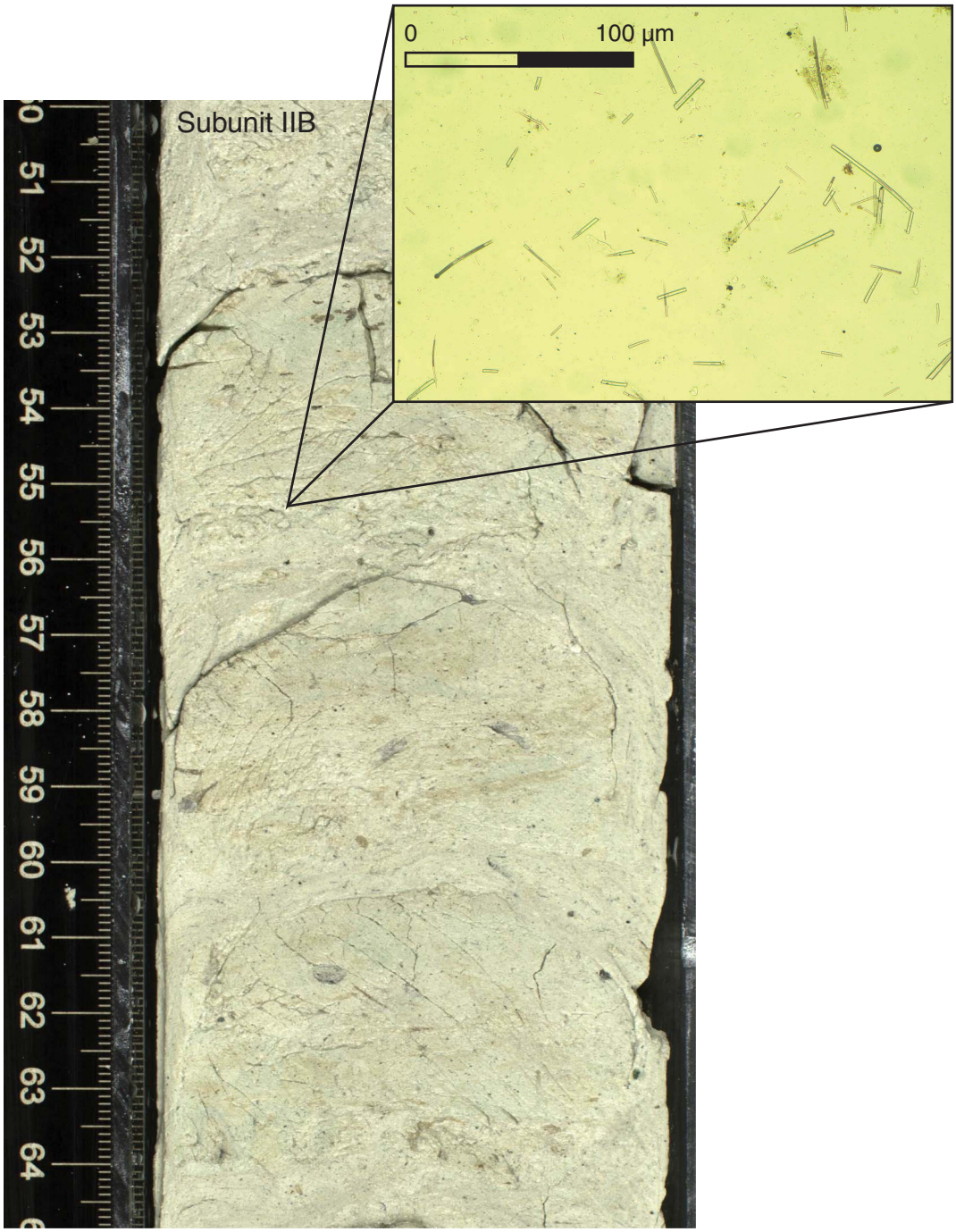

Figure F10. Representative digital image of lithostratigraphic Unit III, showing whitish grayish calcareous siltstone with heavy bioturbation and disrupted primary bedding, as well as traces of black tephra (interval 344-U1414A-37R-2A, 66–81 cm).

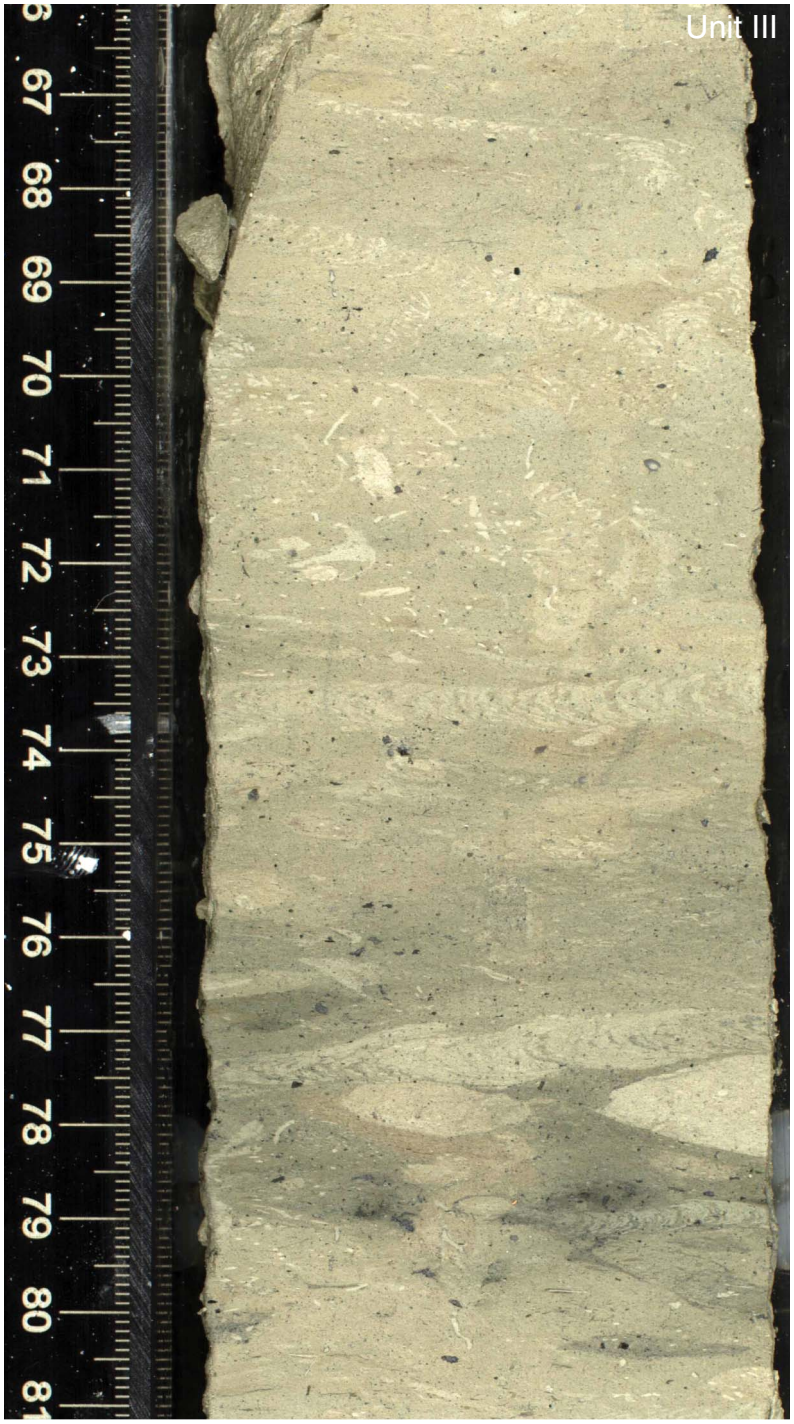

Figure F11. Representative digital image of lithostratigraphic Unit III, showing brownish to very dark gray siliceous sandstone interlayered by chert-like laminae. Sedimentary structures, probably representing former primary bedding, have been replaced by diagenetic silica (interval 344-U1414A-41R-2A, 12–27 cm).

Figure F12. Digital image of sharp inclined contact of calcareous to siliceous siltstone in Unit III to completely lithified limestone breccia consisting of centimeter-sized clasts (interval 344-U1414A-42R-CCA, 0–19 cm).

Figure F13. Digital images of tephras. **A.** Slightly consolidated, normally graded brown tephra layer with brownish glass shards at 19–28 cm (interval 344-U1414A-12H-1A, 13–33 cm). **B.** Disseminated black tephra horizon predominantly made of transparent glass shards with pyrite as alteration product (interval 344-U1414A-24X-3A, 21–37 cm).

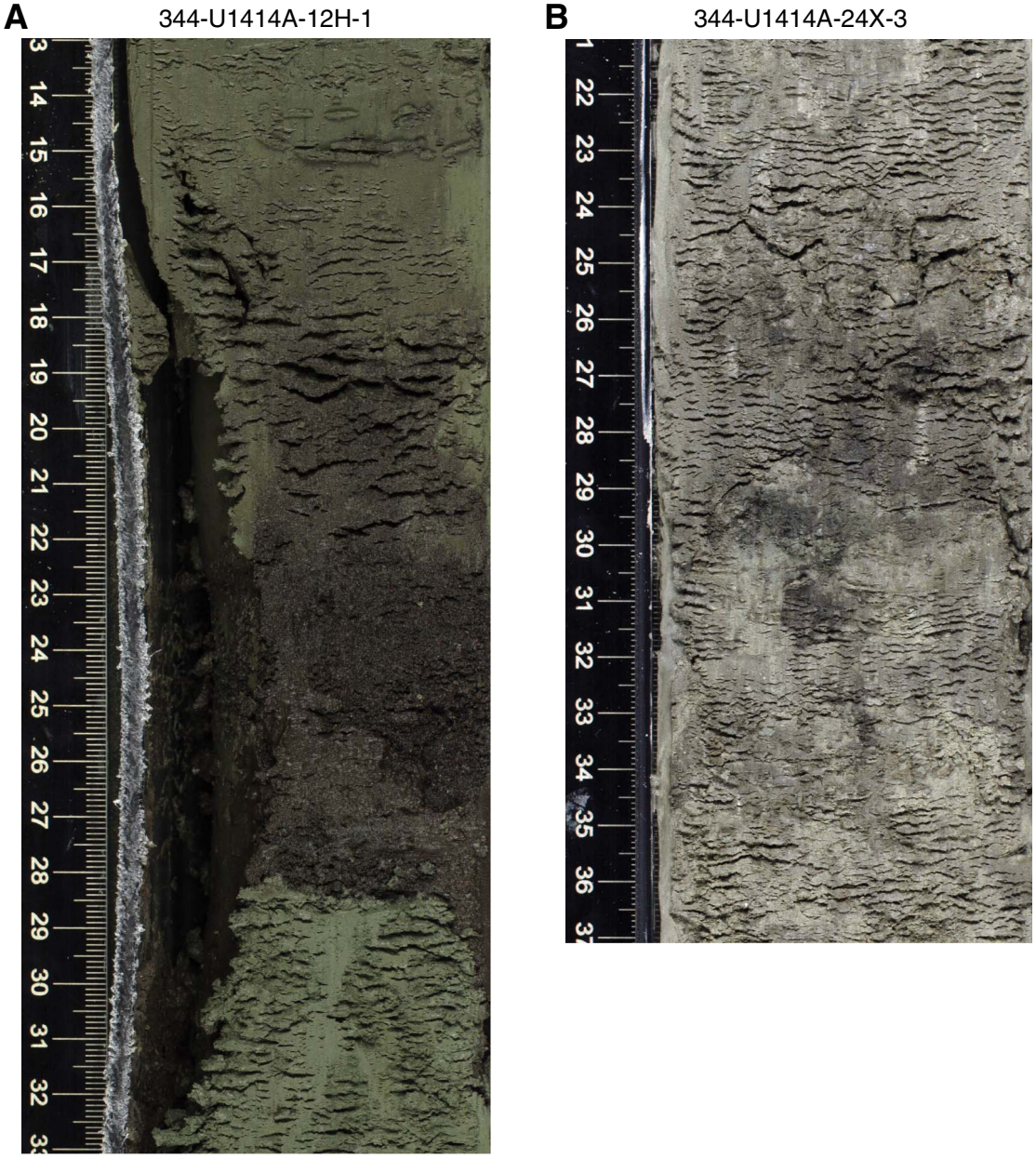

Figure F14. Typical XRD patterns obtained for bulk rock samples, Site U1414. A = amphibole (hornblende), C = calcite, Chl = chlorite (clinochlore), D = dolomite, H = halite, P = plagioclase, Py = pyrite, Q = quartz, S = smectite, Si = silica (opal), Z = zeolite (laumontite and heulandite in Unit I; clinoptilolite in Units II and III).

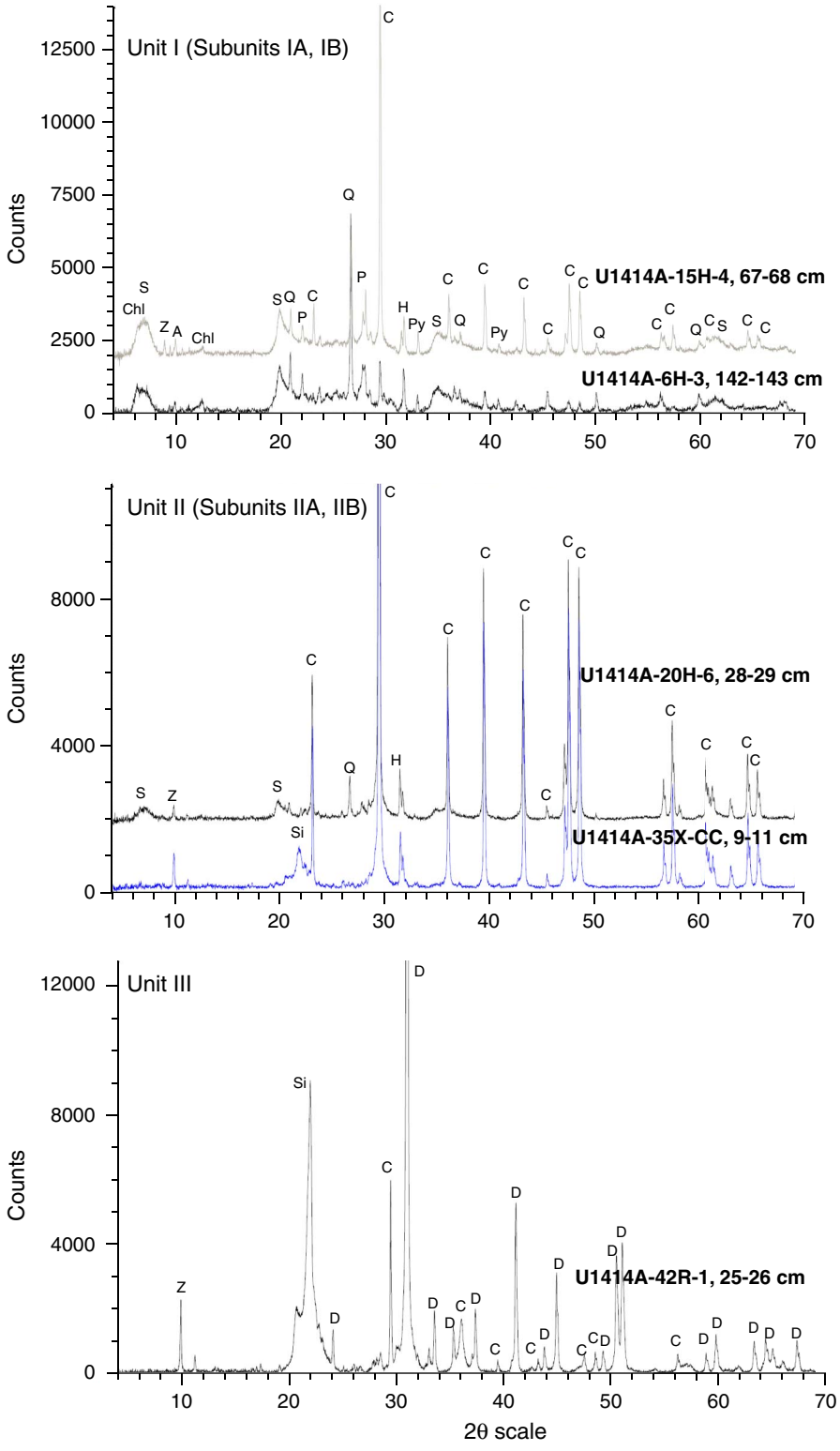

Figure F15. Relative proportions of major mineral phases in sediment, Hole U1414A.

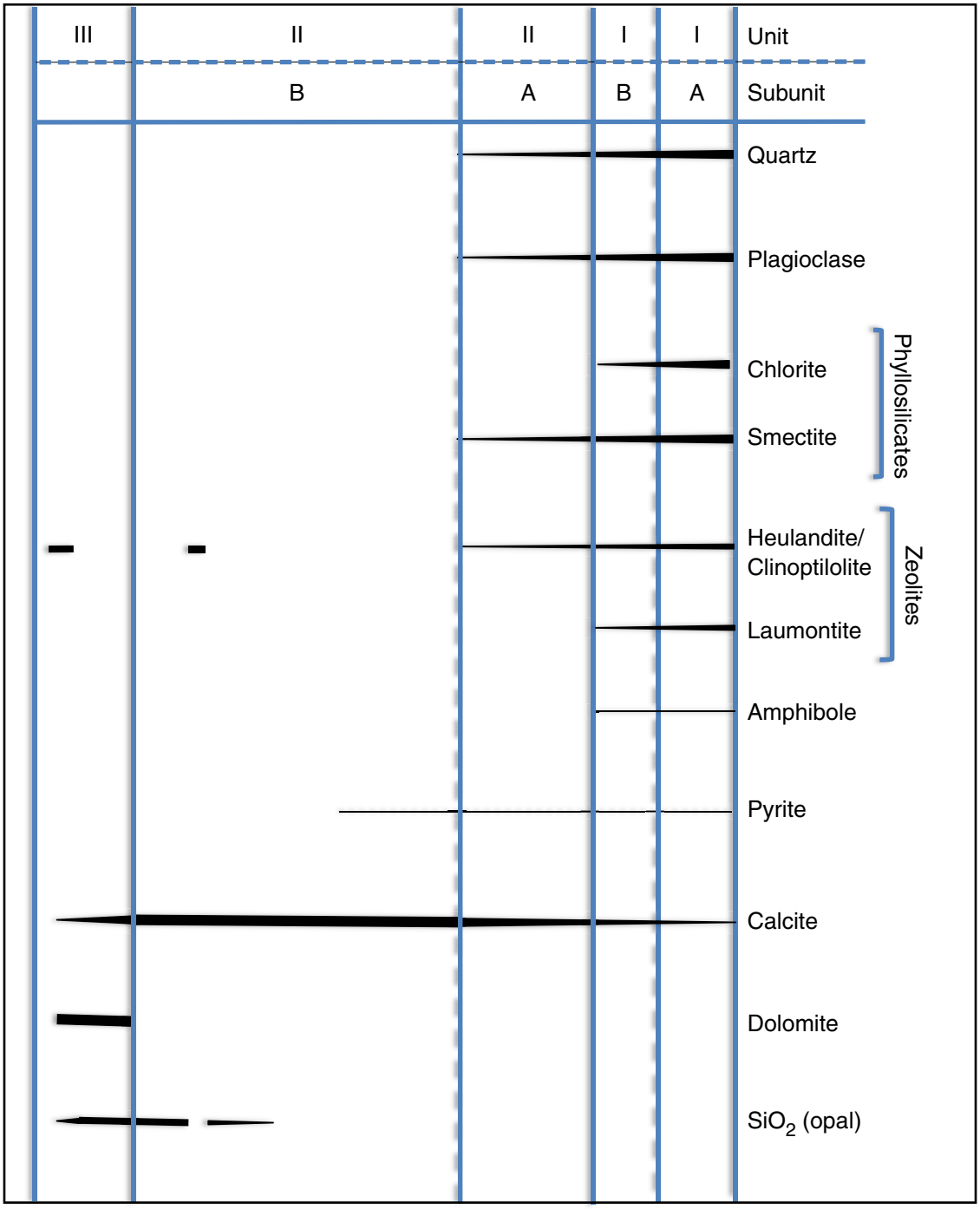

Figure F16. Vesicle and phenocryst abundance with basement lithostratigraphy, Hole U1414A.

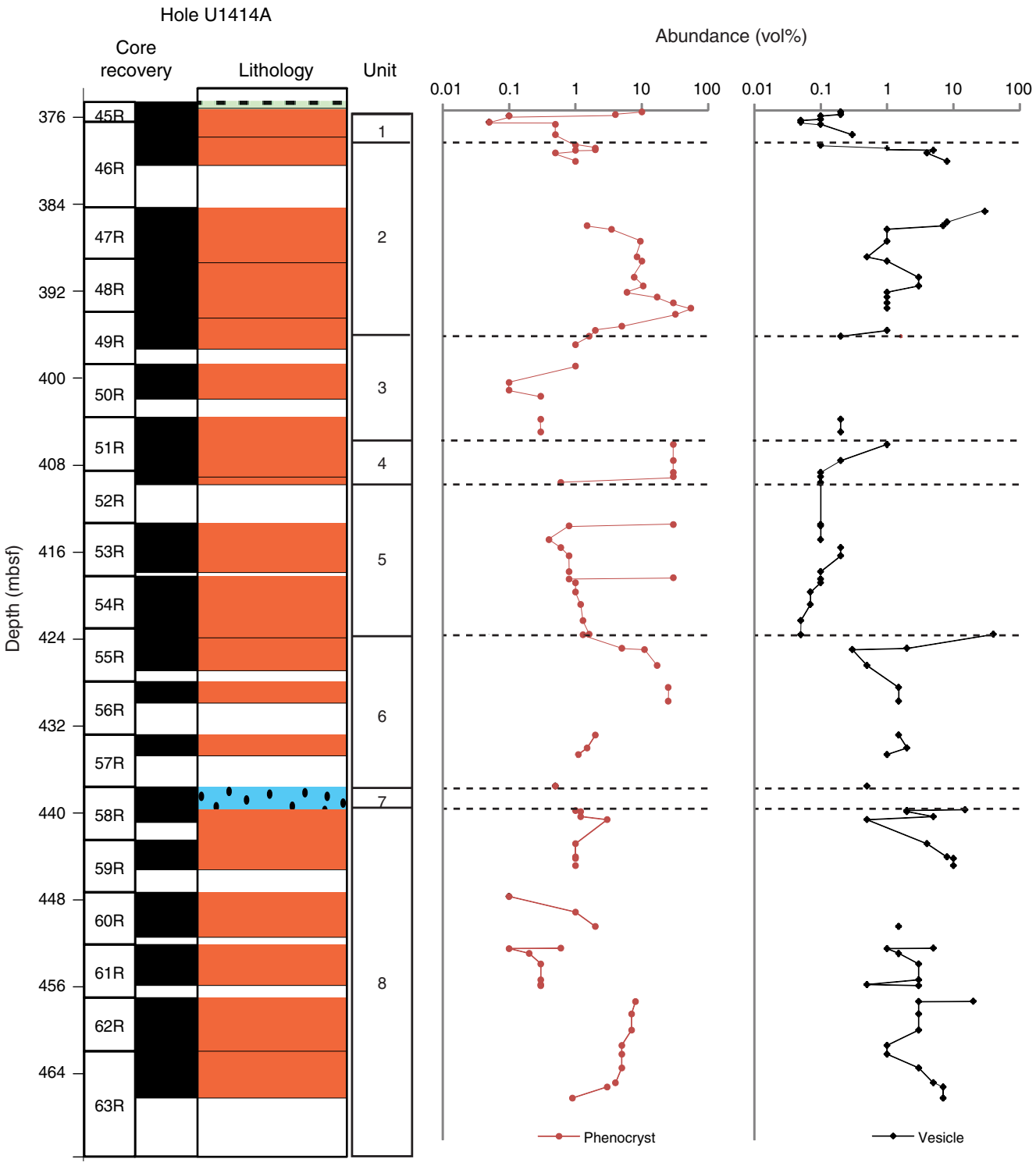

Figure F17. Core images and photomicrographs of igneous textures and their relationship to lava flows, Hole U1414A.

Igneous textures on or near top of massive flow (Unit 2):

344-U1414A-47R-1, 85-93 cm

Highly vesicular

Microcrystalline groundmass

Slight to moderate alteration

Photomicrograph of Thin Section 20 (344-U1414A-47R-1, 89-93 cm)

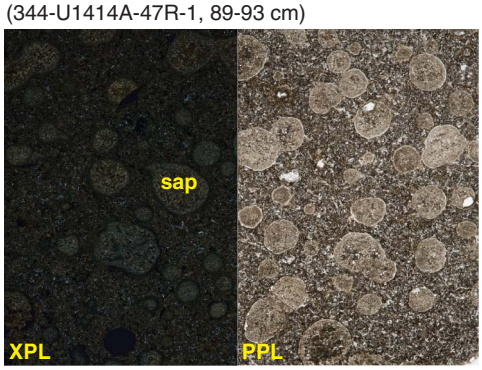

Igneous textures in middle of massive flow (Unit 2):

344-U1414A-49R-1, 94-102 cm

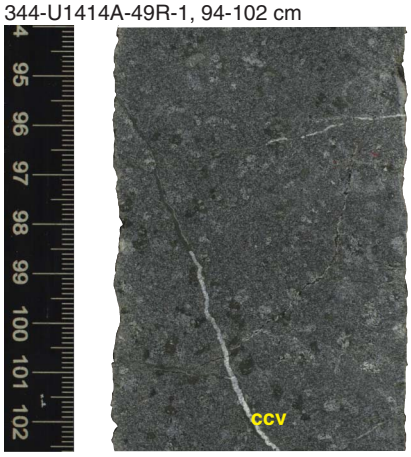

Abundant phenocrysts

Microcrystalline to fine-grained groundmass

Slight alteration

Photomicrograph of Thin Section 23 (344-U1414A-49R-1, 95-98 cm)

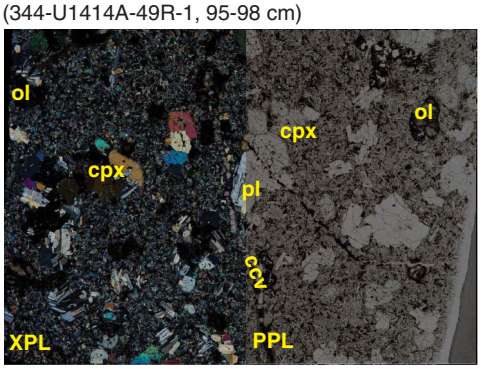

Igneous textures at bottom of massive flow (Unit 2):

344-U1414A-49R-2, 47-57 cm

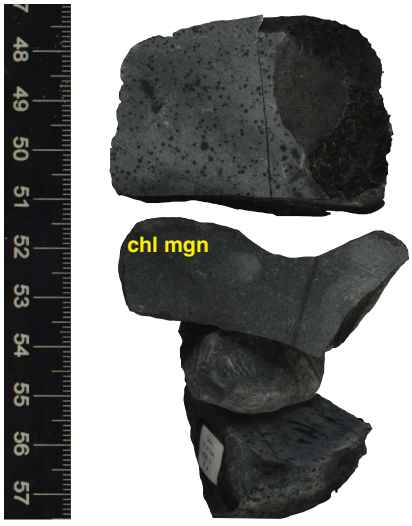

Microcrystalline to cryptocrystalline groundmass

Aphyric

Chilled margin

Recovery poor, comprising of rubble and loose fragments

Slight to moderate alteration

ol = olivine
cpx = clinopyroxene
pl = plagioclase
XPL= cross-polarized light
PPL = plane-polarized light
ccv = calcium carbonate vein
sap = saponite
chl mgn = chilled margin

Figure F18. Core images and photomicrographs of phenocrysts, Hole U1414A. cpx = clinopyroxene, pl = plagioclase, ol = olivine. XPL = cross-polarized light, PPL = plane-polarized light.

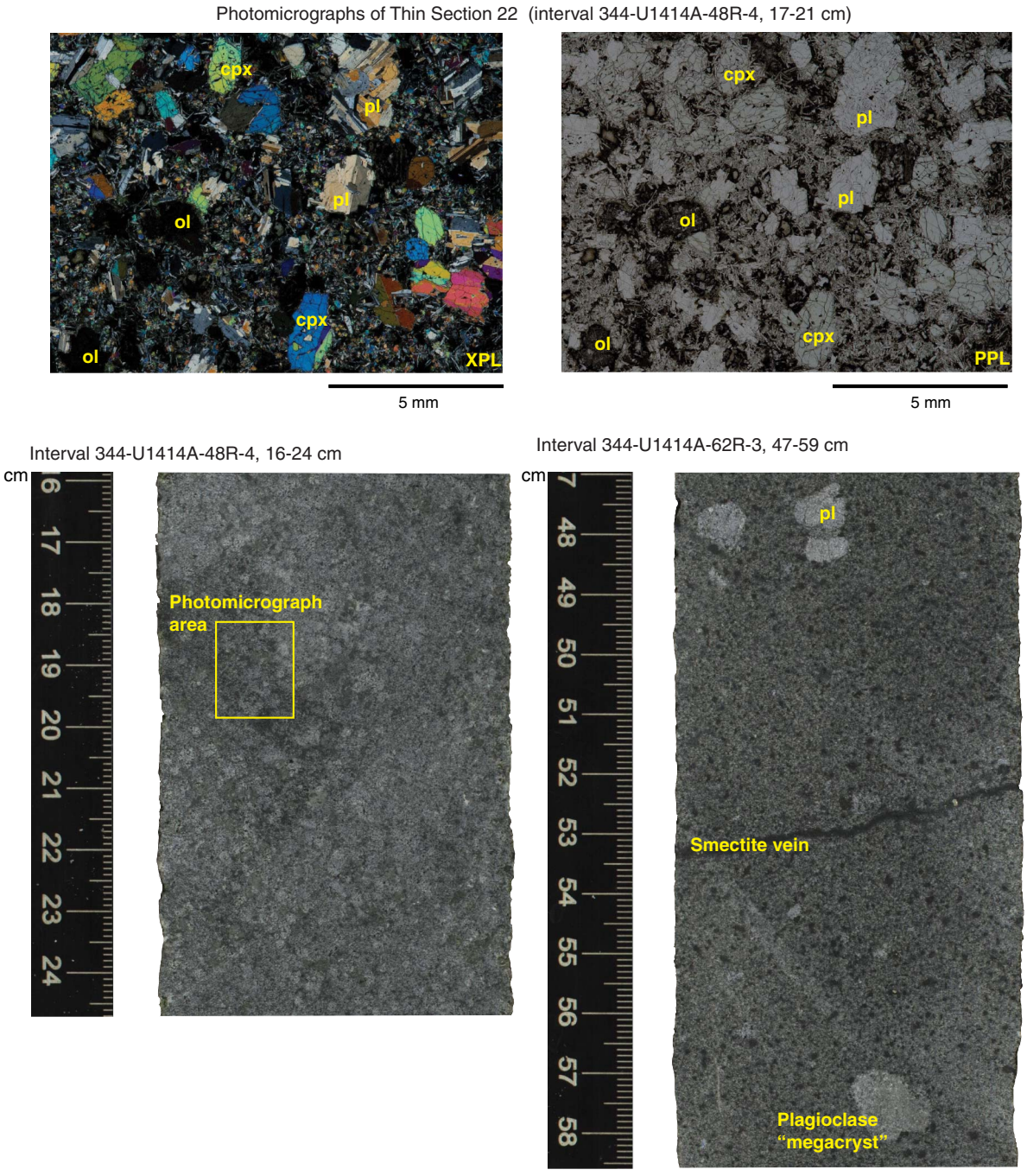

Figure F19. Core images and photomicrographs of alteration features within basement, Hole U1414A. PPL = plane-polarized light, XPL = cross-polarized light. (Continued on next page.)

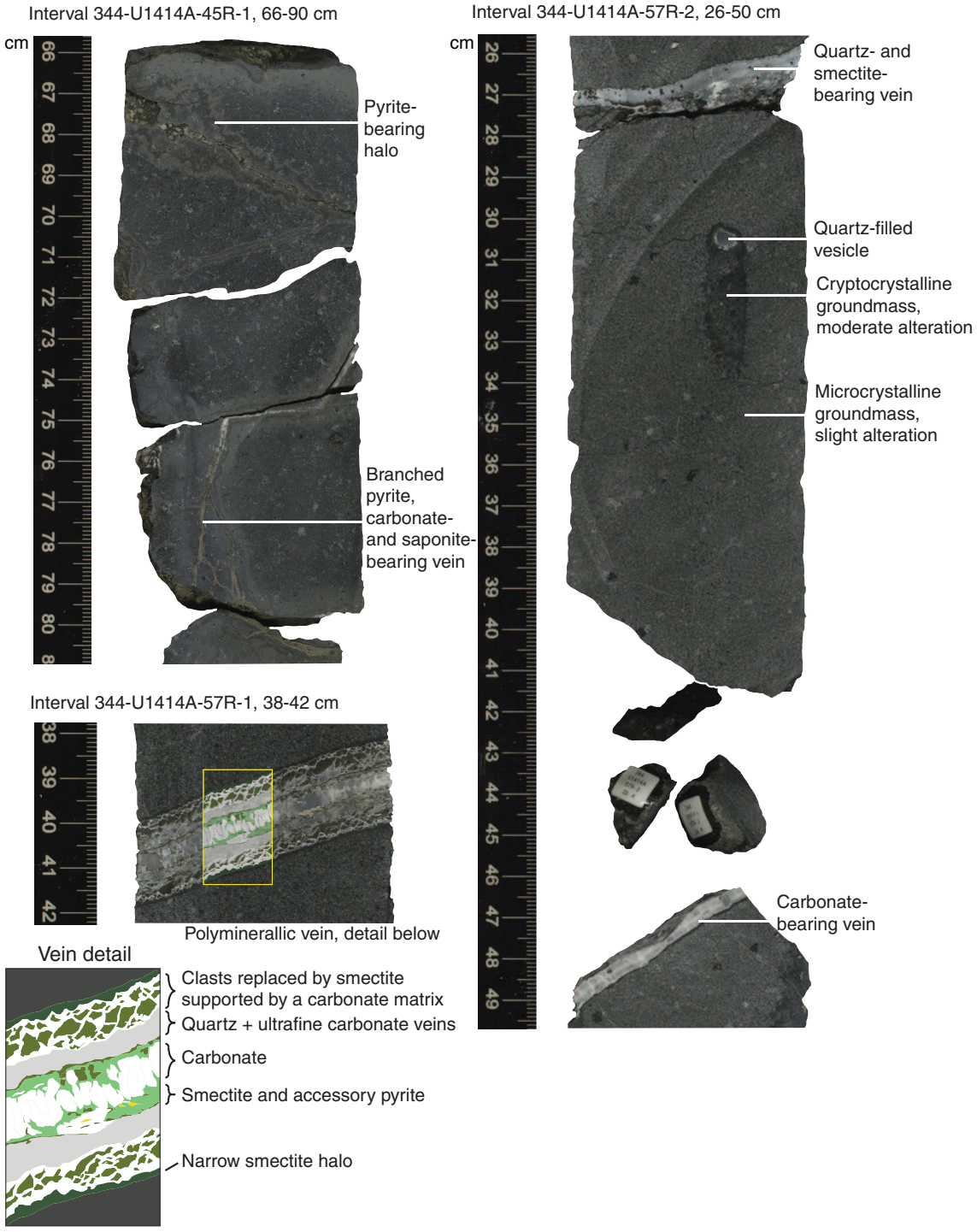

Figure F19 (continued).

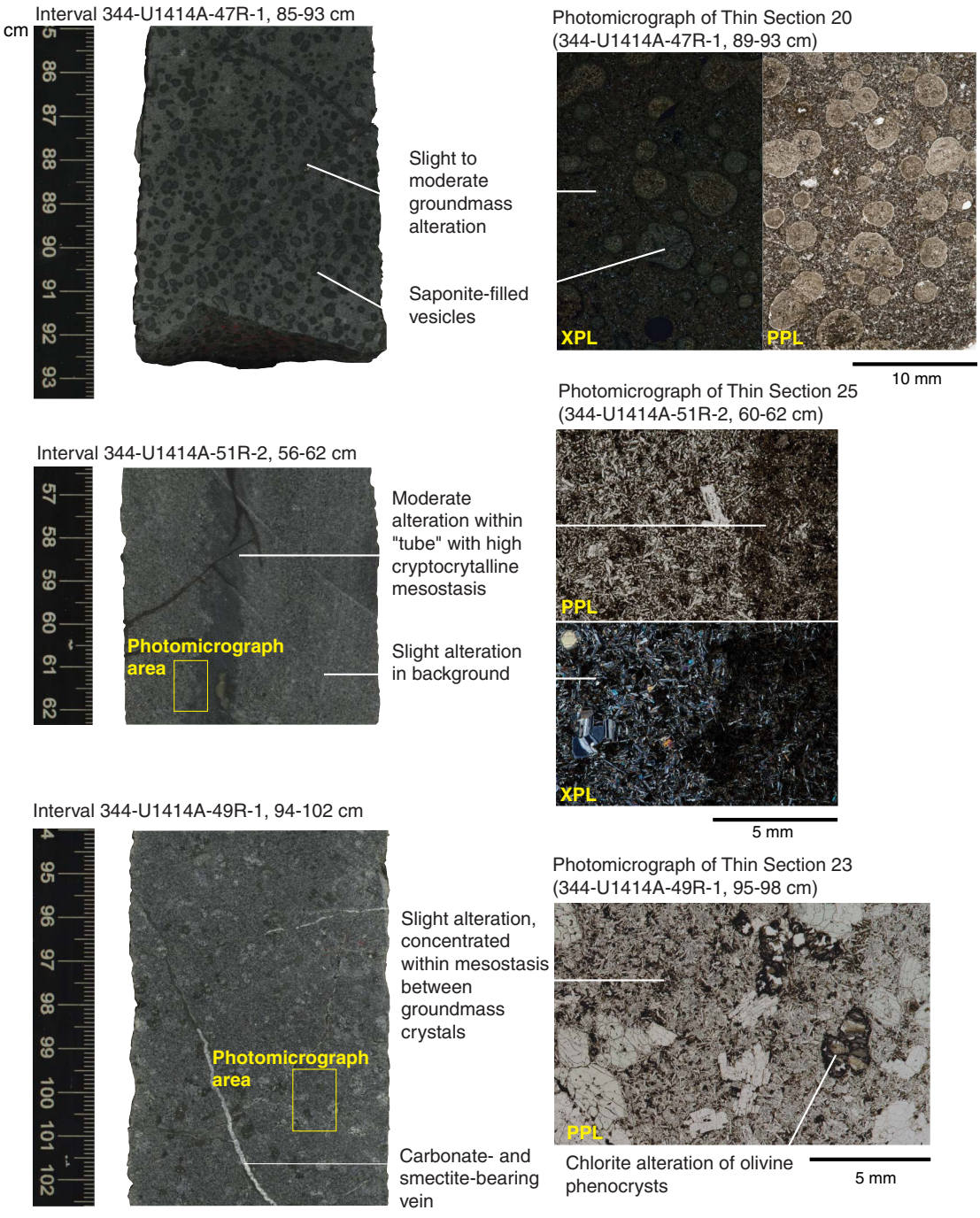

Figure F20. Core images and photomicrographs of basaltic breccia, Hole U1414A. PPL = plane-polarized light, XPL = cross-polarized light.

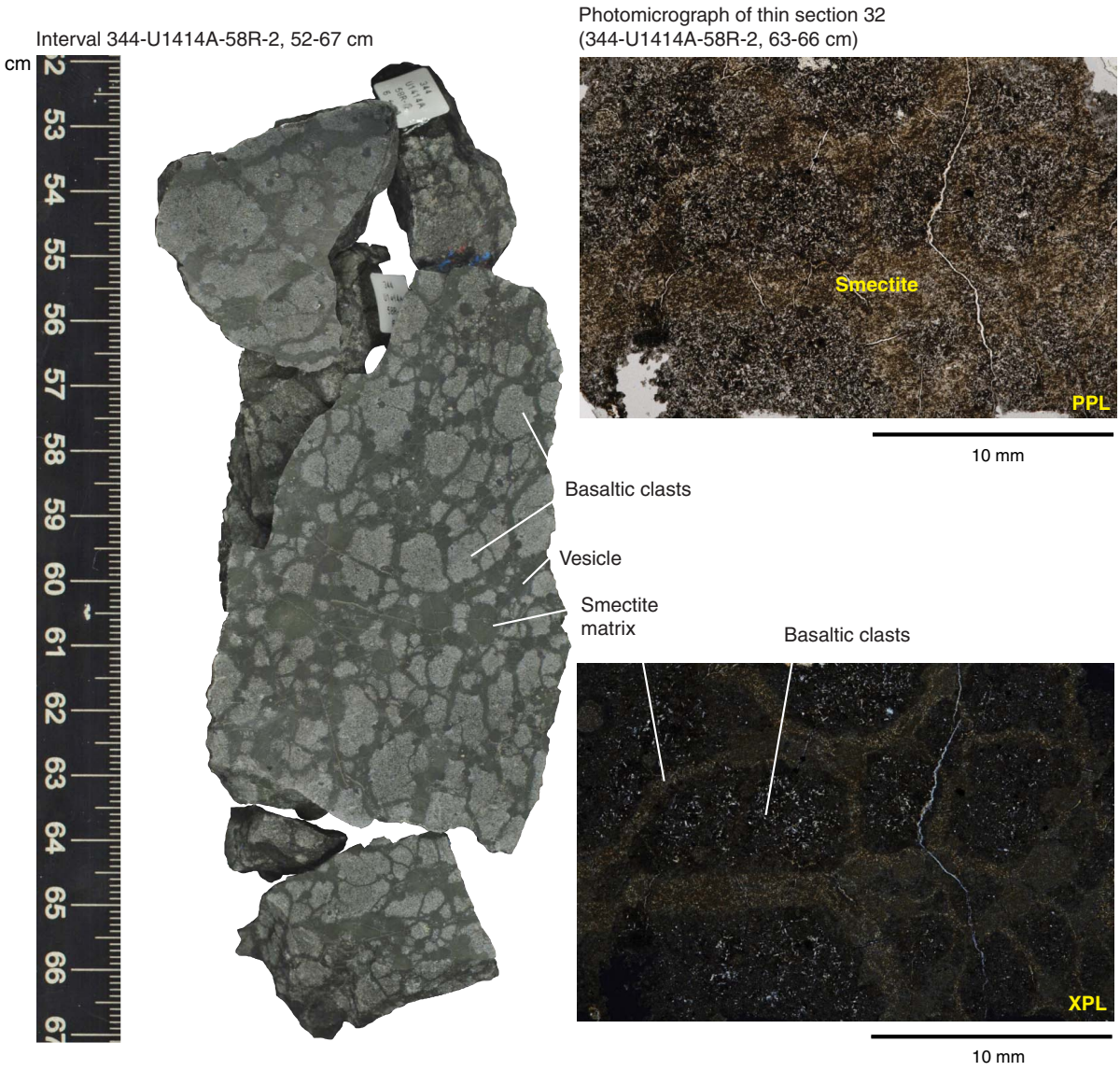

Figure F21. Distribution of veins, vesicles, and breccia, Hole U1414A.

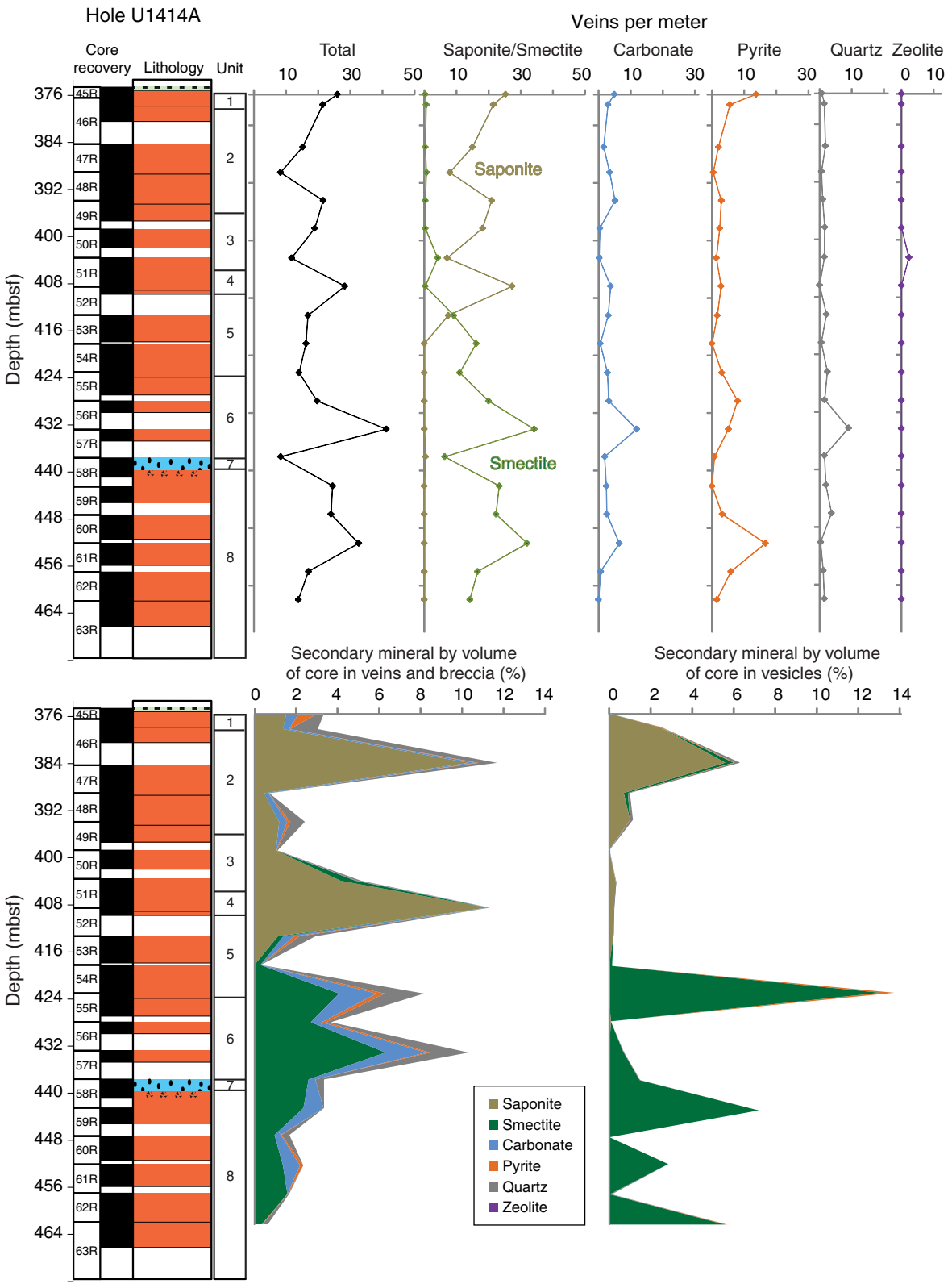

Figure F22. Distribution of halos, Hole U1414A.

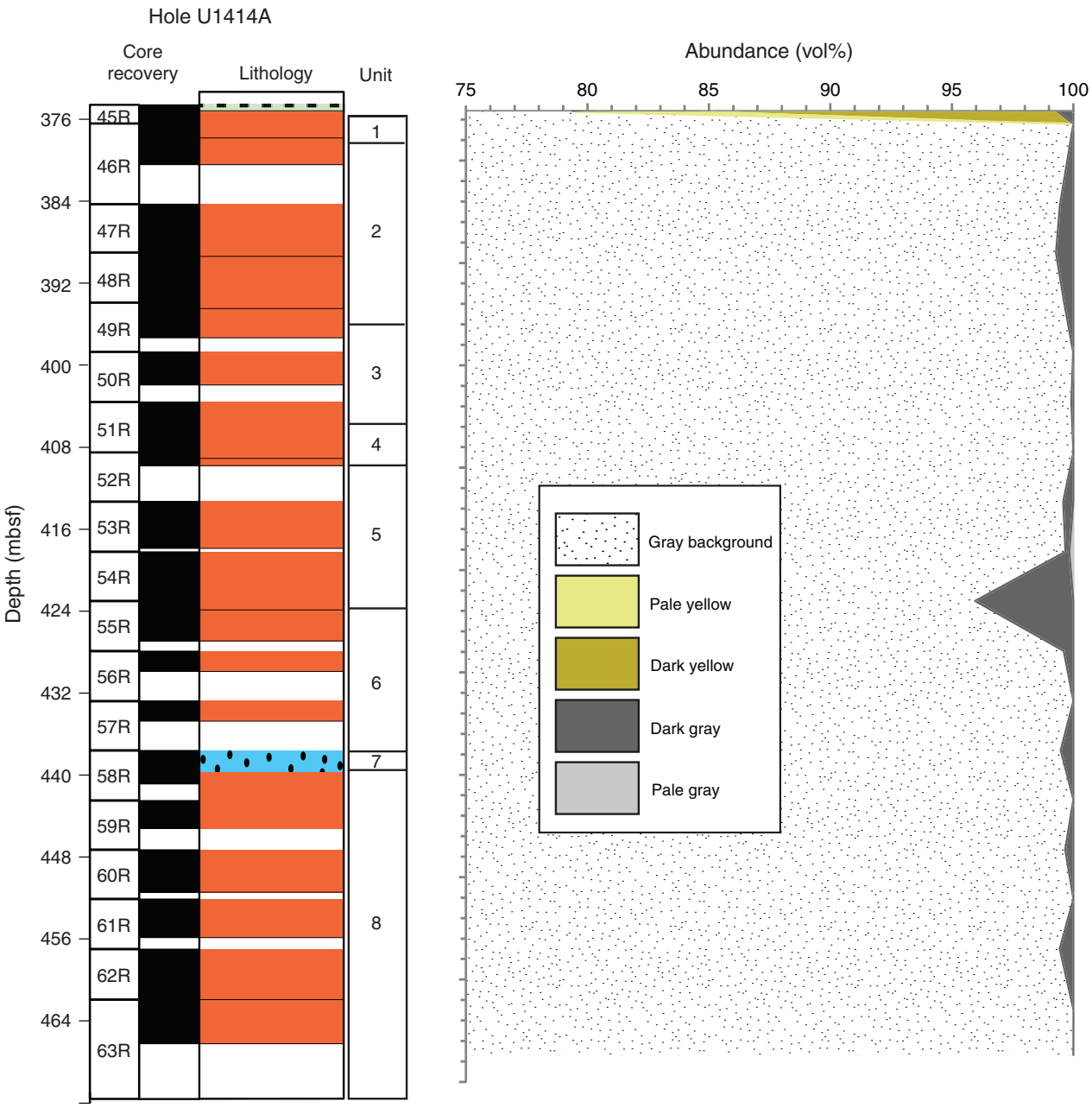

Figure F23. Cartoon illustrating the relative timing and mode of secondary mineral emplacement in igneous basement, Hole U1414A.

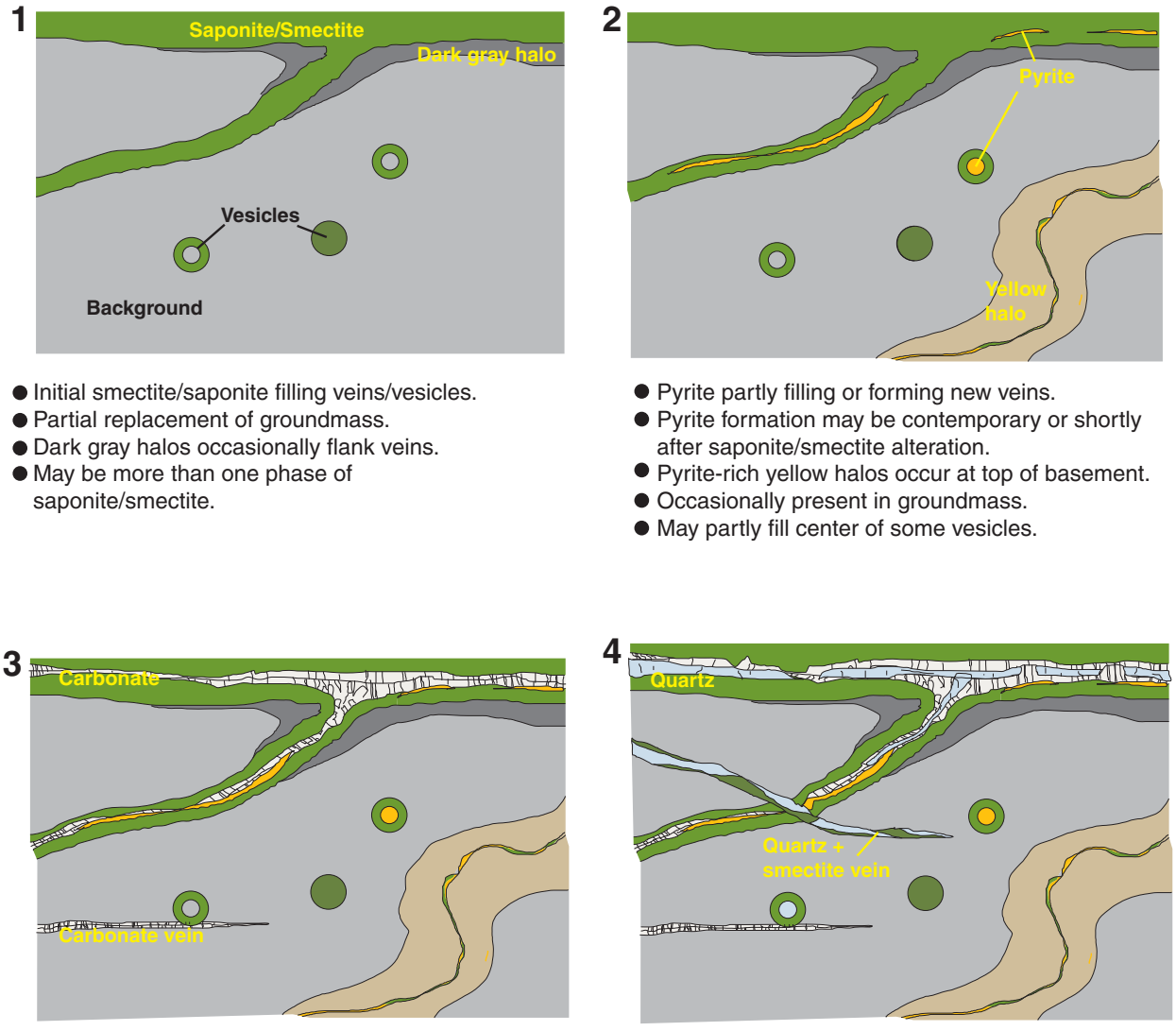

- Initial smectite/saponite filling veins/vesicles.
- Partial replacement of groundmass.
- Dark gray halos occasionally flank veins.
- May be more than one phase of saponite/smectite.

- Pyrite partly filling or forming new veins.
- Pyrite formation may be contemporary or shortly after saponite/smectite alteration.
- Pyrite-rich yellow halos occur at top of basement.
- Occasionally present in groundmass.
- May partly fill center of some vesicles.

- Multiple episodes of carbonate veins crosscut or fill centers of veins that have reopened.
- Carbonate precipitation may or may not be continous throughout lifetime of Site U1414 basement.
- Multiple carbonate emplacement phases observed within some veins.
- Carbonate veins observed to crosscut saponite/smectite veins.

- Late-stage quartz fills centers of veins, crosscuts earlier veins, may partly fill vesicles.
- May be associated with additional late-stage smectite alteration within polymineralic veins.
- Quartz +/- smectite veins observed to crosscut earlier smectite and/or carbonate veins.

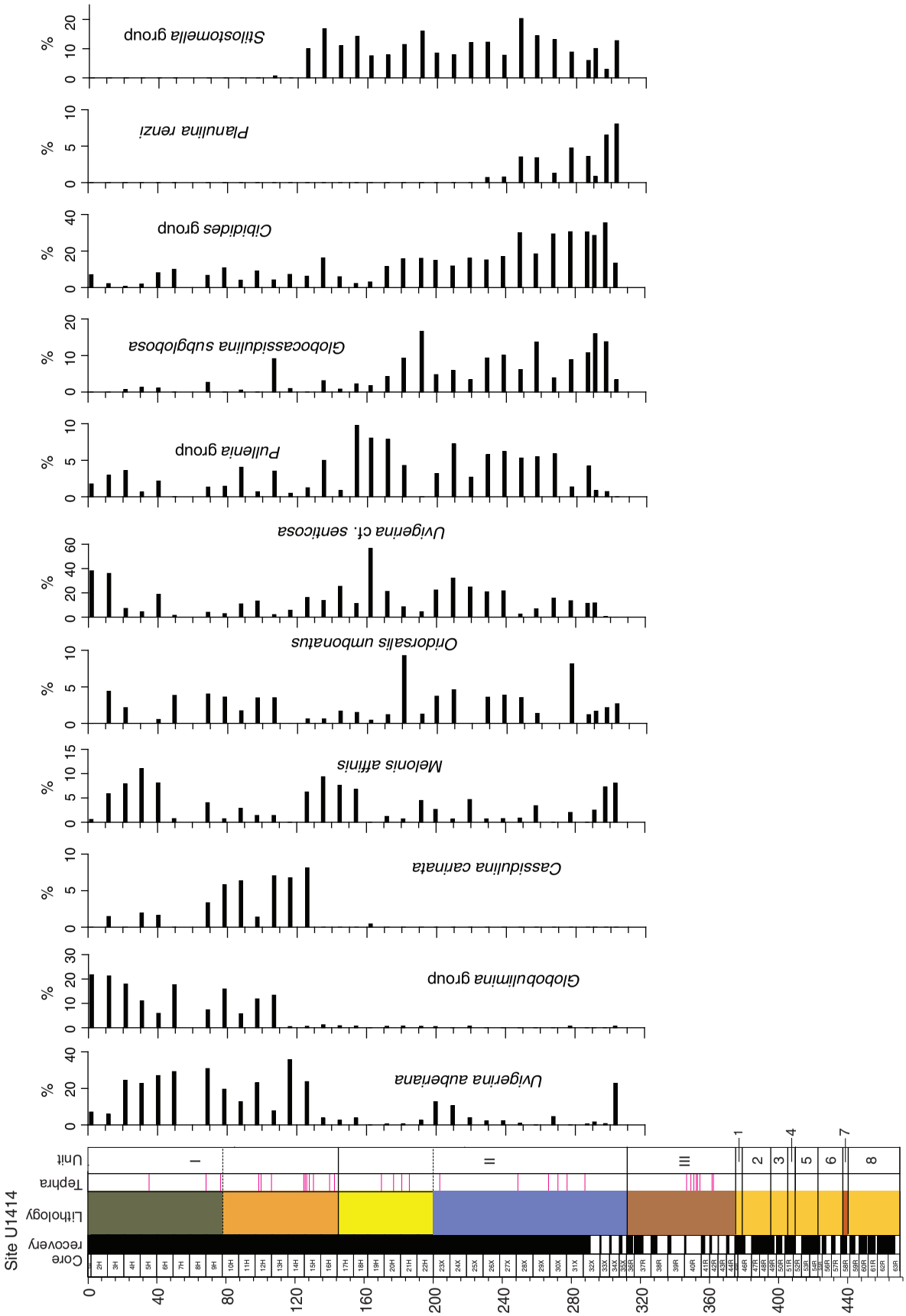

Figure F24. Relative abundance of the most characteristic benthic foraminifer assemblages at Site U1414. The *Stilostomella* group includes the same species as reported in **"Paleontology and biostratigraphy"** in the "Input Site U1381" chapter (Harris et al., 2013a).

Figure F25. Plot of bedding dips, foliation, and fault and vein dip angles, Hole U1414A.

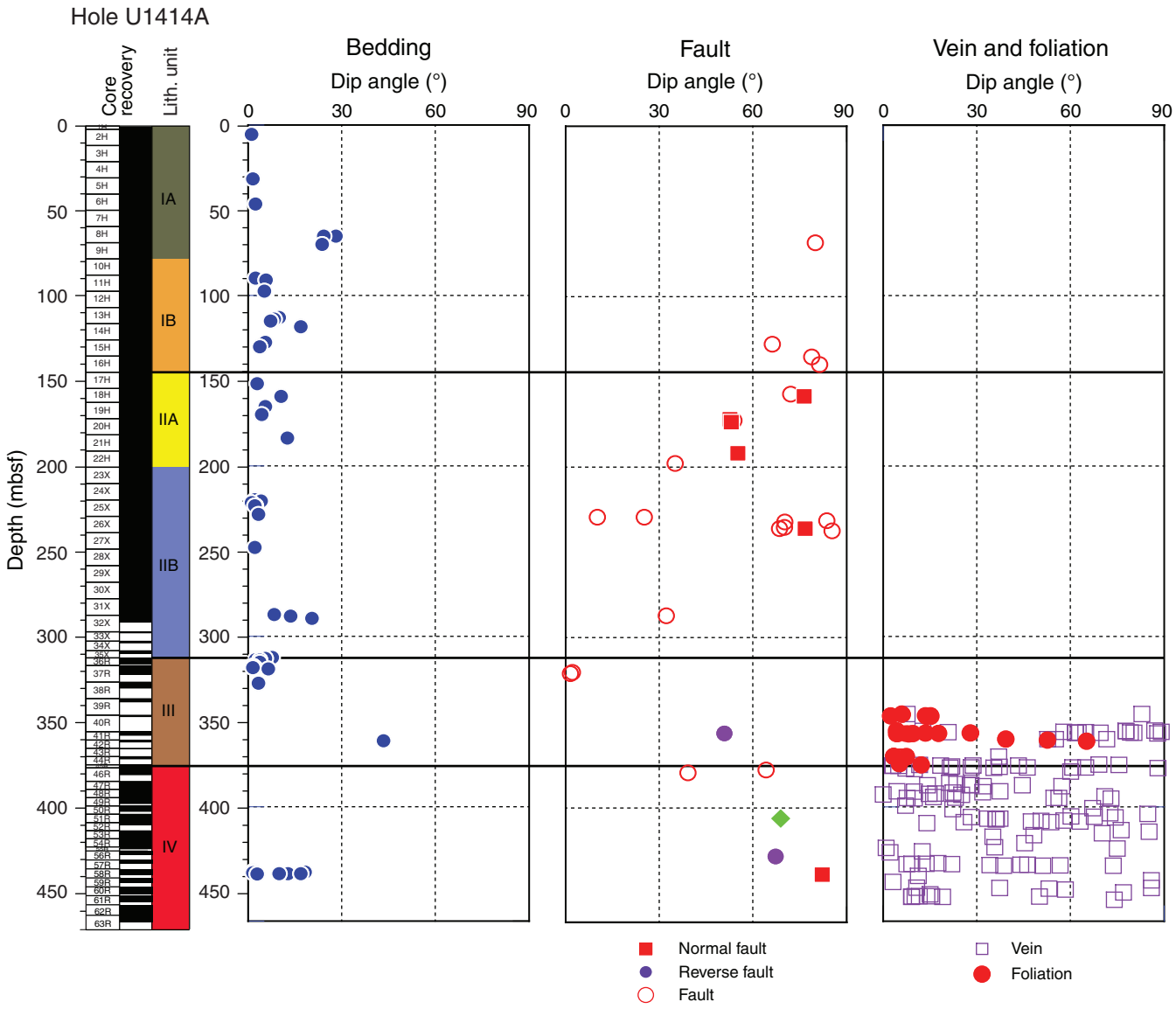

Figure F26. Stereoplot diagrams (lower hemisphere projection) showing the orientation of (**A**) bedding plane and (**B**) faults, Hole U1414A. Data were collected from lithostratigraphic Units I and II.

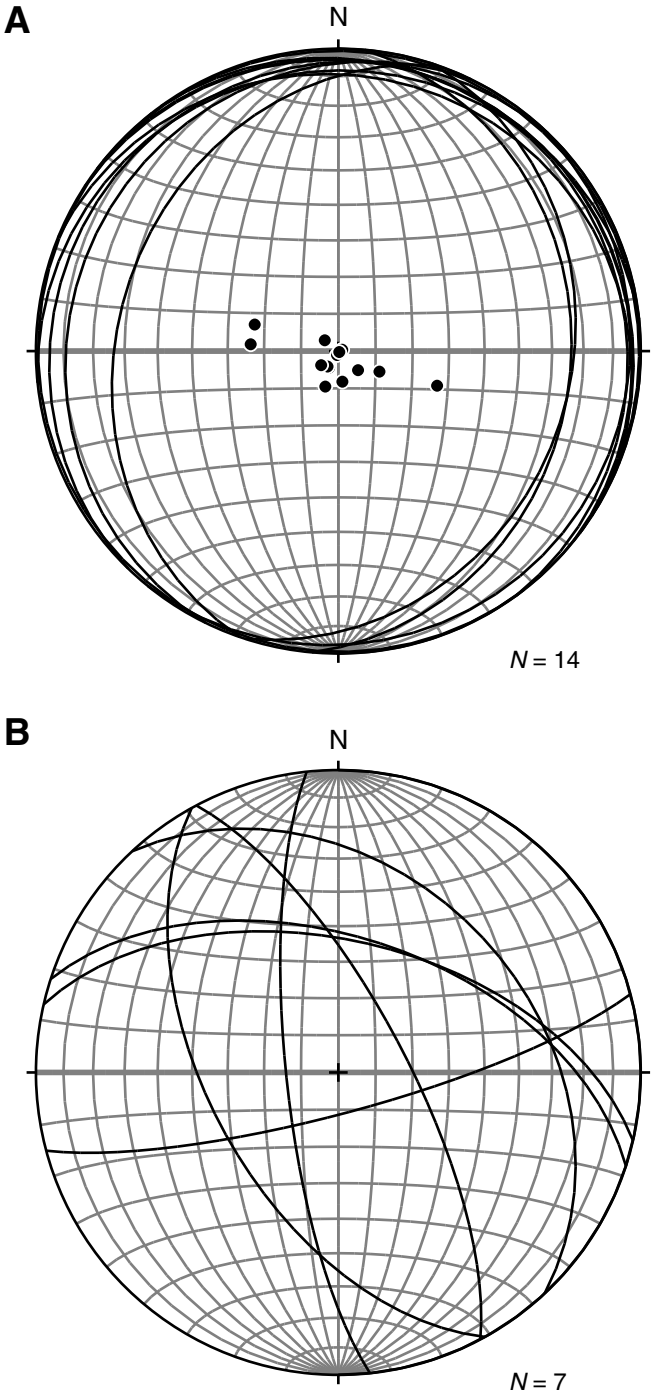

Figure F27. Photograph of clasts derived from bioturbation structures embedded within the fine-grained foliated matrix (interval 344-U1414A-41R-2, 82–89 cm).

Figure F28. Photograph of carbonate-filled veins (interval 344-U1414A-41R-2, 60–68 cm).

Figure F29. Downhole profiles for salinity, chloride, potassium, and sodium, Site U1414. Blue arrows = bottom seawater values. Dashed lines = lithostratigraphic unit and subunit boundaries IA, IB, IIA, IIB, and III.

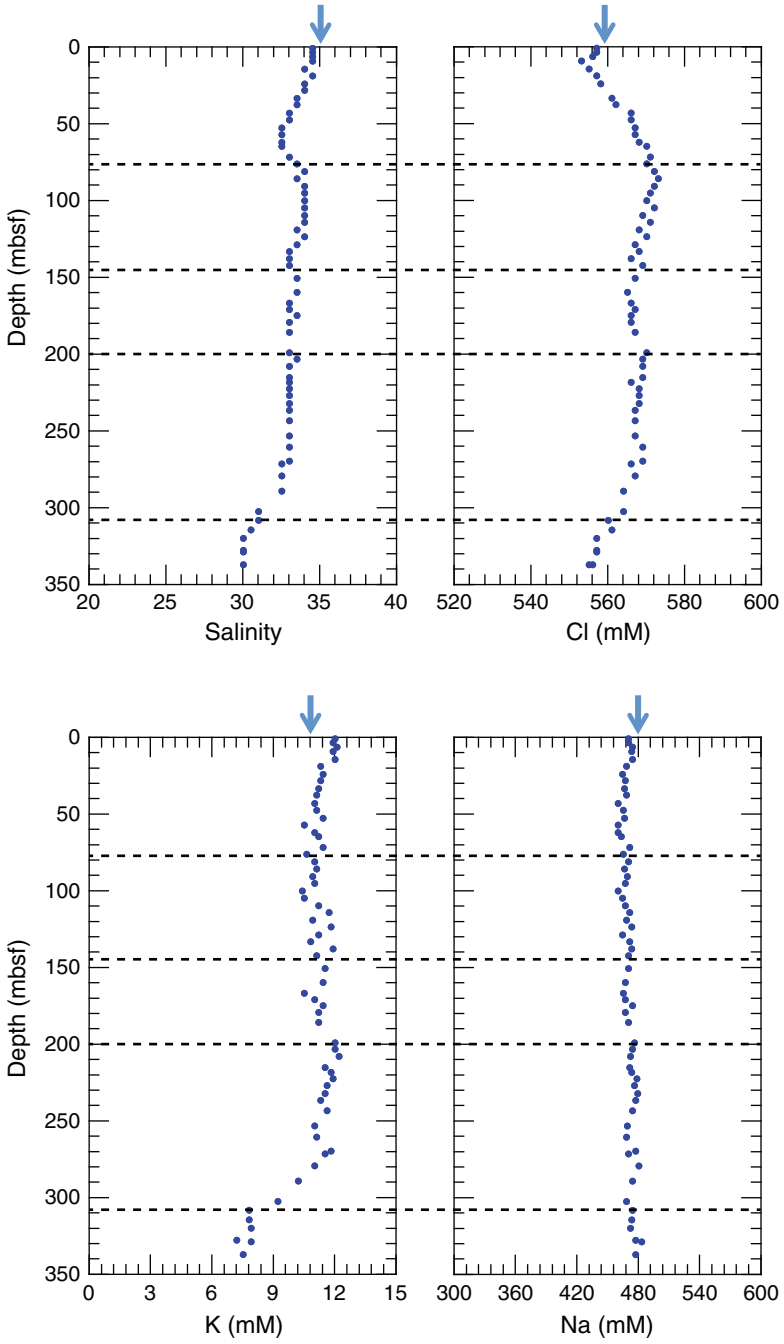

Figure F30. Downhole profiles for alkalinity, sulfate, ammonium, calcium, and magnesium, Site U1414. Blue arrows = bottom seawater values. Dashed lines = lithostratigraphic unit and subunit boundaries IA, IB, IIA, IIB, and III.

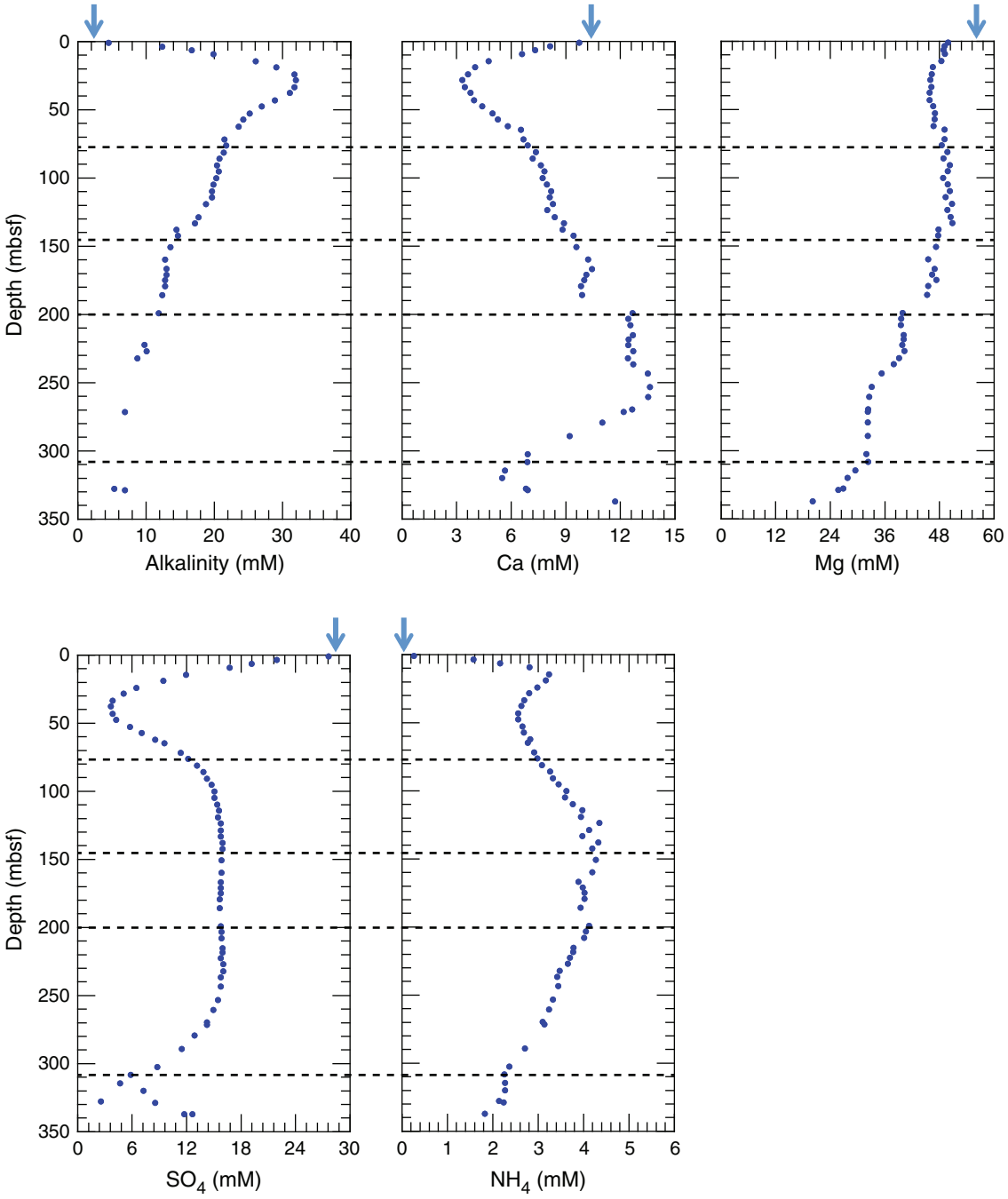

Figure F31. Downhole profiles for strontium, lithium, manganese, boron, silica, and barium, Site U1414. Blue arrows = bottom seawater values. Dashed lines = lithostratigraphic unit and subunit boundaries IA, IB, IIA, IIB, and III.

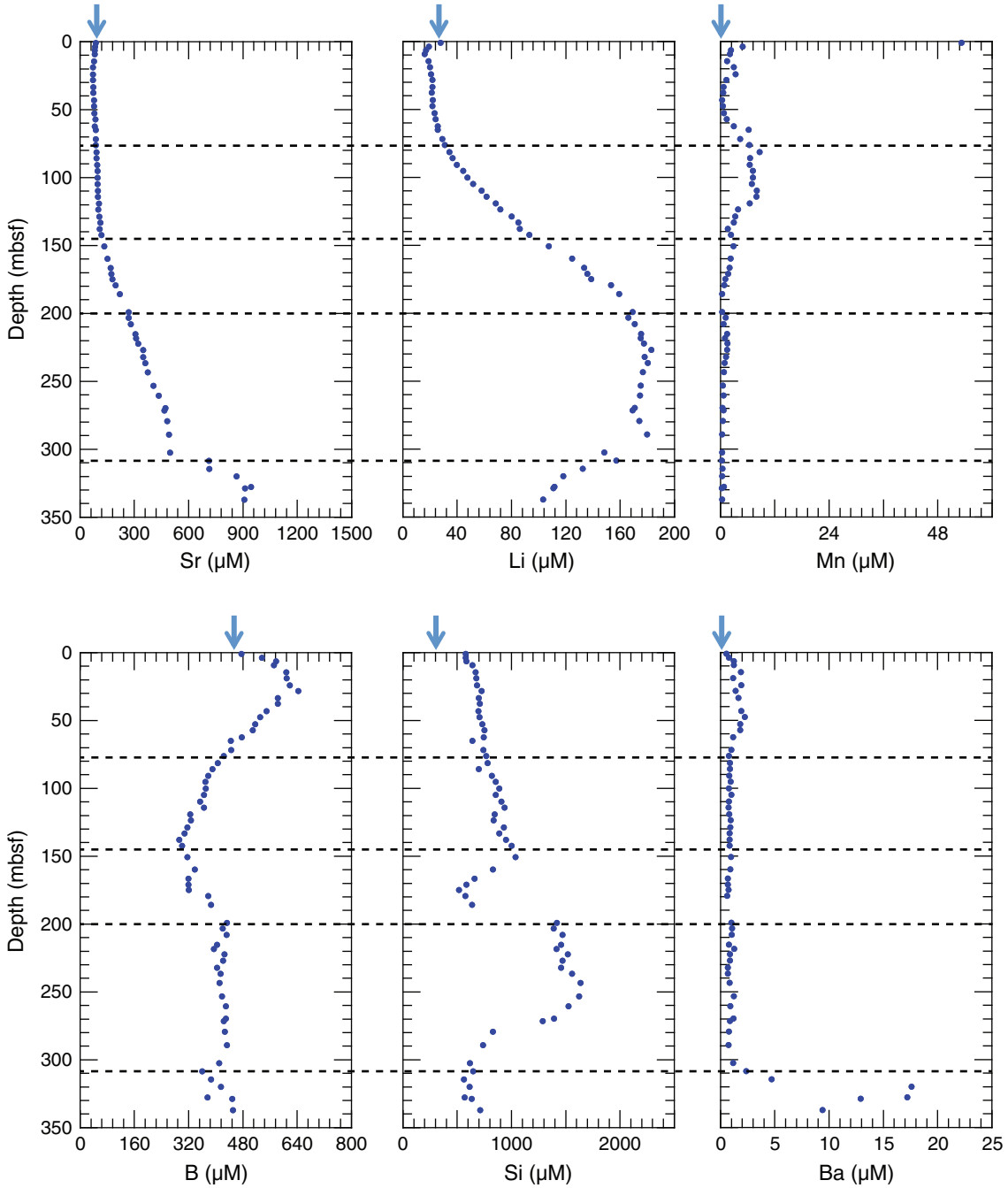

Figure F32. Downcore profiles of methane in headspace gas, Hole U1414A. Dashed lines = lithostratigraphic unit and subunit boundaries IA, IB, IIA, IIB, and III.

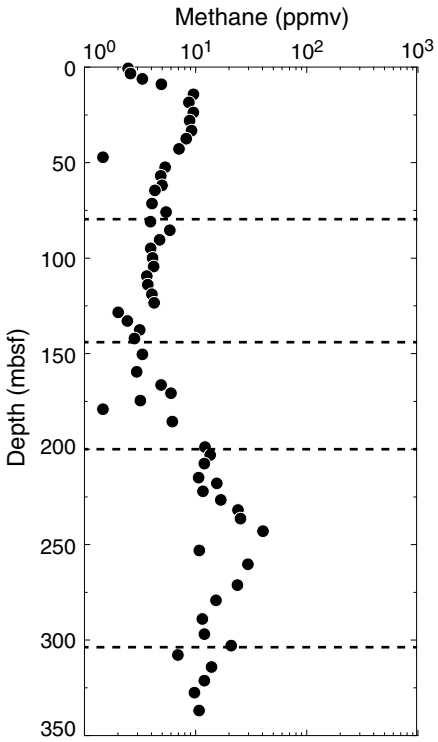

Figure F33. Downcore profiles of total carbon, inorganic carbon, total organic carbon, $CaCO_3$, total nitrogen, and C/N ratio, Hole U1414A. Dashed lines = lithostratigraphic unit and subunit boundaries IA, IB, IIA, IIB, and III.

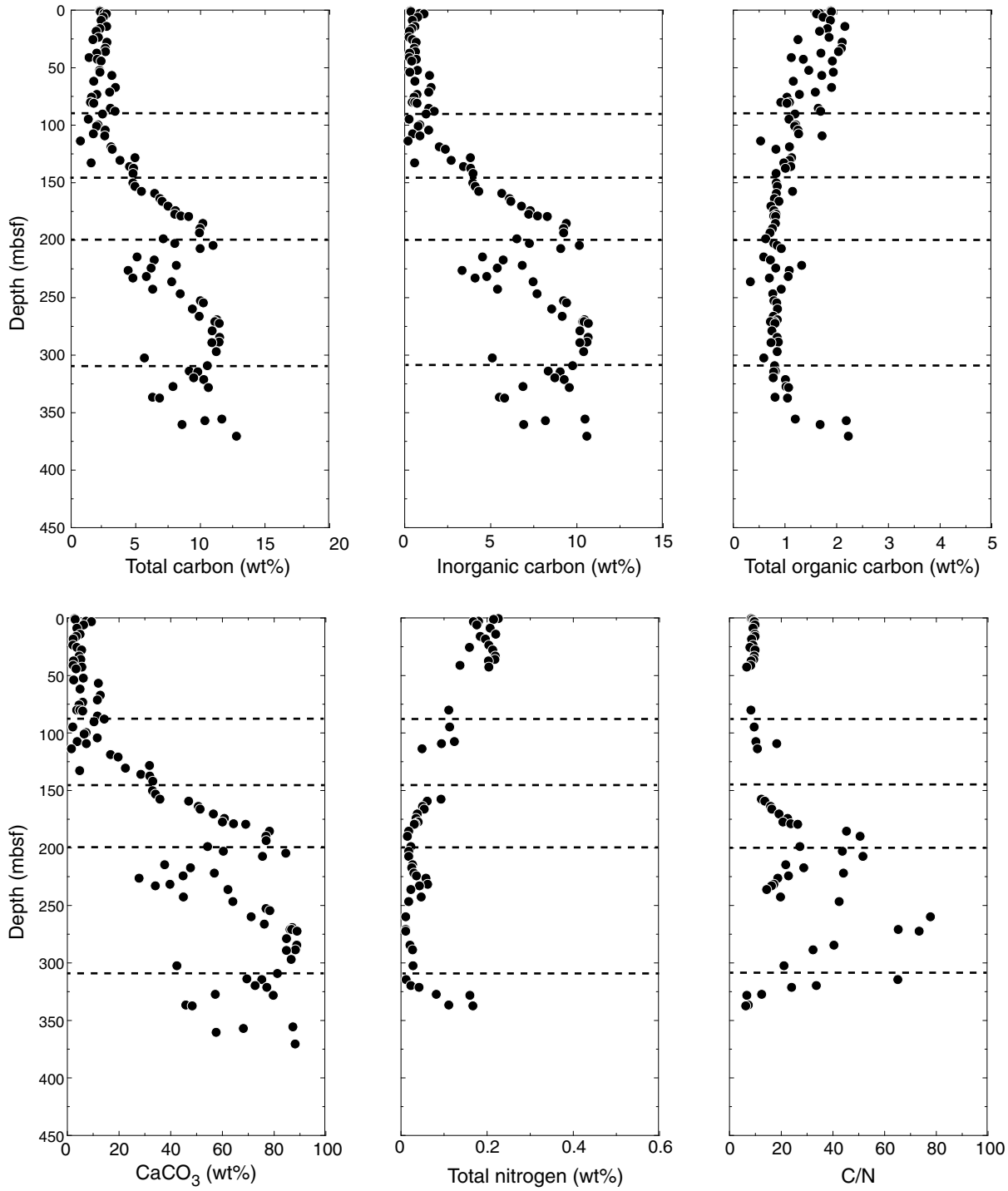

Figure F34. Gamma ray attenuation (GRA) density measured using the WRMSL and discrete sample porosity and density measured using moisture and density (MAD) mass/volume, Method C, Site U1414. Solid lines = lithostratigraphic unit boundaries, dashed lines = subunit boundaries.

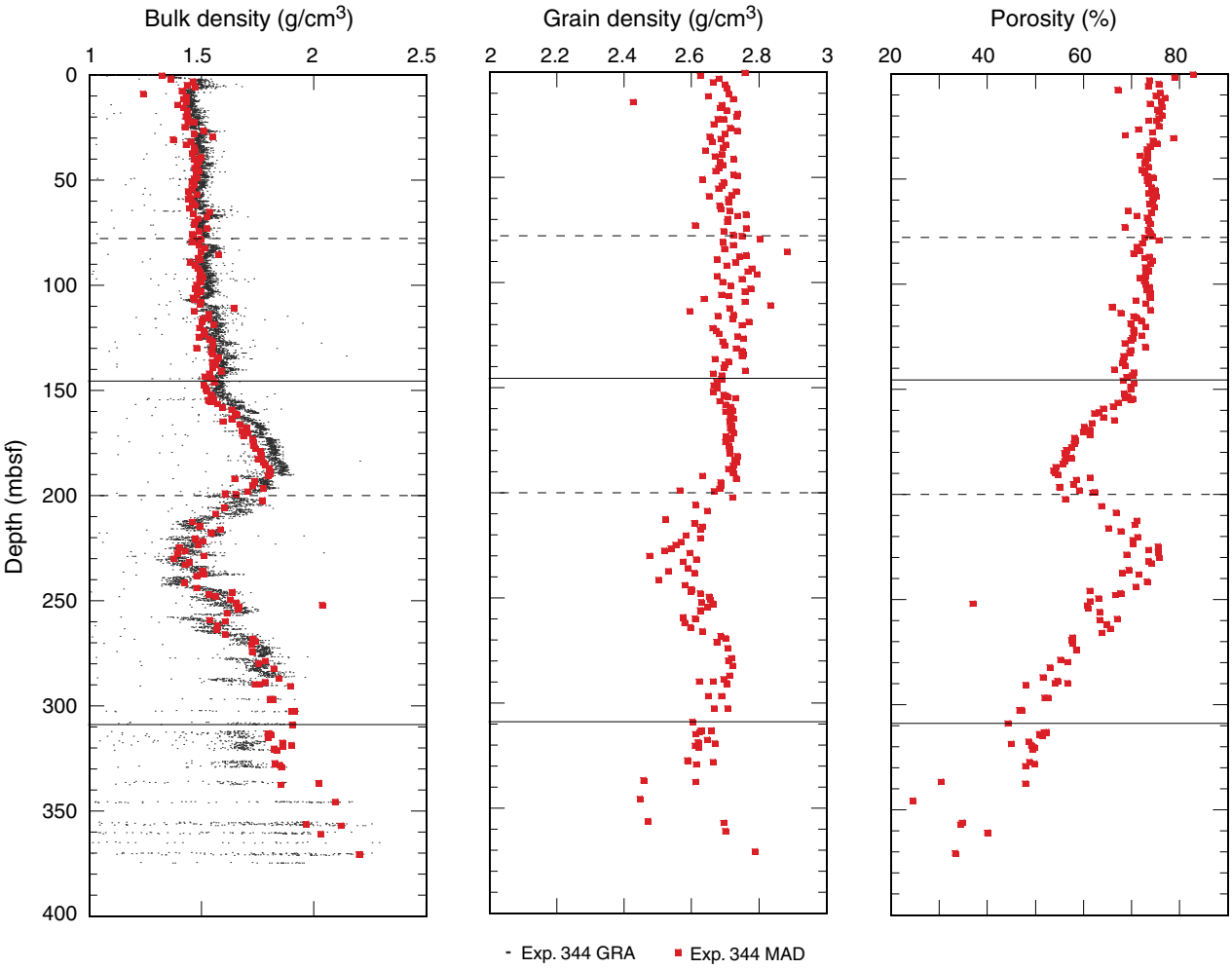

Figure F35. Magnetic susceptibility profiles, Site U1414. WRMSL = Whole-Round Multisensor Logger, SHMSL = Section Half Multisensor Logger. Solid lines = lithostratigraphic unit boundaries, dashed lines = subunit boundaries.

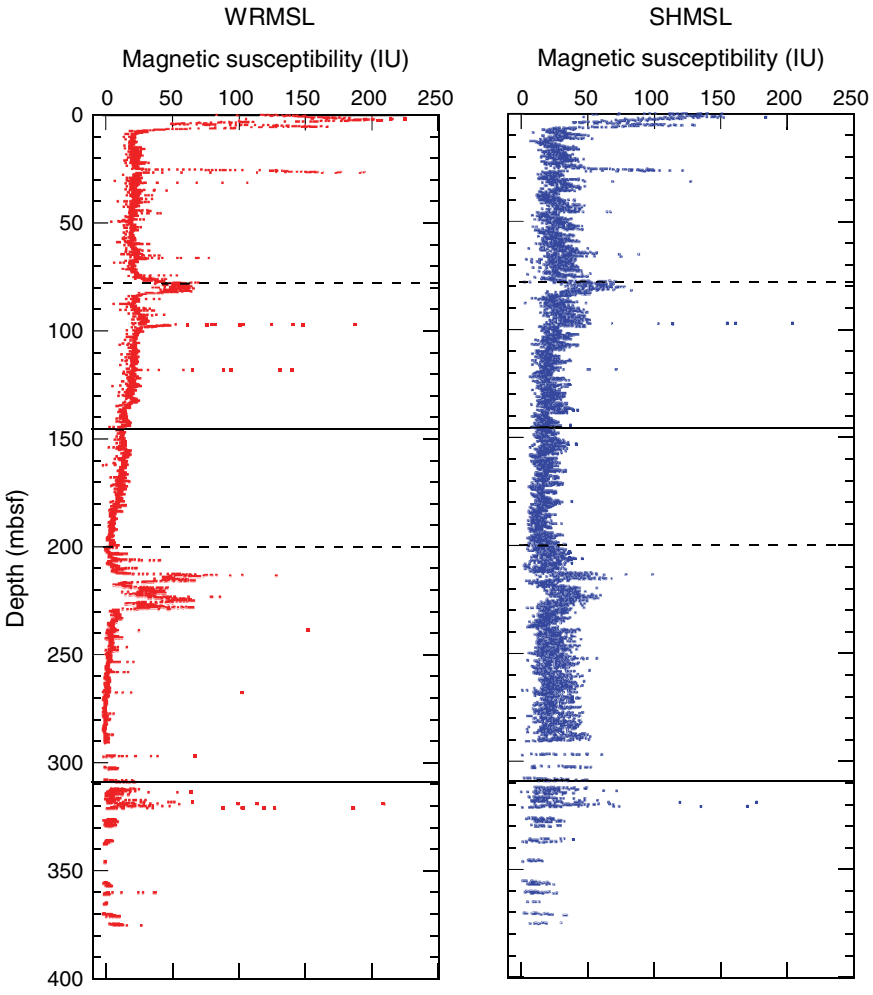

Figure F36. Natural gamma radiation (NGR) profile, Site U1414. Solid lines = lithostratigraphic unit boundaries, dashed lines = subunit boundaries.

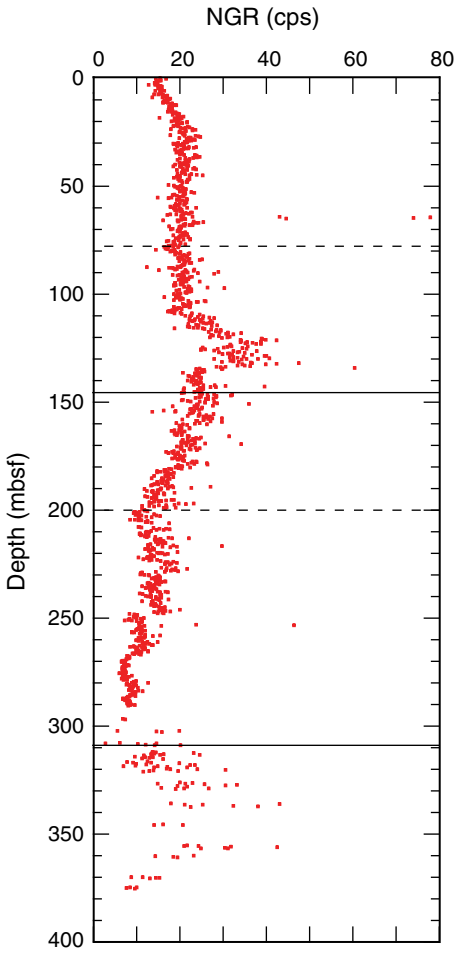

Figure F37. A. *P*-wave velocity measured on split cores and the Whole-Round Multisensor Logger (WRMSL), Hole U1414A. **B.** Same data as A, shown with expanded scale to show trends in the shallow portion of the hole. Solid lines = lithostratigraphic unit boundaries, dashed lines = subunit boundaries.

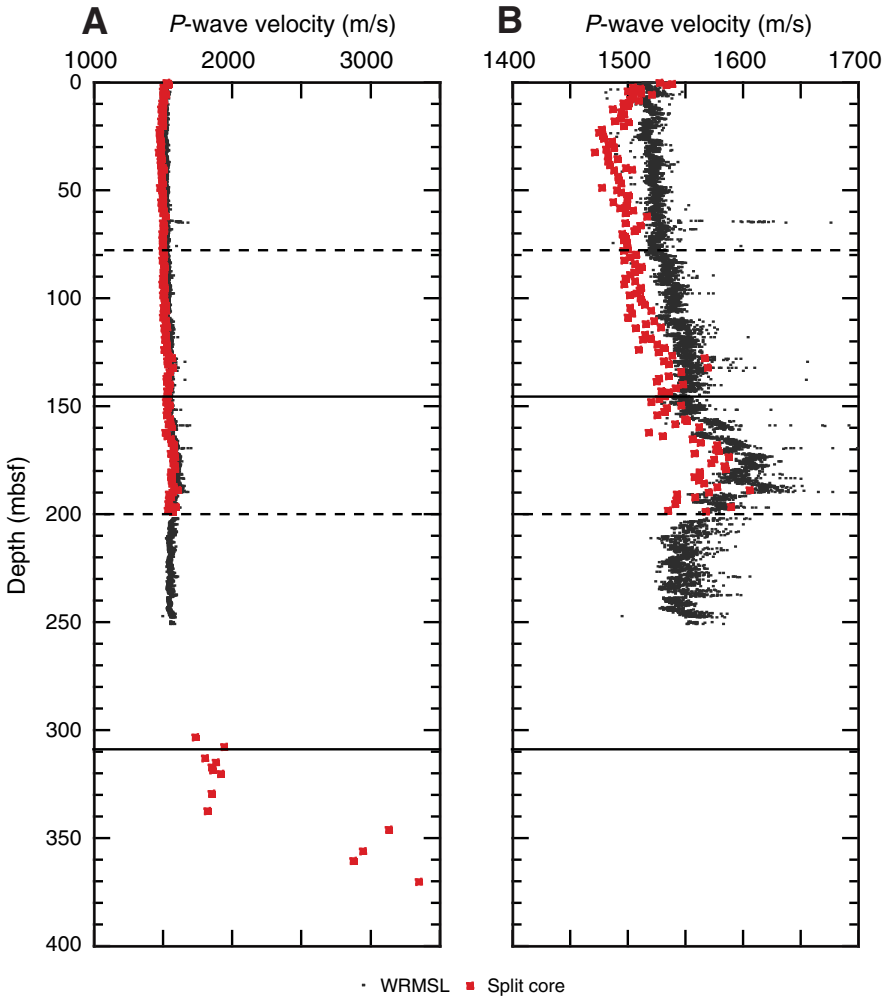

Figure F38. Thermal data, Site U1414. **A.** Thermal conductivity values. **B.** Equilibrium temperatures. Equation shows best linear fit to the four measurements, and curve shows extrapolation of temperature as a function of depth. Solid lines = lithostratigraphic unit boundaries, dashed lines = subunit boundaries.

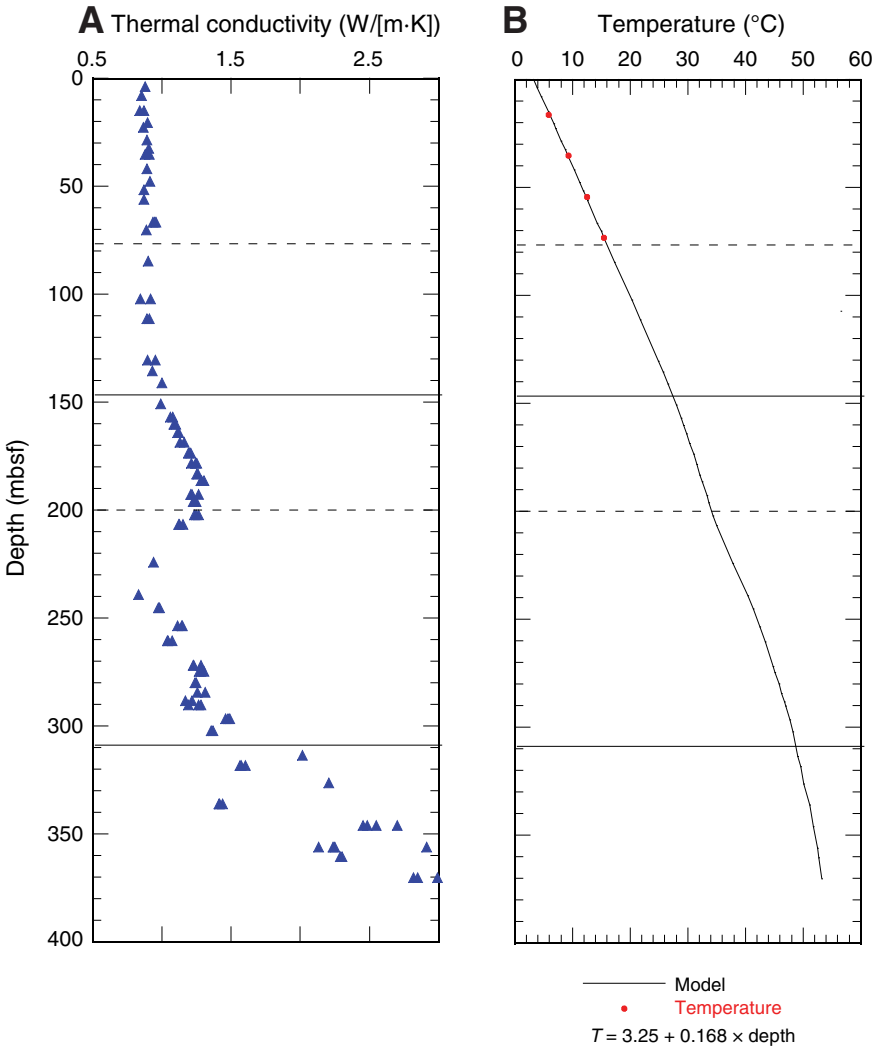

Figure F39. Strength measurements, Site U1414. **A.** Shear strength measured by AVS. **B.** Compressive strength measured using pocket (blue) and needle (red) penetrometers. **C.** Compressive strength shown on expanded scale. Solid lines = lithostratigraphic unit boundaries, dashed lines = subunit boundaries.

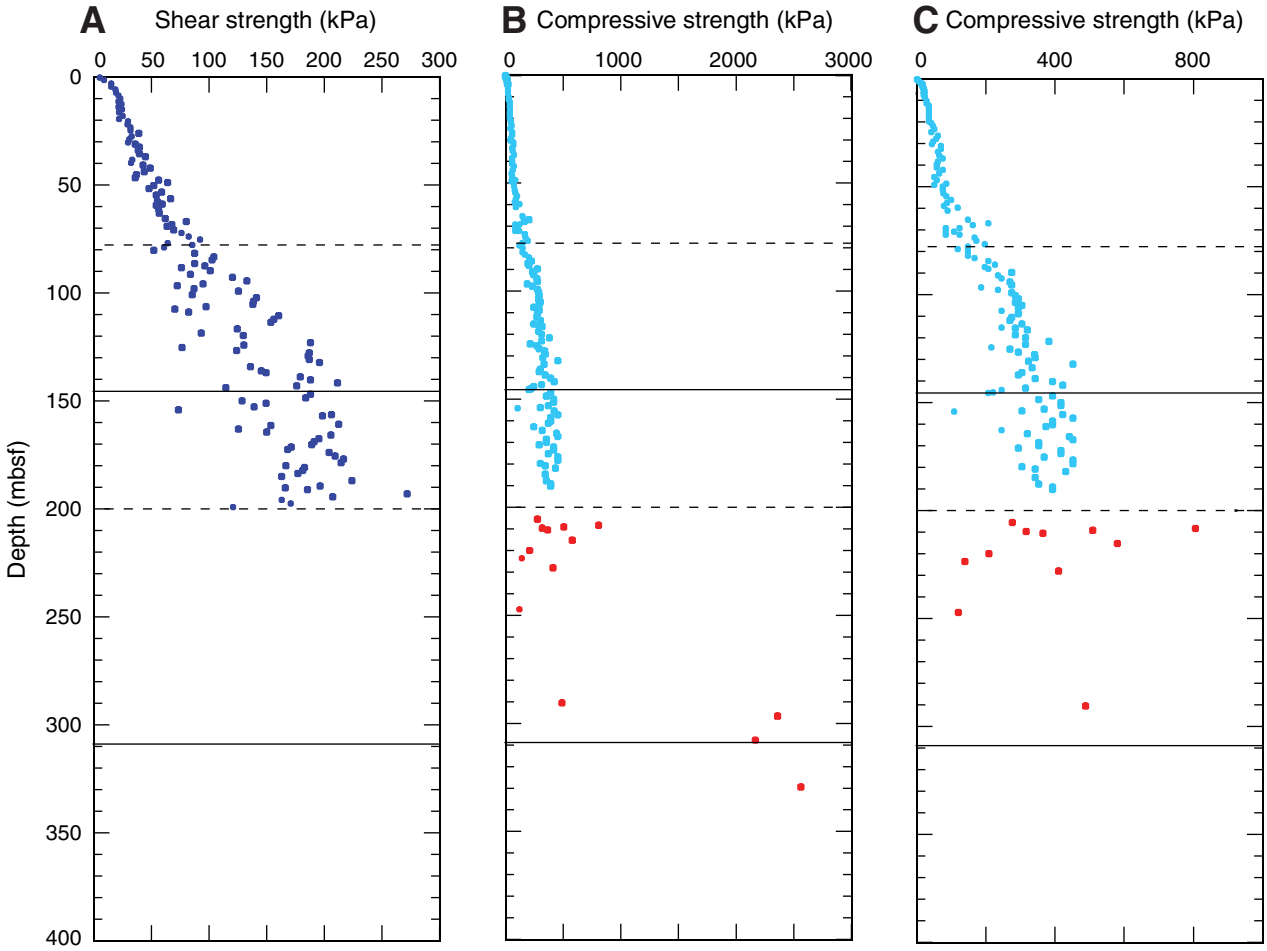

Figure F40. Reflectance L*, a*, and b* profiles, Site U1414. Solid lines = lithostratigraphic unit boundaries, dashed lines = subunit boundaries.

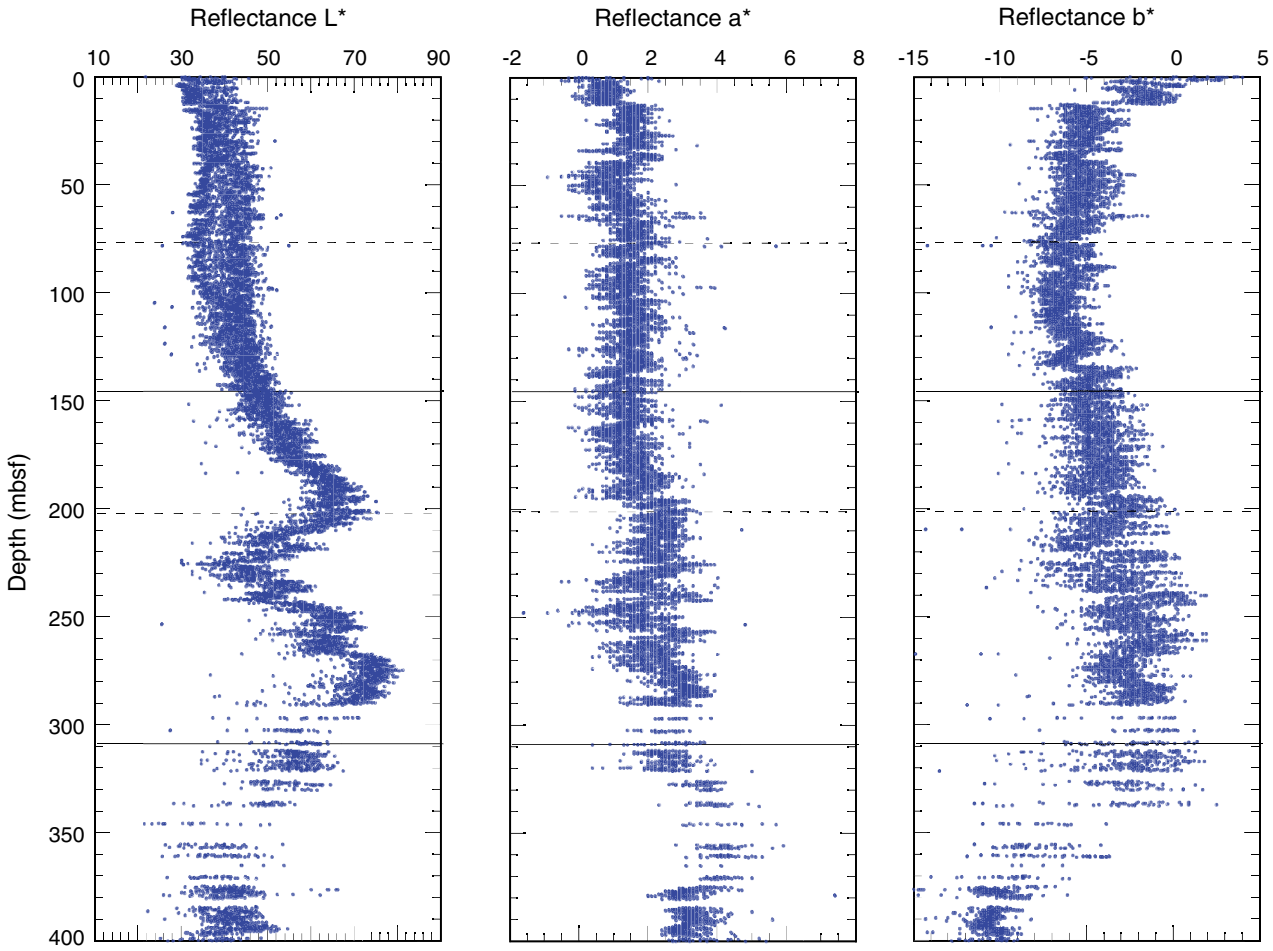

Figure F41. Formation factor values calculated from sediment electrical conductivity measurements, Site U1414. Solid line = lithostratigraphic unit boundary, dashed line = subunit boundary.

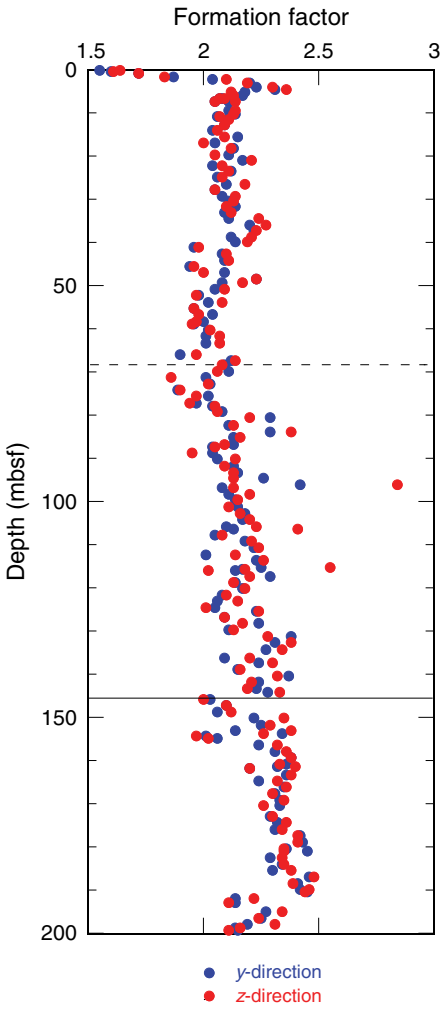

Figure F42. Basalt core magnetic susceptibility from the WRMSL, natural gamma radiation (NGR), and gamma ray attenuation (GRA) bulk density, Site U1414. Alternate depth scale CCSF-344-U1414 is used for the vertical axis.

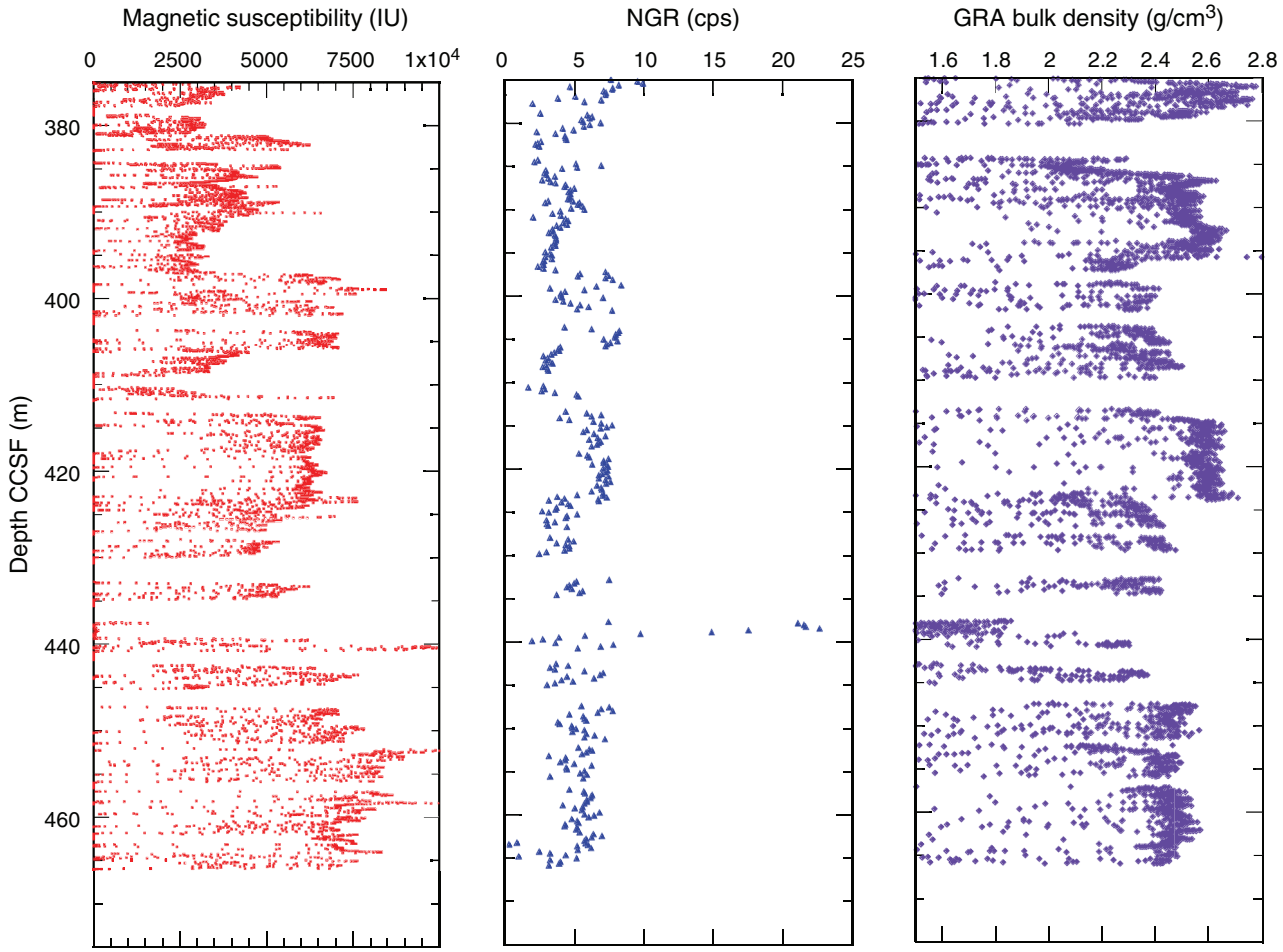

Figure F43. Reflectance L*, a*, and b* for igneous basement, Site U1414. Alternate depth scale CCSF used for the vertical axis.

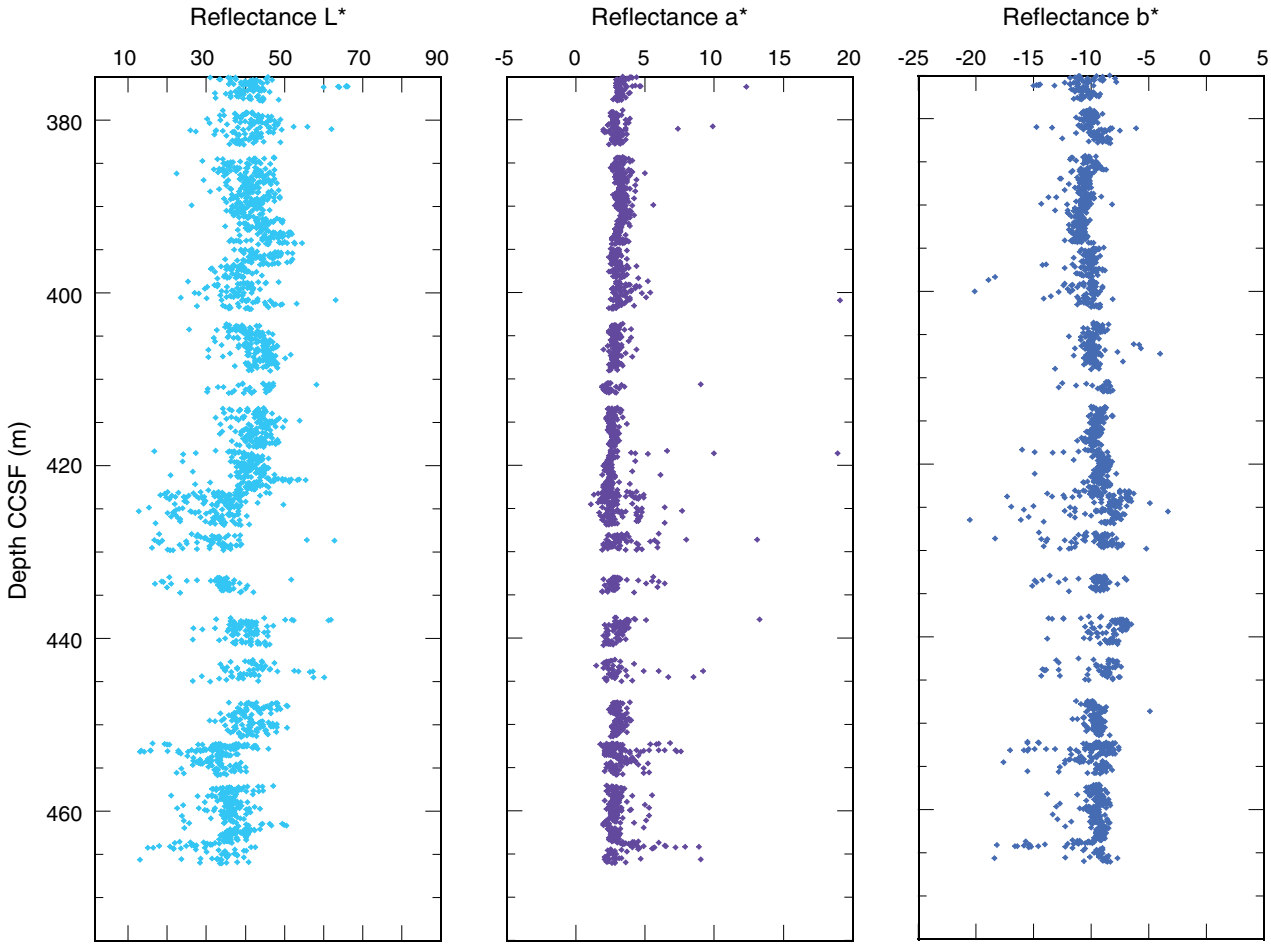

Figure F44. Paleomagnetic results, Hole U1414A. **A, B.** Archive-half NRM intensity and inclination after AF demagnetization at 0 and 40 mT. **C.** Discrete sample characteristic remanent magnetization (ChRM) determined by principal component analysis (Kirschvink, 1980). Black = normal polarity, white = reversed polarity.

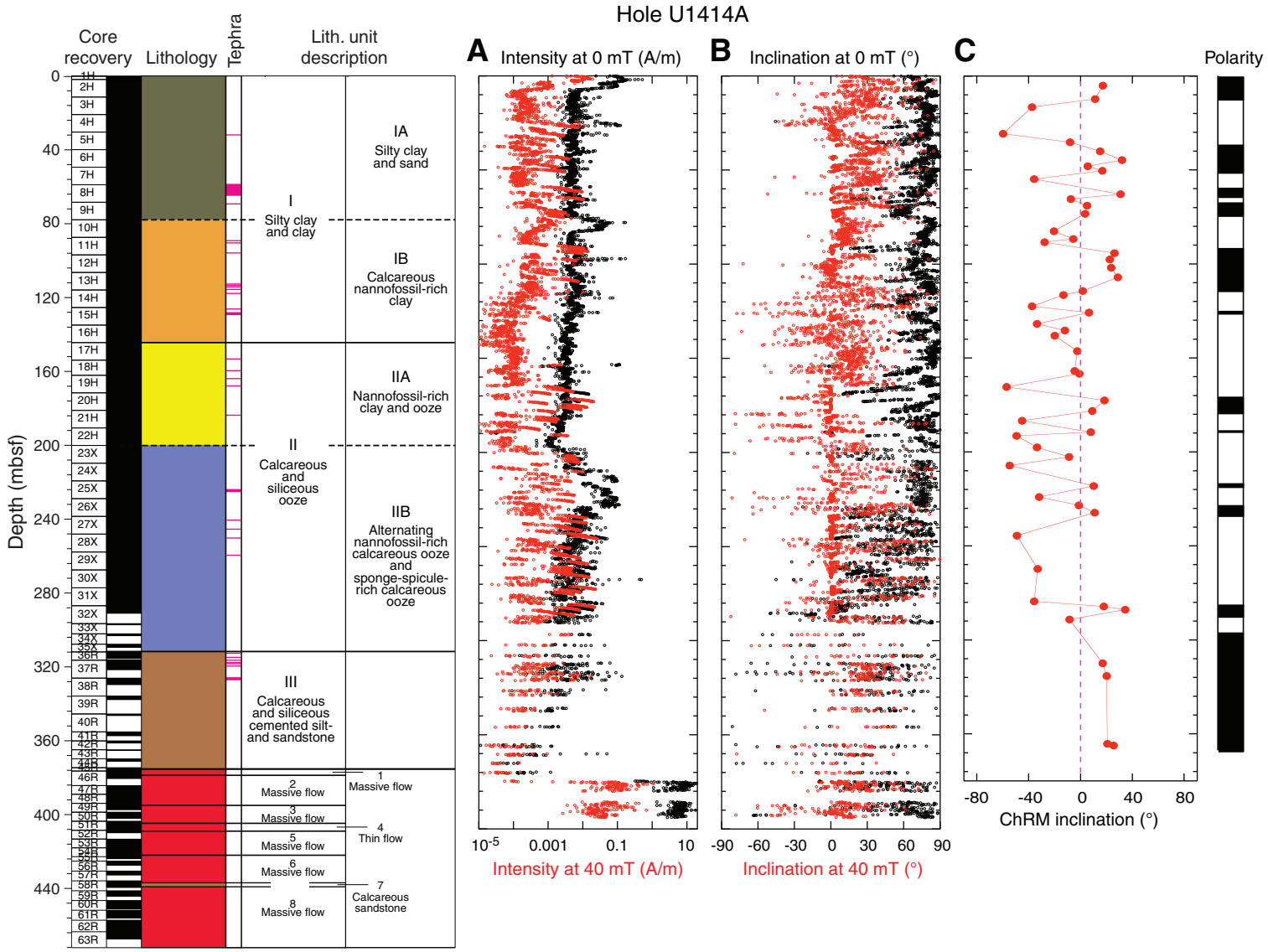

Figure F45. Representative vector endpoint diagrams (Zijderveld, 1967) for discrete sediment samples from stepwise AF demagnetization. All samples display a normal vertical component of magnetization caused by drilling that is removed after 5 mT demagnetization. Open and solid squares = projection of the magnetization vector end-points onto the vertical and horizontal planes, respectively. NRM = natural remanent magnetization. Blue lines = ChRM component derived by principal component analysis (Kirschvink, 1980).

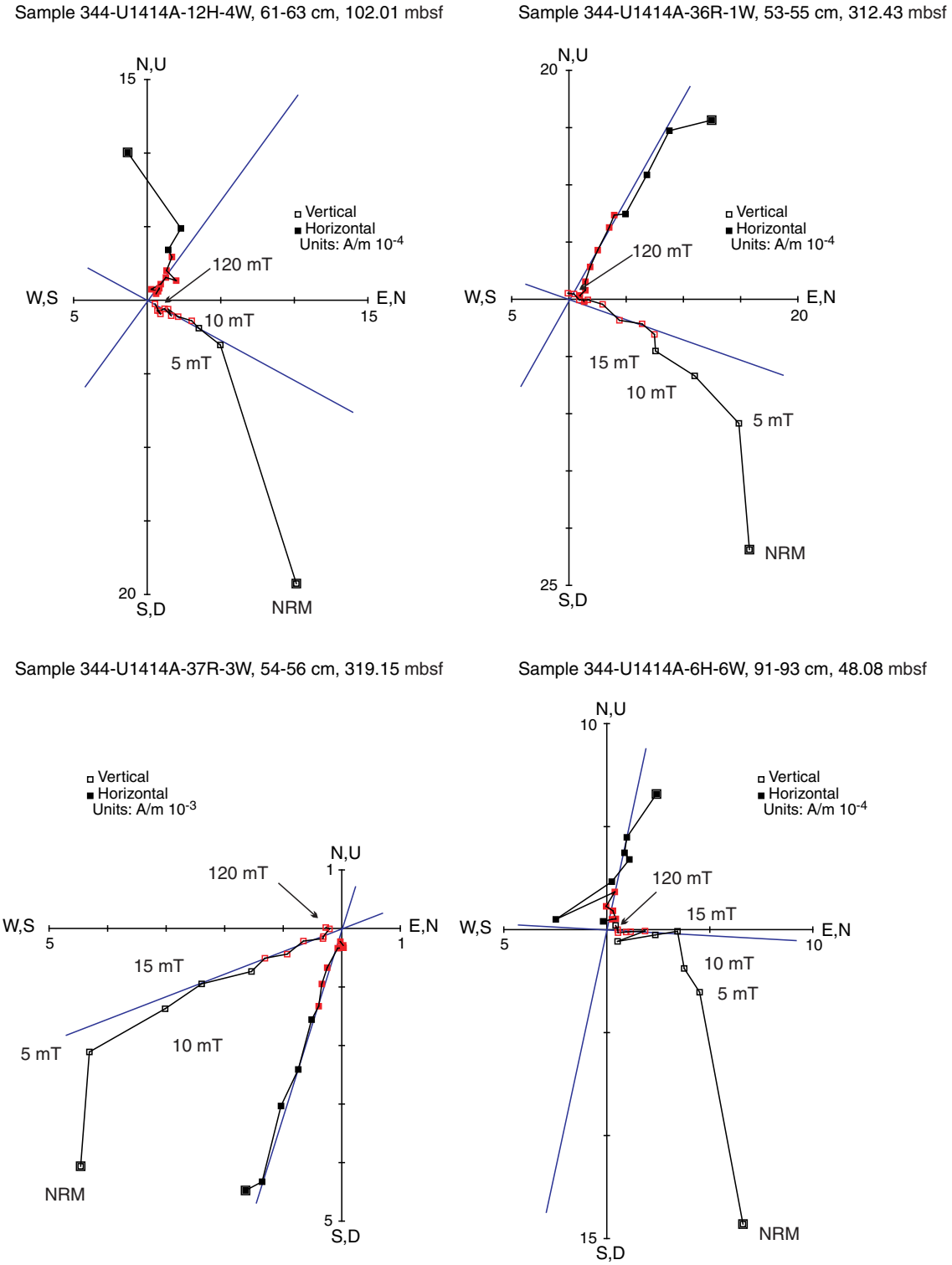

Figure F46. Caliper and total gamma ray logs, Hole U1414A. LCAL = hole diameter measured by the Hostile Environment Litho-Density Sonde (HLDS), C1 and C2 = hole diameters measured in orthogonal directions by the Formation MicroScanner (FMS), HSGR = total gamma ray curve measured by the Hostile Environment Natural Gamma Ray Sonde (HNGS) in the FMS-sonic and triple combo–UBI (TC) tool strings, p1 = logging pass 1, p2 = logging pass 2, p3 = logging pass 3. For more information on tool and curve descriptions, see the "Methods" chapter (Harris et al., 2013b).

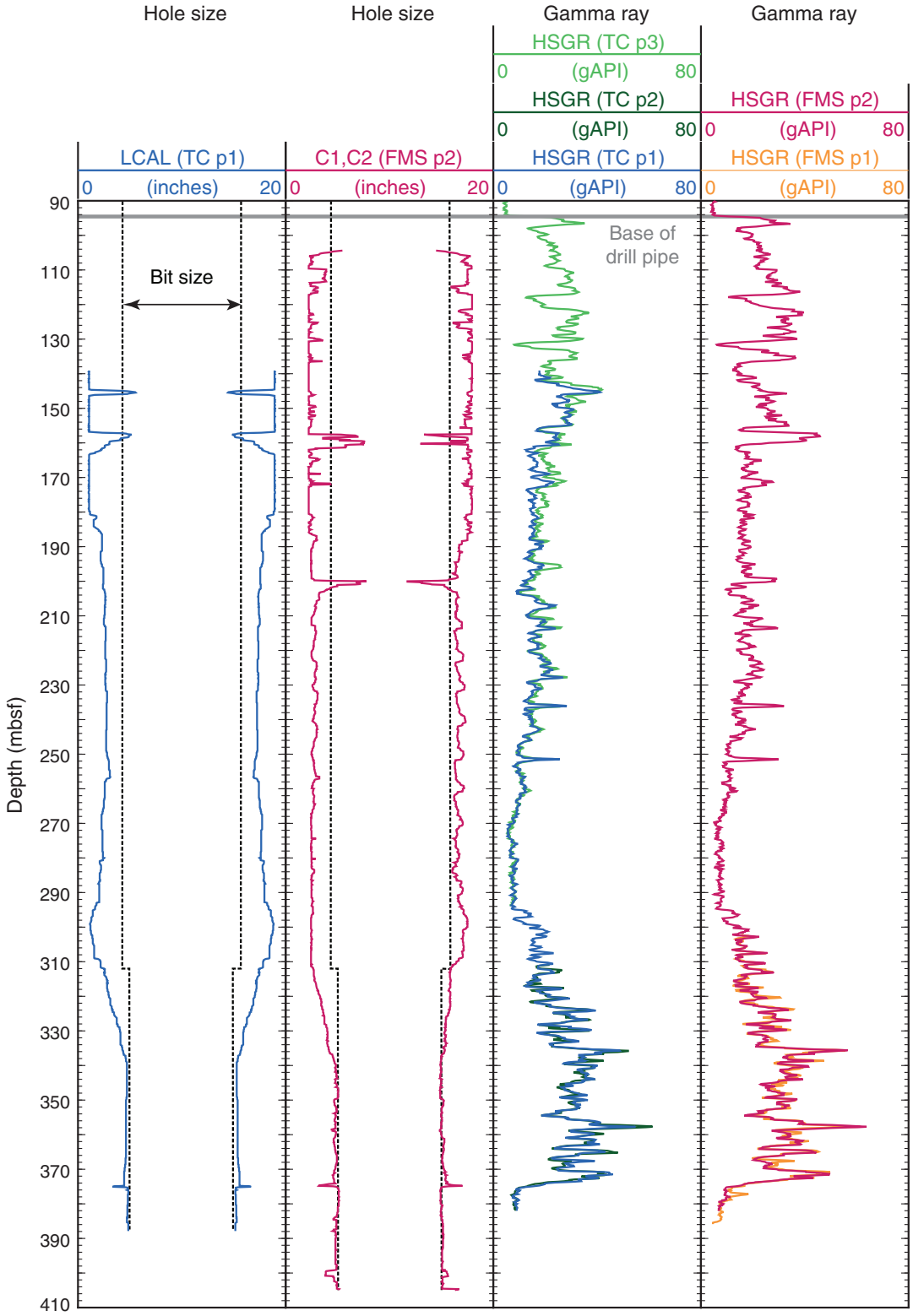

Figure F47. Spectral gamma ray logs, Hole U1414A. HSGR = total gamma ray curve measured by the HNGS in the Formation MicroScanner (FMS)-sonic and triple combo–UBI (TC) tool strings, HURA = uranium content, HTHO = thorium content, HFK = potassium content, p1 = logging pass 1, p2 = logging pass 2, p3 = logging pass 3. For more information on tool and curve descriptions, see the "Methods" chapter (Harris et al., 2013b).

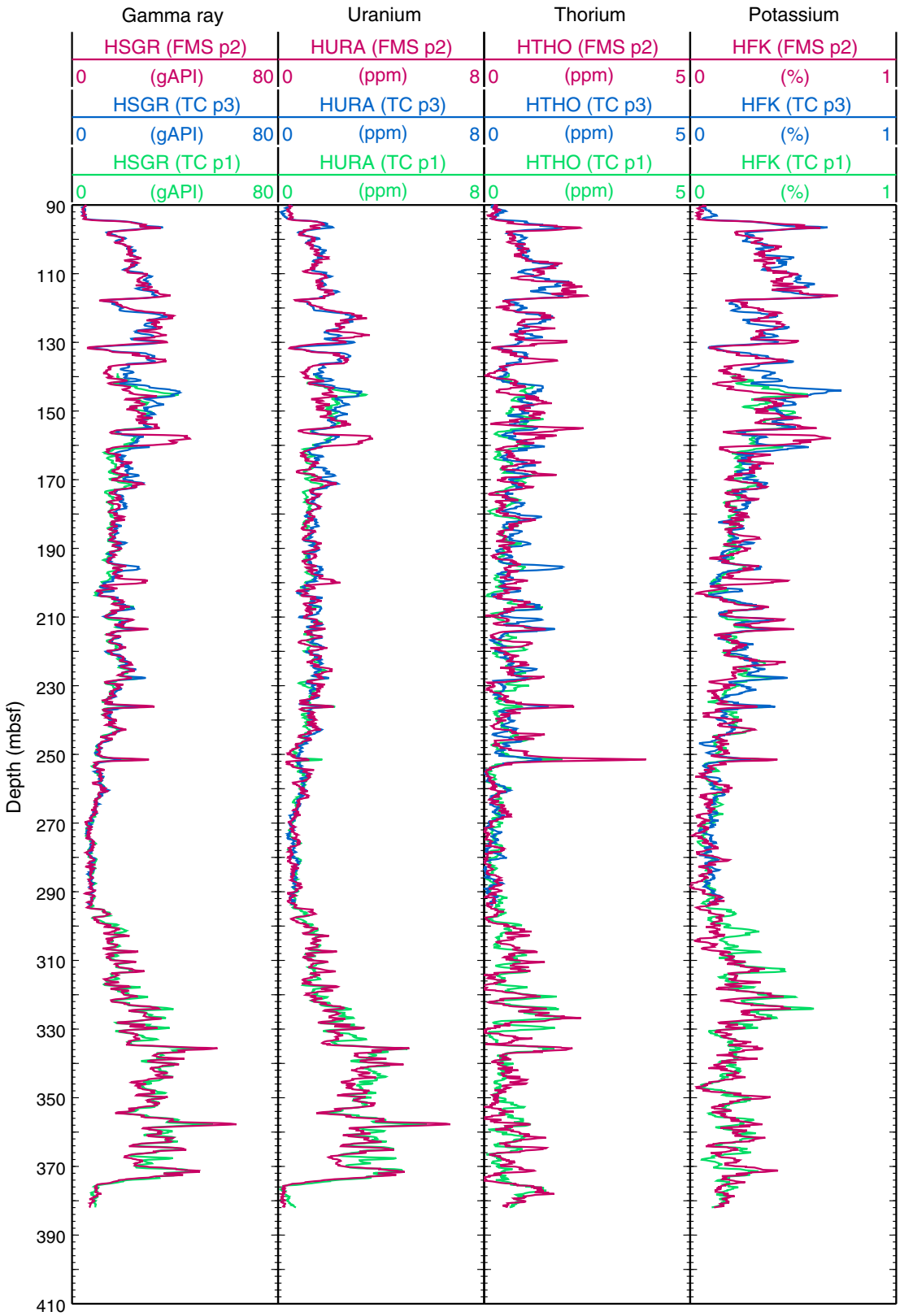

Figure F48. Summary of wireline log data, Hole U1414A. HSGR = total gamma ray curve measured by the HNGS in the Formation MicroScanner (FMS)-sonic and triple combo–UBI (TC) tool strings, NGR = natural gamma ray from core measurements, RHOM = bulk density from logs, MAD = bulk density from core measurements, RT HLRT = true formation resistivity, VCO = compressional wave velocity, VS1 = shear wave velocity. For more information on tool and curve descriptions, see the **"Methods"** chapter (Harris et al., 2013b).

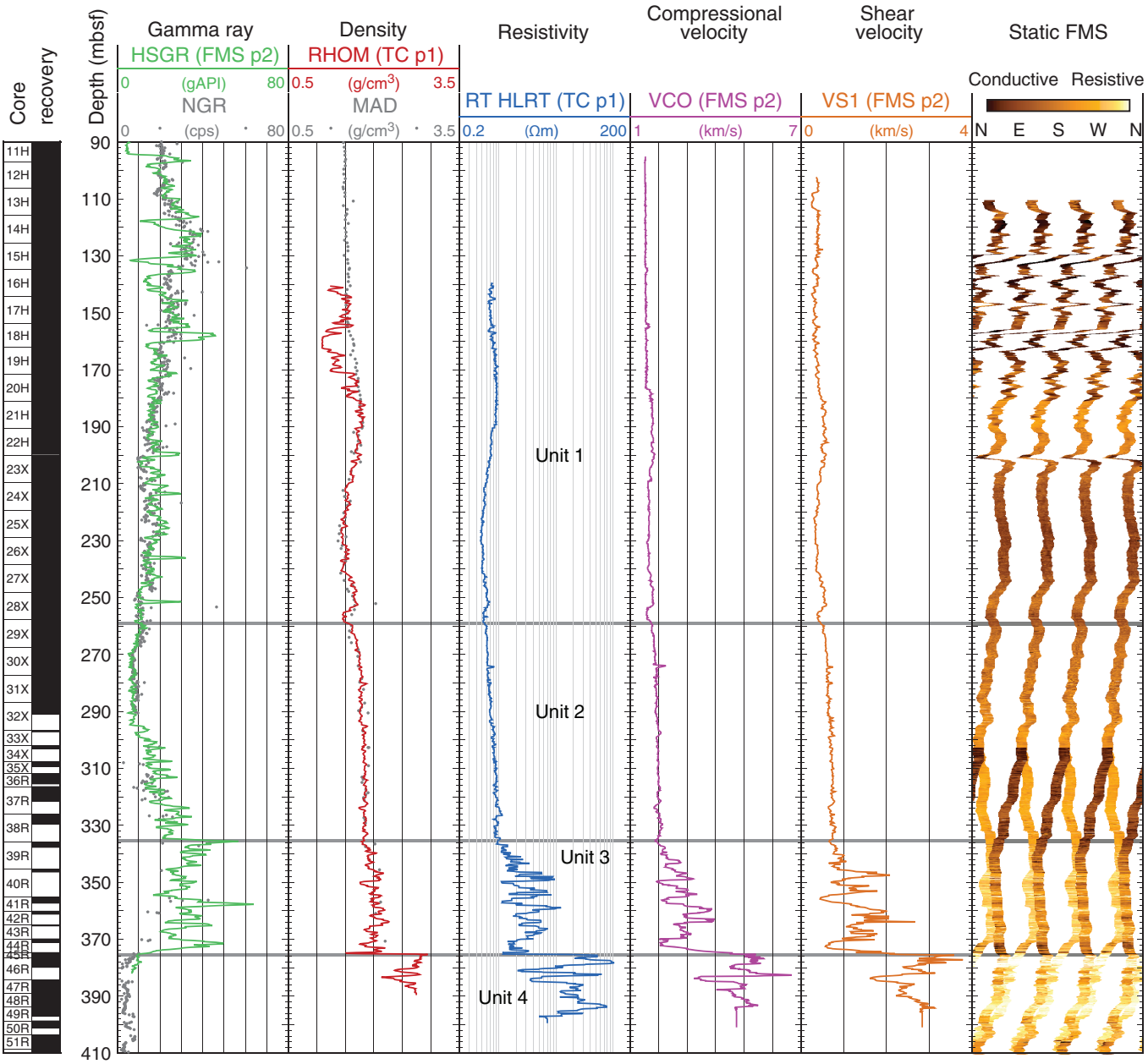

Figure F49. Downhole log images, Hole U1414A. FMS = Formation MicroScanner, UBI = Ultrasonic Borehole Imager. For more information on tools and borehole images, see the "Methods" chapter (Harris et al., 2013b).

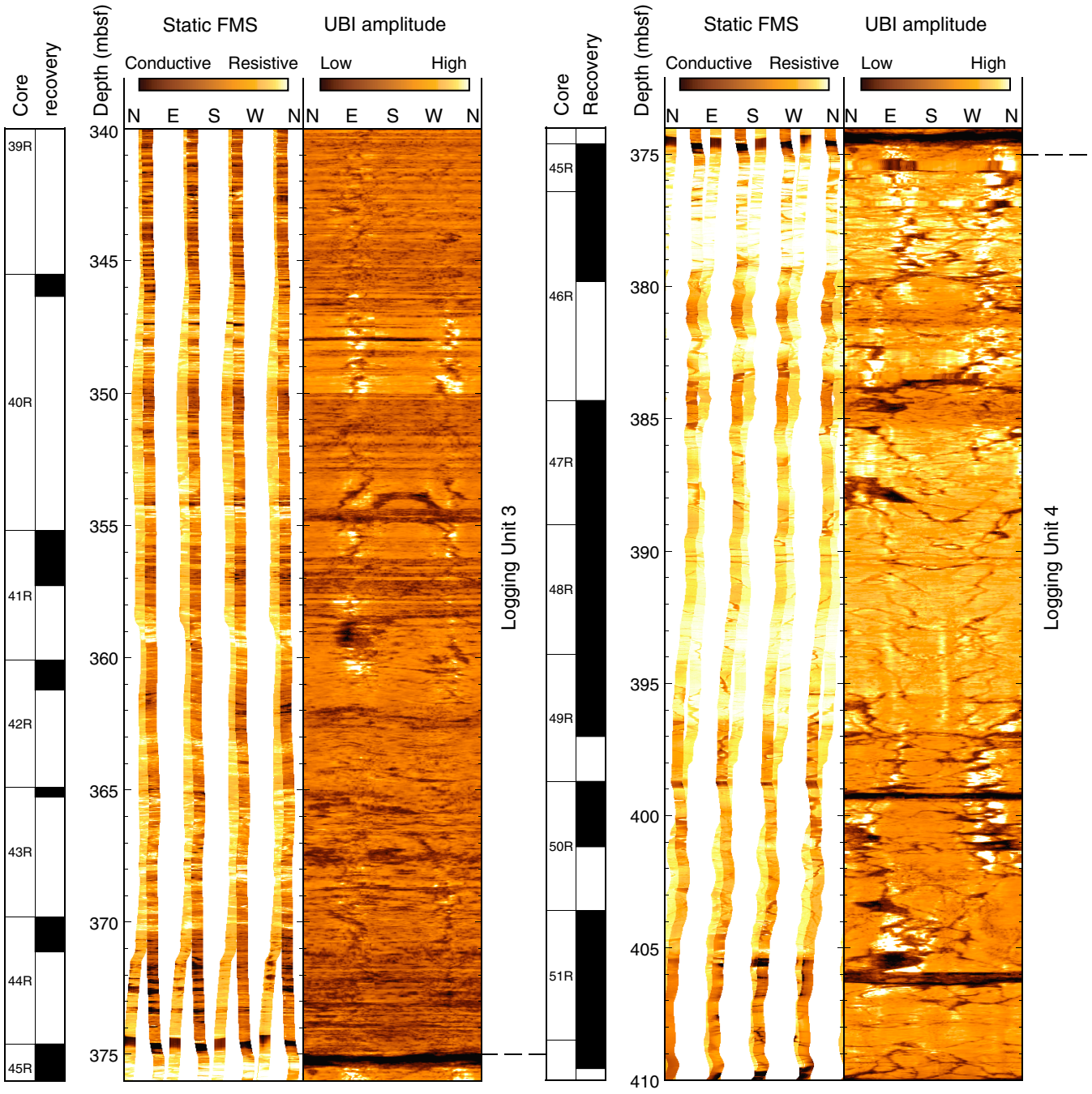

Table T1. Site U1414 coring summary. (Continued on next page.)

Hole U1414A
Latitude: 8°30.2304′N
Longitude: 84°13.5298′W
Time on hole (h): 191.0 (8.0 days)
Seafloor (drill pipe measurement from rig floor, m DRF): 2469.6
Distance between rig floor and sea level (m): 11.5
Water depth (drill pipe measurement from sea level, m): 2458.6
Total penetration (drilling depth below seafloor, m DSF): 471.6
Total length of cored section (m): 471.6
Total core recovered (m): 383.95
Core recovery (%): 81
Total number of cores: 63

Core	Date (2012)	Time UTC (h)	Depth DSF (m) Top of cored interval	Depth DSF (m) Bottom of cored interval	Interval advanced (m)	Depth CSF (m) Top of cored interval	Depth CSF (m) Bottom of cored interval	Length of core recovered (m)	Recovery (%)	Comments
344-U1414A-										
1H	3 Dec	1420	0.00	1.90	1.9	0.00	1.91	1.91	101	FlexIT
2H	3 Dec	1530	1.90	11.40	9.5	1.90	11.85	9.95	105	FlexIT
3H	3 Dec	1630	11.40	20.90	9.5	11.40	21.49	10.09	106	FlexIT, APCT-3
4H	3 Dec	1720	20.90	30.40	9.5	20.90	30.79	9.89	104	FlexIT
5H	3 Dec	1825	30.40	39.90	9.5	30.40	40.30	9.90	104	FlexIT, APCT-3
6H	3 Dec	1915	39.90	49.40	9.5	39.90	49.53	9.63	101	FlexIT
7H	3 Dec	2015	49.40	58.90	9.5	49.40	59.32	9.92	104	FlexIT, APCT-3
8H	3 Dec	2105	58.90	68.40	9.5	58.90	68.73	9.83	103	FlexIT
9H	3 Dec	2205	68.40	77.90	9.5	68.40	78.30	9.90	104	FlexIT, APCT-3
10H	3 Dec	2250	77.90	87.40	9.5	77.90	87.76	9.86	104	FlexIT
11H	3 Dec	2355	87.40	96.90	9.5	87.40	97.15	9.75	103	FlexIT
12H	4 Dec	0040	96.90	106.40	9.5	96.90	106.79	9.89	104	FlexIT
13H	4 Dec	0120	106.40	115.90	9.5	106.40	116.00	9.60	101	FlexIT
14H	4 Dec	0210	115.90	125.40	9.5	115.90	125.80	9.90	104	FlexIT
15H	4 Dec	0255	125.40	134.90	9.5	125.40	135.15	9.75	103	FlexIT
16H	4 Dec	0330	134.90	144.40	9.5	134.90	144.64	9.74	103	FlexIT
17H	4 Dec	0430	144.40	153.90	9.5	144.40	154.02	9.62	101	FlexIT
18H	4 Dec	0515	153.90	162.10	8.2	153.90	162.13	8.23	100	FlexIT
19H	4 Dec	0650	162.10	171.60	9.5	162.10	171.75	9.65	102	FlexIT
20H	4 Dec	0735	171.60	181.10	9.5	171.60	181.19	9.59	101	FlexIT
21H	4 Dec	0830	181.10	190.60	9.5	181.10	191.52	9.57	101	FlexIT
22H	4 Dec	1005	190.60	200.10	9.5	190.60	199.74	9.14	96	FlexIT
23X	4 Dec	1210	200.10	209.70	9.6	200.10	209.58	9.48	99	
24X	4 Dec	1310	209.70	219.30	9.6	209.70	219.49	9.79	102	
25X	4 Dec	1400	219.30	228.90	9.6	219.30	229.01	9.71	101	
26X	4 Dec	1455	228.90	238.50	9.6	228.90	238.57	9.67	101	
27X	4 Dec	1545	238.50	248.10	9.6	238.50	248.27	9.77	102	
28X	4 Dec	1640	248.10	257.80	9.7	248.10	257.45	9.35	96	
29X	4 Dec	1730	257.80	267.50	9.7	257.80	267.46	9.66	100	
30X	4 Dec	1825	267.50	277.20	9.7	267.50	277.17	9.67	100	
31X	4 Dec	1925	277.20	286.90	9.7	277.20	286.82	9.62	99	
32X	4 Dec	2025	286.90	296.60	9.7	286.90	290.97	4.07	42	
33X	4 Dec	2150	296.60	302.10	5.5	296.60	297.23	0.63	11	
34X	5 Dec	0025	302.10	307.70	5.6	302.10	303.11	1.01	18	
35X	5 Dec	0230	307.70	311.90	4.2	307.70	309.37	1.67	40	
36R	6 Dec	0230	311.90	316.40	4.5	311.90	315.45	3.55	79	
37R	6 Dec	0355	316.40	326.10	9.7	316.40	321.53	5.13	53	
38R	6 Dec	0525	326.10	335.80	9.7	326.10	329.59	3.49	36	
39R	6 Dec	0725	335.80	345.50	9.7	335.80	337.71	1.91	20	
40R	6 Dec	0930	345.50	355.20	9.7	345.50	346.35	0.85	9	
41R	6 Dec	1110	355.20	360.10	4.9	355.20	357.28	2.08	42	
42R	6 Dec	1235	360.10	364.90	4.8	360.10	361.23	1.13	24	
43R	6 Dec	1355	364.90	369.80	4.9	364.90	365.28	0.38	8	
44R	6 Dec	1505	369.80	374.60	4.8	369.80	371.13	1.33	28	
45R	6 Dec	1915	374.60	376.40	1.8	374.60	377.80	2.85	158	
46R	7 Dec	0310	376.40	384.30	7.9	376.40	380.43	3.40	43	
47R	7 Dec	0640	384.30	389.00	4.7	384.30	389.38	4.93	105	
48R	7 Dec	0915	389.00	393.90	4.9	389.00	394.46	5.19	106	
49R	7 Dec	1320	393.90	398.70	4.8	393.90	397.34	3.11	65	
50R	7 Dec	1820	398.70	403.60	4.9	398.70	401.91	2.48	51	
51R	7 Dec	2330	403.60	408.50	4.9	403.60	409.08	5.10	104	
52R	8 Dec	0130	408.50	413.30	4.8	408.50	409.81	1.06	22	

Table T1 (continued).

Core	Date (2012)	Time UTC (h)	Depth DSF (m) Top of cored interval	Depth DSF (m) Bottom of cored interval	Interval advanced (m)	Depth CSF (m) Top of cored interval	Depth CSF (m) Bottom of cored interval	Length of core recovered (m)	Recovery (%)	Comments
53R	8 Dec	0435	413.30	418.20	4.9	413.30	417.89	4.28	87	
54R	8 Dec	1110	418.20	423.00	4.8	418.20	423.87	5.55	116	
55R	8 Dec	1535	423.00	427.90	4.9	423.00	426.92	3.27	67	
56R	8 Dec	2025	427.90	432.80	4.9	427.90	429.91	1.88	38	
57R	8 Dec	2255	432.80	437.60	4.8	432.80	434.73	1.77	37	
58R	9 Dec	0130	437.60	442.50	4.9	437.60	440.86	2.64	54	
59R	9 Dec	0515	442.50	447.30	4.8	442.50	445.21	2.04	43	
60R	9 Dec	0810	447.30	452.10	4.8	447.30	451.42	3.50	73	
61R	9 Dec	1055	452.10	457.00	4.9	452.10	455.35	3.25	66	
62R	9 Dec	1315	457.00	461.90	4.9	457.00	461.84	4.42	90	
63R	9 Dec	1805	461.90	471.60	9.7	461.90	466.24	3.97	41	
			Hole U1414A totals:		471.6			383.95	81	

DRF = drilling depth below rig floor, DSF = drilling depth below seafloor, CSF = core depth below seafloor. H = advanced piston corer core, X = extended core barrel core, R = rotary core barrel core. APCT-3 = advanced piston corer temperature tool.

Table T2. Summary of sediment and basement units, Site U1414.

Unit	Subunit	Site U1381*	Top depth (mbsf)	Core, section, interval (cm)	Bottom depth (mbsf)	Core, section, interval (cm)	Unit thickness (m)	Major lithology
Sediment								
				344-U1414A-		344-U1414A-		
I	IA	I	0.00	1H-1, 0	78.3	9H-CC, 30	78.3	Silty clay and sand
	IB		78.3	10H-1, 0	145.34	17H-1, 94	67.04	Calcareous nannofossil–rich clay
II	IIA		145.34	17H-1, 94	200.01	22X-CC, 30	54.67	Nannofossil-rich calcareous ooze
	IIB	II	200.01	23X-1, 0	309.37	35X-CC, 29	109.36	Alternating nannofossil-rich calcareous ooze and sponge spicule–rich calcareous ooze
III		IV (III)	309.37	35X-CC, 29	375.25	45R-1, 65	65.88	Calcareous and siliceous cemented silt- and sandstone
Basement								
				344-U1414A-		344-U1414A-		
1			375.25	45R-1, 65	378.78	46R-2, 125	3.49	Massive flow
2			378.78	46R-2, 125	395.94	49R-2, 54	16.9	Massive flow
3			395.94	49R-2, 54	405.90	51R-2, 114	9.69	Massive flow
4			405.90	51R-2, 114	409.41	52R-1, 91	3.51	Thin flow
5			409.41	52R-1, 91	423.87	54R-5, 83	14.46	Massive flow
6			423.87	55R-1, 0	437.70	58R-1, 10	13.83	Massive flow
7			437.70	58R-1, 10	439.37	58R-2, 33	1.67	Intercalated calcareous silty sandstone
8			439.37	58R-2, 33	466.24	63R-4, 29	26.87	Massive flow

* = Site U1381 equivalent units. See text for detail.

Table T3. Range of groundmass compositions observed in thin section within each igneous unit, Site U1414.

Basement unit	Plagioclase (vol%)	Clinopyroxene (vol%)	Olivine (vol%)	Fe-Ti oxides (vol%)	Cryptocrystalline (vol%)	*N*
1	63	21.5	3	5.5	7	1
2	57.8	31.6	8.6	8.9	23.3	3
	48.3	17.2	1	4.7	8	
3	48	18.7	0.3	6.5	36.2	2
	44	9	0	5.6	31	
4	27.8	10.3	0	13.7	47.8	1
5	62.6	18.7	3.3	6.8	13.1	2
	61.2	17.1	0.5	4.3	12.3	
6	44	15.7	0	5.1	34.8	1
7	58.5	22.8	3.1	5.7	24.8	4
	52.2	14	0	4.2	12.8	

N = number of thin sections on which the composition range is based.

Table T4. Summary of alteration features observed in basement, Hole U1414A.

	Total	Saponite	Carbonate	Pyrite	Smectite	Quartz	Zeolite
Veins per meter:	19.99	7.95	3.05	4.04	10.87	1.82	0.12
Abundance of vein-filling minerals (vol%):	3.47	1.65	0.39	0.13	0.91	0.46	0.002
Abundance of secondary minerals in breccia (vol%):	0.28			0.004	0.28		
Abundance of vesicle-filling secondary minerals (vol%):	2.32	0.71	0.001	0.05	1.512	0.044	0.0004
Abundance of secondary minerals occupying veins and breccia (vol%):	3.75	1.65	0.39	0.13	1.19	0.46	0.002
Total secondary mineral abundance (veins, breccia, and vesicles) (vol%):	6.07	2.35	0.39	0.18	2.7	0.5	0.003

Veins per meter was normalized to 100% recovery. Volume percent was calculated based on the surface area that each alteration feature occupied on the cut surface of recovered core. Raw data sourced from visual observations (**web.iodp.tamu.edu/UWQ/**).

Table T5. Calcareous nannofossil faunal distribution, Hole U1414A. (Continued on next page.)

Core, section, interval (cm)	Depth (mbsf) Top	Depth (mbsf) Bottom	Preservation	Group abundance	*Calcidiscus leptoporus*	*Calcidiscus tropicus*	Calcispheres	*Catinaster coalitus*	*Ceratolithus armatus (acutus)*	*Ceratolithus atlanticus*	*Ceratolithus cristatus*	*Ceratolithus cristatus (rugosus)*	*Coccolithus miopelagicus*	*Coccolithus pelagicus*	*Cyclicargolithus floridanus*	*Discoaster asymmetricus*	*Discoaster bellus*	*Discoaster brouweri*	*Discoaster kugleri*	*Discoaster pentaradiatus*	*Discoaster quinqueramus*	*Discoaster* sp.	*Discoaster* spp.	*Discoaster surculus*	*Discoaster triradiatus*	*Discoaster variabilis*	*Emiliania huxleyi*	*Gephyrocapsa* (<4 µm)	*Gephyrocapsa* (>4 µm)	*Gephyrocapsa* (>5.5 µm)	*Gephyrocapsa caribbeanica*	*Gephyrocapsa oceanica*	*Helicosphaera carteri*	*Helicosphaera sellii*	*Helicosphaera* sp.	*Helicosphaera* spp.	*Pontosphaera discopora*	*Pontosphaera japonica*	*Pontosphaera multipora*
344-U1414A-																																						
1H-CC, 0–5	1.84	1.89	M	C	Freq									R												Freq	C	C		C	C				C			
2H-CC, 0–5	11.77	11.82	G	C	Freq						R	R															C	A	R	A	A				C			
3H-CC, 0–5	21.40	21.45	M	R	Freq																						C	R		Freq	C				Freq			
4H-CC, 0–5	30.70	30.75	M	F	Freq									R													C	Freq		Freq	C				Freq			
5H-CC, 0–5	40.25	40.30	M	C	Freq		Freq							Freq													C	C		C	C				Freq			
6H-CC, 0–5	49.47	49.52	G	A	Freq		Freq																			Freq	A	A		A	A				C			
7H-CC, 0–5	59.27	59.32	G	A	C									Freq													D	A		C	A				Freq			
8H-CC, 0–5	68.68	68.73	G	A	C		R							R												C	A	A		A	A				C			
9H-CC, 0–5	78.25	78.30	M	R	R																						Freq					Freq	R			Freq			
10H-CC, 0–5	87.71	87.76	G	A	Freq																		*				D	Freq		A	A	Freq			C			
11H-CC, 0–5	97.10	97.15	G	F	R									Freq													C				C				Freq			
12H-CC, 0–5	106.73	106.78	M	C	Freq									R													C			Freq	C	R			C			
13H-7, 0–5	115.95	116.00	G	C	R																						C	C		Freq	C				C		R	
14H-CC, 0–5	125.75	125.80	G	F	C									R				R					R									R			C	R		
15H-CC, 0–5	135.09	135.14	G	A	C						R	R		Freq				C					C												C			R
16H-CC, 0–5	144.59	144.64	G	A	Freq						R	R		Freq				C					C												Freq			
17H-CC, 0–5	153.95	154.00	M	A	C													C					C													Freq		
18H-CC, 0–5	162.08	162.13	M	A	Freq									Freq		R		C					C		R							R						
19H-CC, 0–5	171.68	171.73	G	D	C						R	R		Freq						Freq			C									Freq	Freq					
20H-CC, 0–5	181.05	181.10	M	D	C						R	R		Freq				C		C			A											R				
21H-CC, 0–5	191.40	191.45	G	D	Freq		Freq		R					Freq						Freq			C	C										R				
22H-CC, 0–5	199.65	199.70	G	D	Freq									Freq				C		Freq	R		C											R				
23X-CC, 0–5	209.48	209.53	G	A	R									C			Freq	Freq		Freq			A			Freq						R						
24X-CC, 0–5	219.34	219.39	M	C										Freq		R		C					C			R						R						
25X-CC, 0–5	228.92	228.97	M	A	R									R				C		C			C			Freq						R						
26X-CC, 0–5	238.46	238.51	M	C	Freq									C									C			Freq						R			R			
27X-CC, 0–5	248.15	248.20	M	C	C									C				C					C															
28X-CC, 0–5	257.28	257.33	G	C	Freq		C					R	C	C									R															
29X-CC, 0–5	267.34	267.39	M	C			C					Freq	C	C									Freq															
30X-CC, 0–5	277.12	277.17	M	C								R	C	C									Freq									Freq						
31X-CC, 0–5	286.77	286.82	M	C					R					C								Freq															
32X-CC, 0–5	290.92	290.97	M	C					R			R	C	C																		R						
33X-CC, 0–5	297.18	297.23	P	C										C								R															
34X-CC, 0–5	303.06	303.11	M	C								Freq	C	C								R										R						
35X-CC, 0–5	309.31	309.36	M	C								R	C	C									Freq															
36R-CC, 0–5	315.36	315.41	M	C								Freq			C				R																			
37R-CC, 0–5	321.48	321.53	M	A	R	R								C	Freq								R												R			
38R-CC, 0–5	329.54	329.59	P	F										C									R														
39R-CC, 0–5	337.49	337.54	P	F										Freq									Freq															

Preservation: G = good, M = moderate, P = poor. Abundance: D = dominant, A = abundant, C = common, R= rare, Freq = frequent, F = few. * = reworked.

Table T5 (continued).

Core, section, interval (cm)	Depth (mbsf) Top	Depth (mbsf) Bottom	Preservation	Group abundance	*Pseudoemiliania lacunosa*	*Reticulofenestra minuta*	*Reticulofenestra pseudoumbilicus*	*Reticulofenestra* small	*Rhabdosphaera clavigera*	*Scyphosphaera pulcherrima*	*Sphenolithus abies*	*Sphenolithus* spp.	*Syracosphaera pulchra*	*Umbilicosphaera sibogae*
344-U1414A-														
1H-CC, 0–5	1.84	1.89	M	C										
2H-CC, 0–5	11.77	11.82	G	C										R
3H-CC, 0–5	21.40	21.45	M	R										R
4H-CC, 0–5	30.70	30.75	M	F										R
5H-CC, 0–5	40.25	40.30	M	C										R
6H-CC, 0–5	49.47	49.52	G	A										
7H-CC, 0–5	59.27	59.32	G	A							*		R	R
8H-CC, 0–5	68.68	68.73	G	A										
9H-CC, 0–5	78.25	78.30	M	R										R
10H-CC, 0–5	87.71	87.76	G	A								*		
11H-CC, 0–5	97.10	97.15	G	F	Freq									
12H-CC, 0–5	106.73	106.78	M	C	Freq									
13H-7, 0–5	115.95	116.00	G	C	Freq									R
14H-CC, 0–5	125.75	125.80	G	F	C									
15H-CC, 0–5	135.09	135.14	G	A	C					R		C		
16H-CC, 0–5	144.59	144.64	G	A							R			
17H-CC, 0–5	153.95	154.00	M	A					R				R	
18H-CC, 0–5	162.08	162.13	M	A	C		D		R					
19H-CC, 0–5	171.68	171.73	G	D	Freq	C	C				Freq	C		
20H-CC, 0–5	181.05	181.10	M	D			C				C	C		
21H-CC, 0–5	191.40	191.45	G	D			C			R	A	A		
22H-CC, 0–5	199.65	199.70	G	D			Freq				C	A		
23X-CC, 0–5	209.48	209.53	G	A			R				C	A		
24X-CC, 0–5	219.34	219.39	M	C			D				Freq	C		
25X-CC, 0–5	228.92	228.97	M	A			C				Freq	C		
26X-CC, 0–5	238.46	238.51	M	C			C				R	Freq		
27X-CC, 0–5	248.15	248.20	M	C			C							
28X-CC, 0–5	257.28	257.33	G	C			C					C		
29X-CC, 0–5	267.34	267.39	M	C			A					C		
30X-CC, 0–5	277.12	277.17	M	C			A					C		
31X-CC, 0–5	286.77	286.82	M	C			C					C		
32X-CC, 0–5	290.92	290.97	M	C			C					Freq		
33X-CC, 0–5	297.18	297.23	P	C			C					C		
34X-CC, 0–5	303.06	303.11	M	C			C					C		
35X-CC, 0–5	309.31	309.36	M	C			C					C		
36R-CC, 0–5	315.36	315.41	M	C			C					C		
37R-CC, 0–5	321.48	321.53	M	A			C					C		
38R-CC, 0–5	329.54	329.59	P	F			C	Freq				C		
39R-CC, 0–5	337.49	337.54	P	F			C	C				C		

Table T6. Radiolarian faunal distribution, Hole U1414A. (Continued on next page.)

Core, section, interval (cm)	Depth (mbsf) Top	Depth (mbsf) Bottom	Preservation	Group abundance	*Acrosphaera* sp.	*Acrosphaera murrayana*	*Acrosphaera spinosa*	*Acrosphaera trepanata*	*Actinomma medianum*	*Actinomma* sp.	*Amphirhopalum ypsilon*	*Anthocyrtidium marieae*	*Axoprunum* sp. ?	*Botryostrobus auritus*	*Carpocanistrum acutidentatum*	*Carpocanistrum cephallum*	*Carpocanistrum favosum*	*Carpocanistrum* sp.	*Carposphaera* sp.	*Cenosphaera* sp.	*Collonosphaera huxleyi*	*Collosphaera brattstroemi*	*Collosphaera macropora*	*Collosphaera orthoconus*	*Collosphaera tuberosa*	*Cornutella profunda*	*Corocalyptra cervus*	*Corocalyotra* sp.	*Cycladophora davisiana*	*Cyrtocapsella japonica*	*Diartus hughesi*	*Diartus petterssoni*	*Dictyocoryne truncatum*	*Dictyophimus crisiae*	*Didymocyrtis laticonus*	*Didymocyrtis penultima*	*Didymocyrtis tetrathalamus*	*Disolenia* sp.	*Dyctyocoryne profunda*	*Euchitonia* sp.	*Eucyrtidium acuminatum*	*Eucyrtidium hexagonatum*	*Giraffospyris angulata*	*Giraffospyris* sp.	*Haeckeliella* sp.	*Hexacontium laevigatum*	*Hexacontium* sp.	*Hexaloncha amphisiphon*	*Hexapyle dodecantha* group
344-U1414A-																																																
1H-CC, 0–5	1.84	1.89	VG	A				C			C	C		A	C		C		C		C	F		C	F			C					C			A		C		C	C	C	F		C	C	C
4H-CC, 0–5	30.70	30.75	VG	A				C			A			A	C		C		C		C	F		C				C					C			A		C		C	C	C	F	C	C	C	C
5H-CC, 0–5	40.25	40.30	VG	A											C		C		C			F		C	F			C					C					C		C	C	C				C	C
6H-CC, 0–5	49.47	49.52	VG	A											C		C		C			F		C	F			C					C					C		C	C	C				C	C
8H-CC, 0–5	68.68	68.73	G	A		C	C			C	C		C		F	F	C		C		C	F					F								A		C		C	F	C					C
11H-CC, 0–5	97.10	97.15	G	C		C	C				C				F	F	C		C									F										C			C						
10H-CC, 0–5	87.71	87.76	G	C		C	C				F			C		F			C										C			C					C			C	F	C					C
12H-CC, 0–5	106.73	106.78	G	C			F			C	F			C		F		F											C			F				F		C			F						C
14H-CC, 0–5	125.75	125.80	P	F			F			F								F																			F				F		C				F
16H-CC, 0–5	144.59	144.64	P	F		C	F			C				C			C			C			C							F				F	F	F					F					F
17H-CC, 0–5	153.95	154.00	G	C			F			C								C																		F						F					F
24X-CC, 0–5	219.34	219.39	VG	A	C					C							C	C													C	C							C		A		C				
25X-CC, 0–5	228.92	228.97	VG	A	C					C							C														C	C			C				C		A						
26X-CC, 0–5	238.46	238.51	VG	A	C					C							C														C	C							C		A						
29X-CC, 0–5	267.34	267.39	VG	A	C					C							C		C											F		C			C					C		A						

Preservation: VG = very good, G = good, P = poor. Abundance: A = abundant, C = common, F = few.

Table T6 (continued).

Core, section, interval (cm)	Depth (mbsf) Top	Depth (mbsf) Bottom	Preservation	Group abundance	*Hymeniastrum euclidis*	*Lamprocyclas maritalis maritalis*	*Lamprocyclas maritalis polypora*	*Larcospira quadrangula*	*Lipmanella dictyoceras*	*Lithopera bacca*	*Lithopera neotera*	*Lithostrobus hexagonalis*	*Lophophaenoma witjazzi*	*Lophospyris pentagona pentagona?*	*Lychnodictyum audax*	*Nephrospyris renilla*	*Octopyle stenozona*	*Otosphaera auriculata*	*Otosphaera polymorpha*	*Perichlamydium praetextum*	*Peripyramis circumtexta*	*Phormospyris stabilis*	*Phormostichoartus corbula*	*Porodiscus* sp.	*Pterocanium korotnevi*	*Pterocanium prismatium*	*Pterocanium* sp.	*Pterocanium trilobum*	*Pterocorys campanula*	*Pterocorys minythorax ?*	*Pterocorys* sp.	*Pterocorys zancleus*	*Pteroscenium pinnatum*	*Solenosphaera omnitubus omnitubus*	*Siphonosphaera tenera*	*Spongaster tetras*	*Spongocore puella*	*Spongocore* sp.	*Spongodiscus resurgens*	*Spongodiscus* sp.	*Spongosphaera* sp.	*Spongurus cylindricus*	*Spongurus* sp.	*Stichocorys delmontensis*	*Stichocorys peregrina*	*Stylatractus* sp.	*Stylodictya tenuispina*	*Stylodictya validispina*	*Tetrapyle octacantha*	*Tholospyris baconiana*	*Tholospyris* sp. group	*Zygocircus* sp.
344-U1414A-																																																		
1H-CC, 0–5	1.84	1.89	VG	A	C	C			C	C			C	C	C		C	A				C	C	C					C					C	A			A	C							C				
4H-CC, 0–5	30.70	30.75	VG	A	C	C			C	C			C	C	C		C					C	C	C					C					C	A			A	C							C				
5H-CC, 0–5	40.25	40.30	VG	A									C									C												C	A			A	C							C				
6H-CC, 0–5	49.47	49.52	VG	A																		C	C											C	A			A	C							C				
8H-CC, 0–5	68.68	68.73	G	A		C							C								C	C	C				C		F	C				C					C							C	C			
11H-CC, 0–5	97.10	97.15	G	C						F																								C																		
10H-CC, 0–5	87.71	87.76	G	C		C							F							C		C	C	C						F				C					F							C			F	C		
12H-CC, 0–5	106.73	106.78	G	C		F	F						F				C					C		C					F		F					F	F		F								F	C	F	
14H-CC, 0–5	125.75	125.80	P	F					F								F																							C							F					
16H-CC, 0–5	144.59	144.64	P	F					C						F		C		C							C								F						C					C	F				F	C	
17H-CC, 0–5	153.95	154.00	G	C							F						C																	F						C	C									F	F	
24X-CC, 0–5	219.34	219.39	VG	A						C								F				C	C																A	C				C							
25X-CC, 0–5	228.92	228.97	VG	A																		C	C																A	C				C							
26X-CC, 0–5	238.46	238.51	VG	A																		C	C																A	A				C							
29X-CC, 0–5	267.34	267.39	VG	A																		C	C																A	A				C							

Table T7. Benthic foraminiferal faunal counts, Hole U1414A. (Continued on next two pages.)

Core, section, interval (cm)	Depth (mbsf) Top	Depth (mbsf) Bottom	Preservation	Group abundance	*Alabamina* sp.	*Anomalinoides* sp.	*Astacolus* sp.	*Bolivinellina translucens*	*Brizalina ordinaria*	*Brizalina* spp.	*Brizalina subaenariensis*	*Buccella* sp.	*Bulimina alazanensis*	*Bulimina mexicana*	*Bulimina* sp.	*Cancris oblonga*	*Cassidulina carinata*	*Chilostomella oolina*	*Chrysalogonium* sp.	*Chrysalogonium* spp.	*Cibicides* sp. 1	*Cibicides* spp.	*Cibicidoides bradyi*	*Cibicidoides incrassatus*	*Cibicidoides mckannai*	*Cibicidoides pachyderma*	*Cibicidoides* spp.	*Fontbotia wuellerstorfi*	*Cribostomoides* sp.	*Cushmanina striatopunctata*	*Dentalina* sp.	*Discorbinella* spp.	*Eggerella bradyi*	*Eggerella* sp.	*Ellipsoglandulina* sp.	*Epistominella smithi*	*Epistominella* sp.	*Fissurina* spp.	*Fursenkoina* sp.	*Gavelinopsis praegeri*	*Globobulimina affinis*	*Globobulimina auriculata*	*Globobulimina* sp.	*Globobulimina* spp.	*Globocassidulina obtusa*	*Globocassidulina subglobosa*	*Gyroidinoides* spp.	*Hansenisca altiformis*	*Hoeglundina elegans*
344-U1414A-																																															
1H-CC, 0–5	1.84	1.89	G	C									2		1			18								1	9	2							1		2				8	6					9	
2H-CC, 0–5	11.77	11.82	G	C				1	1				1	2			2	12				1					1	1					1				1				8			1			
3H-CC, 0–5	21.40	21.45	G	C									1					3										1				1				5				3		1	4	1	4
4H-CC, 0–5	30.70	30.75	G	C													3	4										3		1						5				4	1		2	1		9
5H-CC, 0–5	40.25	40.30	G	C									1	5			3	2				1			2	8	1	3							3		4				5			2		4	1
6H-CC, 0–5	49.47	49.52	G	C										2				3				3				7		3					1				7				3			7		2
7H-CC, 0–5	59.27	59.32	G	F													1	1				1	1				1	4					1				7	1			1		4	2		3
8H-CC, 0–5	68.68	68.73	M	F						1				6			5	2				2				4	2	2							3	3							4				
9H-CC, 0–5	78.25	78.30	M	F			1			1				2		1	8	1				3				8	1	3					1	1			2				2	4			3	1	11
10H-CC, 0–5	87.71	87.76	M	F									3	8			11	1								3		4		1					1		10				4			1		1	7
11H-CC, 0–5	97.10	97.15	M	F			1							2			2	4				4	1			3		5				1								1		1			3	5
12H-CC, 0–5	106.73	106.78	M	F									1	6			10	3					2					4		1	1	1	2				5	1			5	1		13	3	1	3
13H-7, 0–5	115.95	116.00	G	C										7			14						1			9		5				1				3							2	2	18	13
14H-CC, 0–5	125.75	125.80	G	F										3			13				1		6				1	3								6						1			13		
15H-CC, 0–5	135.09	135.14	G	C									3	3								6	16					4			7		3			3							5	1		
16H-CC, 0–5	144.59	144.64	M	F		1				1		1	9	2								1	3					3			1	2	2						4			1	1	2	
17H-CC, 0–5	153.95	154.00	M	P	1					1			13	2							1		3								1		1				8						3	2	1	
18H-CC, 0–5	162.08	162.13	M	C								2	5				1					4					3				4			1	1	2	4						4	3		
19H-CC, 0–5	171.68	171.73	M	C									28	1				1				2	6			1	10				1	2				10	4						7	4		
20H-CC, 0–5	181.05	181.10	M	C		1							14	2					2			15				2	5									4	5						13	3	3	
21H-CC, 0–5	191.40	191.45	M	F		1				2			2	1					4		1	11	1			8	2	2				3		4		1		3						26	2		
22H-CC, 0–5	199.65	199.70	M	R										4								8				8	4	8				1			1		10	4						9	6		
23X-CC, 0–5	209.48	209.53	M	C																		6	7			2		3				1			1	4	3	1						9	3		
24X-CC, 0–5	219.34	219.39	M	C		1															10		10				1	3				1		3			8	6				1			5	4		
25X-CC, 0–5	228.92	228.97	M	C			1						9						1			14	4					3	1								2							13	1	11	
26X-CC, 0–5	238.46	238.51	M	C			1						9						1			14		1			4	3						2			2						13	1	11	
27X-CC, 0–5	248.15	248.20	P	P																	1		8	1			16	8						1		2	1						7	3		
28X-CC, 0–5	257.28	257.33	M	C									1						2								18	9								1	2						20	2	12	
29X-CC, 0–5	267.34	267.39	M	F							1								2				3				22	20			1			2			6						6	3		
30X-CC, 0–5	277.12	277.17	P	F							1										13		2				18	12						1			2					1	13	3	1	
31X-CC, 0–5	286.77	286.82	P	F									18	1									1				41	9			2			1		1							18	8		
32X-CC, 0–5	290.92	290.97	M	C									3									2	5				11	16								2	2							19	2		
33X-CC, 0–5	297.18	297.23	P	R		4																	2				37	10									4					2	19	5		
34X-CC, 0–5	303.06	303.11	P	F									6	9									1				18	1			1		1	1			1						5	2		

P/B = planktonic foraminifer/benthic foraminifer ratio. Preservation: G = good, M = moderate, P = poor. Abundance: C = common, F = few, R = rare, P = present.

Table T7 (continued). (Continued on next page.)

Core, section, interval (cm)	Depth (mbsf) Top	Depth (mbsf) Bottom	Preservation	Group abundance	*Karreriella bradyi*	*Karreriella* sp.	*Laevidentalina aphelis*	*Laevidentalina* sp.	*Lagena hispidula*	*Lagena* spp.	*Lagena striata*	*Laticarinina pauperata*	*Lenticulina* sp.	*Martinottiella* sp.	*Melonis affinis*	*Melonis* sp.	*Mucronina acuta*	*Myllostomella fijiensis*	*Myllostomella* spp.	*Nodosarella* sp.	*Nodosaria* sp.	*Nonionella* sp.	*Nonionella stella*	*Nuttallides umbonifera*	*Oolina globosa*	*Oolina* spp.	*Oridorsalis umbonatus*	*Orthomorphina* sp.	*Osangularia* sp.	*Planulina renzi*	*Plectofrondicularia* sp.	*Pleurostomella acuminata*	*Pleurostomella brevis*	*Praeglobobulimina ovata*	*Praeglobobulimina spinescens*	*Pseudoparrella* sp.	*Pullenia bulloides*	*Pullenia quinqueloba*	*Pullenia* sp.	*Pullenia subcarinata*	*Pyrgo depressa*	*Pyrgo murrhina*	*Pyrgo serrata*	*Pyrgo* sp.	*Pyrulina* sp.	*Quinqueloculina* sp.	*Rectuvigerina* sp.	*Rutherfordoides mexicanus*	*Scallopostoma ovicula*
344-U1414A-																																															
1H-CC, 0–5	1.84	1.89	G	C				1		2	2	5		3	1																		5			2		1					1						
2H-CC, 0–5	11.77	11.82	G	C								1		1	8								1				6						8	1		4								4			
3H-CC, 0–5	21.40	21.45	G	C			1	1		1					11								1				3						19		1	2			3		1		1				
4H-CC, 0–5	30.70	30.75	G	C											17																		8						1		10		1	1				
5H-CC, 0–5	40.25	40.30	G	C											15								2				1						3	1		2			2		1			1			
6H-CC, 0–5	49.47	49.52	G	C				1		2		5		1	1												5						17								8		1					
7H-CC, 0–5	59.27	59.32	G	F						1		1			12								2				2						8			3			3		3			1		2		
8H-CC, 0–5	68.68	68.73	M	F								1		1	6												6						7	1		1			1		6	1		1				
9H-CC, 0–5	78.25	78.30	M	F					1	1					1												5						12	3		2					4							
10H-CC, 0–5	87.71	87.76	M	F				1	1	4					5												3						5			6			1	2	16							
11H-CC, 0–5	97.10	97.15	M	F						1		1			2												5						7	4		1					4	1		2				
12H-CC, 0–5	106.73	106.78	M	F			1			2					2												5						4	6		5					4	1	1			14		
13H-7, 0–5	115.95	116.00	G	C								5																					1			1					1							
14H-CC, 0–5	125.75	125.80	G	F				4	2	1		5			10			2				1					1					1			2					5	1						
15H-CC, 0–5	135.09	135.14	G	C			2		1	1		5	1	2	15				1						1		1	1				7	2		2		3			5		3					3
16H-CC, 0–5	144.59	144.64	M	F			2	3	1		3	2		1	9	2	1								2		2									1							1				
17H-CC, 0–5	153.95	154.00	M	P			2		1			9			9												2					3		1		13											
18H-CC, 0–5	162.08	162.13	M	C			3	1								6				1							1					1			14	1	3									
19H-CC, 0–5	171.68	171.73	M	C			1					7		2	2	3		1				2		1	1	3	2			1		4			10	1	2					1				
20H-CC, 0–5	181.05	181.10	M	C			2					7		1	1	2		1	2	1							13		1			2			1	6						1				
21H-CC, 0–5	191.40	191.45	M	F			5	1				7			7	1			2		4				1	2	2					5			1						1	3	2			
22H-CC, 0–5	199.65	199.70	M	R			2					9		2	5			3									7					4	1			4		2			1		2			
23X-CC, 0–5	209.48	209.53	M	C				1		5		5			1				2								7					1	1			9			2		1					
24X-CC, 0–5	219.34	219.39	M	C				3	1			5	2	1	7			1			4				2				2				10			2			2			1	1			
25X-CC, 0–5	228.92	228.97	M	C			1					5		3	1	4		1					3				5			1		11	1			7		1								
26X-CC, 0–5	238.46	238.51	M	C				1				5		3	1	4		1					1				5			1		3	1			7		1								
27X-CC, 0–5	248.15	248.20	P	P	2		1	3		1		3	2	2	1	2		1	3		2		3				4			4		6				2			4							
28X-CC, 0–5	257.28	257.33	M	C		1	2					15	4	3	5					1	1		1		3		2			5		1	5			8										3
29X-CC, 0–5	267.34	267.39	M	F			1	3			2	13				4		1	2		1									2		5	1			6			3							
30X-CC, 0–5	277.12	277.17	P	F				1				3	1		3	7											12			7		3							2							4
31X-CC, 0–5	286.77	286.82	P	F			2	2				1		2		10											2			6		2				6			1							1
32X-CC, 0–5	290.92	290.97	M	C			1					7	1		3	2		6	3	1							2			1		2							1							
33X-CC, 0–5	297.18	297.23	P	R			3					2	1		10				4								3			9						1							1				
34X-CC, 0–5	303.06	303.11	P	F				7		4		1			12			3	1	1							4			12		1														

Table T7 (continued).

Core, section, interval (cm)	Depth (mbsf) Top	Depth (mbsf) Bottom	Preservation	Group abundance	*Sigmoilina obesa*	*Sigmoilopsis schlumbergeri*	*Sigmopyrgo vespertilio*	*Siphonina* sp.	*Siphonodosaria ketienziensis*	*Siphonodosaria lepidula*	*Siphonodosaria* spp.	*Siphotextularia* sp.	*Siphouvigerina ampullacea*	*Sphaeroidina bulloides*	*Spiroplectinata annectens*	*Spirosigmoilina distorta*	*Spirosigmoilina pusilla*	*Spirosigmoilina tenuis*	*Stainforthia complanata*	*Stainforthia* sp.	*Textularia* spp.	*Trifarina carinata*	*Triloculina* sp.	*Uvigerina auberiana*	*Uvigerina* cf. *senticosa*	*Uvigerina peregrina*	*Uvigerina* sp.	*Valvulineria glabra*	*Valvulineria* sp. 1	*Valvulineria* sp. 2	Others (*Rotaliina*)	Others (*Miliolina*)	Total	P/B
344-U1414A-																																		
1H-CC, 0–5	1.84	1.89	G	C									5	1										12	65	4					1		170	82.0
2H-CC, 0–5	11.77	11.82	G	C			2						9											8	49	1							136	81.4
3H-CC, 0–5	21.40	21.45	G	C			1							1					11				2	34	10	5				3		2	139	83.6
4H-CC, 0–5	30.70	30.75	G	C			1						1	3					5	1				35	7	10		4	13	3			154	93.5
5H-CC, 0–5	40.25	40.30	G	C			2					3	1						5					50	35	16							185	59.4
6H-CC, 0–5	49.47	49.52	G	C											1				4				1	38	2	3						1	130	92.0
7H-CC, 0–5	59.27	59.32	G	F			1					3							2					2	5	2		2			1		84	86.7
8H-CC, 0–5	68.68	68.73	M	F			1						1						1					46	6	24		1			2		149	90.1
9H-CC, 0–5	78.25	78.30	M	F								1							8				1	27	4	7	2	1				3	138	72.3
10H-CC, 0–5	87.71	87.76	M	F			2					3		1					10				1	22	19	6		2		2		3	170	90.5
11H-CC, 0–5	97.10	97.15	M	F								1	2						9				2	33	19	14		2					143	50.0
12H-CC, 0–5	106.73	106.78	M	F			2												15					11	3					2			141	75.0
13H-7, 0–5	115.95	116.00	G	C									3						3					74	12	23		1		3	1		203	60.4
14H-CC, 0–5	125.75	125.80	G	F					12										1					38	26					1			160	88.9
15H-CC, 0–5	135.09	135.14	G	C					1	5							4				3			6	22	10					1	1	160	60.0
16H-CC, 0–5	144.59	144.64	M	F			1			10	1	3	2				1							3	30	2							118	72.5
17H-CC, 0–5	153.95	154.00	M	P						13	1	1	7											5	15				1		4		124	86.5
18H-CC, 0–5	162.08	162.13	M	C						9	1	2	17				1		1						127	1							224	74.6
19H-CC, 0–5	171.68	171.73	M	C				1		5	1													1	35						1		165	64.7
20H-CC, 0–5	181.05	181.10	M	C						7	1		8											1	12	1							140	82.4
21H-CC, 0–5	191.40	191.45	M	F						6		2				7	1						1	4	7	7					2		155	72.6
22H-CC, 0–5	199.65	199.70	M	R						6			2								2			24	42					2			185	51.6
23X-CC, 0–5	209.48	209.53	M	C							6			2			2	1						16	49								151	21.6
24X-CC, 0–5	219.34	219.39	M	C						2														6	37	2							145	1.4
25X-CC, 0–5	228.92	228.97	M	C					1	1	1													3	29								139	24.7
26X-CC, 0–5	238.46	238.51	M	C					1	1														3	28								129	6.0
27X-CC, 0–5	248.15	248.20	P	P		1				8	2							2						1	3	1					1		113	28.0
28X-CC, 0–5	257.28	257.33	M	C					5		3														10						1		146	49.7
29X-CC, 0–5	267.34	267.39	M	F					2	3		1												7	24						6		153	69.6
30X-CC, 0–5	277.12	277.17	P	F							5														20						12		147	89.9
31X-CC, 0–5	286.77	286.82	P	F							4	1												1	19						6		167	92.9
32X-CC, 0–5	290.92	290.97	M	C		1						1		1								1		2	14						7		119	91.0
33X-CC, 0–5	297.18	297.23	P	R																				1	1		1				17		137	92.5
34X-CC, 0–5	303.06	303.11	P	F					4	6	1													34			2				8		148	92.1

Table T8. Pore fluid major element concentrations, Site U1414.

Core, section, interval (cm)	Depth (mbsf)	Volume (mL)	Salinity	pH	Alkalinity (mM)	SO_4 IC (mM)	SO_4 ICP (mM)	Cl IC (mM)	Cl titr. (mM)	Br (mM)	Na (mM)	K (mM)	Ca (mM)	Mg (mM)	NH_4 (mM)
344-U1414A-															
1H-1, 51–61	0.56	55	34.5	7.59	4.45	27.6	27.4	559	557	0.861	470	12.0	9.71	49.8	0.25
2H-1, 131–141	3.26	48	34.5	7.60	12.3	21.9	21.4	556	557	0.875	470	11.9	8.11	49.0	1.56
2H-3, 131–141	6.08	49	34.5	7.60	16.6	19.1	18.3	557	556	0.892	474	12.1	7.28	48.8	2.15
2H-5, 131–141	8.90	55	34.5	7.73	19.8	16.7	16.0	557	553	0.899	473	11.9	6.57	49.1	2.80
3H-2, 131–141	14.17	53	34.0	7.68	26.0	11.9	12.1	557	555	0.912	474	12.0	4.73	48.3	3.23
3H-5, 131–141	18.40	51	34.5	7.74	29.0	9.4	8.3	558	557	0.915	468	11.3	3.99	46.4	3.16
4H-2, 131–141	23.67	42	34.0	7.73	31.7	6.4	6.1	560	558	0.929	464	11.4	3.60	46.2	2.97
4H-5, 132–142	27.92	58	34.0	7.73	31.9	5.0	4.3	559	466	0.924	467	11.3	3.28	45.9	2.79
5H-2, 131–141	33.17	51	33.5	7.70	31.7	3.8	3.2	563	561	0.940	466	11.2	3.42	46.1	2.68
5H-5, 131–141	37.40	48	33.5	7.72	31.0	3.6	2.2	561	562	0.934	468	11.1	3.73	45.7	2.62
6H-2, 135–145	42.75	39	33.0	7.72	28.8	3.8	2.9	571	566	0.955	460	11.0	3.94	45.7	2.55
6H-5, 135–145	47.11	46	33.0	7.73	26.9	4.2	3.7	568	566	0.945	465	11.1	4.38	46.5	2.55
7H-2, 140–150	52.35	41	32.5	7.75	25.1	5.7	4.8	569	567	0.946	466	11.4	4.95	46.9	2.64
7H-5, 140–150	56.85	41	32.5	7.66	24.2	7.0	6.3	570	567	0.944	460	10.5	5.24	46.8	2.67
8H-2, 140–150	61.85	44	32.5	7.68	23.5	8.5	7.0	571	568	0.945	460	11.0	5.78	46.6	2.81
8H-4, 105–113	64.49	10	32.5	—	—	9.5	9.2	573	570	0.940	463	11.2	6.51	49.0	2.76
9H-2, 140–150	71.35	42	33.0	7.75	21.4	11.3	10.5	575	571	0.942	471	11.4	6.65	49.0	2.90
9H-5, 140–150	75.85	48	33.5	7.58	21.7	12.1	12.4	575	570	0.942	465	10.6	6.88	48.4	2.97
10H-2, 140–150	80.85	41	34.0	7.66	21.3	13.1	13.1	576	572	0.941	470	11.0	7.33	49.6	3.07
10H-5, 140–150	85.35	33	33.5	7.51	20.7	13.8	12.2	581	573	0.951	466	11.1	7.16	48.8	3.25
11H-2, 140–150	90.35	52	34.0	7.57	20.3	14.2	14.1	571	572	0.927	469	10.9	7.60	50.2	3.31
11H-5, 140–150	94.85	36	34.0	7.65	20.6	14.7	14.7	576	571	0.934	467	11.0	7.80	49.7	3.44
12H-2, 140–150	99.85	40	34.0	7.48	20.2	15.0	14.8	575	570	0.932	460	10.4	7.70	48.7	3.61
12H-5, 140–150	104.35	39	34.0	7.55	19.8	15.0	14.9	571	572	0.921	464	10.5	7.94	49.7	3.58
13H-2, 140–150	109.35	62	34.0	7.49	19.6	15.3	15.6	572	569	0.924	467	11.2	8.16	50.2	3.75
13H-5, 140–150	113.85	44	34.0	7.71	19.6	15.5	15.5	576	571	0.926	471	11.7	8.09	49.2	3.96
14H-2, 140–150	118.85	47	33.5	7.54	18.7	15.4	15.1	570	568	0.915	468	10.9	8.27	50.6	3.93
14H-5, 135–150	123.33	—	34.0	—	—	15.7	15.4	575	570	0.927	473	11.8	7.96	49.6	4.34
15H-2, 140–150	128.35	44	33.5	7.45	17.6	15.7	15.2	570	567	0.917	464	11.2	8.36	50.3	4.11
15H-5, 140–150	132.85	46	33.0	7.46	17.1	15.7	15.7	569	568	0.912	471	10.8	8.86	50.7	3.96
16H-2, 110–120	137.55	45	33.0	7.43	14.4	15.9	15.8	571	566	0.921	473	11.9	8.80	47.7	4.31
16H-5, 140–150	142.05	53	33.0	7.38	14.6	15.9	14.8	569	569	0.912	470	11.1	9.40	47.6	4.18
17H-4, 135–150	150.33	53	33.5	7.43	13.5	15.8	15.8	572	567	0.923	470	11.5	9.56	47.1	4.26
18H-5, 130–150	159.43	48	33.5	7.39	12.7	15.8	16.2	570	565	0.915	467	11.4	10.2	45.4	4.18
19H-3, 135–150	166.35	49	33.0	7.34	12.9	15.7	15.2	566	566	0.909	465	10.5	10.4	46.8	3.88
19H-6, 135–150	170.67	38	33.0	7.31	12.9	15.7	15.4	568	567	0.913	467	11.0	10.1	46.3	3.97
20H-2, 135–150	174.53	50	33.5	7.37	12.7	15.7	15.6	570	566	0.917	474	11.4	9.98	47.2	4.01
20H-5, 137–152	179.05	50	33.0	7.30	12.7	15.6	15.4	569	566	0.915	467	11.2	9.80	45.4	4.01
21H-3, 135–150	185.53	48	33.0	7.34	12.3	15.6	15.8	566	567	0.910	470	11.2	9.86	45.2	3.92
22H-6, 70–85	198.88	48	33.0	7.25	11.8	15.7	15.7	570	570	0.916	476	12.0	12.6	39.8	4.11
23X-2, 130–150	203.00	4	33.5	—	—	15.8	15.7	569	569	0.912	474	12.0	12.4	39.5	4.04
23X-5, 130–150	207.50	16	33.0	—	—	15.8	15.6	569	569	0.915	472	12.2	12.5	39.4	4.00
24X-4, 94–114	214.85	20	33.0	—	—	15.9	16.0	565	569	0.903	471	11.5	12.7	40.0	3.77
24X-6, 130–150	217.85	18	33.0	—	—	15.9	15.8	571	566	0.917	473	11.8	12.4	40.0	3.76
25X-2, 112–132	222.02	17	33.0	7.55	9.72	15.7	15.9	564	568	0.904	478	11.9	12.4	39.7	3.69
25X-5, 130–150	226.52	21	33.0	7.63	9.99	16.0	16.3	564	568	0.903	476	11.6	12.7	40.2	3.64
26X-2, 130–150	231.80	19	33.0	7.61	8.65	16.0	16.1	568	568	0.911	479	11.5	12.4	39.0	3.46
26X-5, 130–150	236.30	21	33.0	—	—	15.7	15.7	565	567	0.903	477	11.3	12.7	37.8	3.41
27X-3, 120–150	242.90	10	33.0	—	—	15.7	15.6	572	567	0.918	474	11.6	13.5	35.2	3.43
28X-4, 67–97	252.93	21	33.0	—	—	15.4	15.0	576	567	0.919	469	11.0	13.6	33.0	3.31
29X-2, 72–102	260.17	11	33.0	—	—	14.9	15.0	575	569	0.919	468	11.1	13.5	32.4	3.23
30X-2, 79–109	269.40	12	33.0	—	—	14.2	13.8	572	569	0.911	477	11.8	12.6	32.2	3.09
30X-4, 65–95	271.09	—	32.5	7.49	6.85	14.2	14.3	568	566	0.902	470	11.5	12.2	32.1	3.13
31X-2, 65–100	279.05	9	32.5	—	—	12.8	12.9	570	567	0.913	480	11.0	11.0	32.1	3.01
32X-2, 91–121	288.82	10	32.5	—	—	11.4	11.5	568	564	0.906	474	10.2	9.18	32.1	2.70
34X-1, 0–14	302.17	10	31.0	—	—	8.7	9.4	561	564	0.894	468	9.2	6.87	31.8	2.35
35X-1, 15–39	307.97	28	31.0	—	—	5.8	6.3	569	560	0.912	474	7.8	6.85	32.2	2.24
36R-2, 67–92	314.01	18	30.5	—	—	4.6	3.1	564	561	0.904	473	7.8	5.63	29.4	2.26
37R-3, 74–103	319.50	26	30.0	—	—	7.2	1.4	564	557	0.909	472	7.9	5.48	27.7	2.26
38R-1, 123–145	327.44	34	30.0	7.55	5.261	2.5	1.7	563	557	0.904	477	7.2	6.78	26.7	2.13
38R-2, 66–102	328.39	60	30.0	7.45	6.85	8.5	1.4	563	557	0.905	483	7.9	6.88	25.6	2.23
39R-1, 80–94	336.67	9	30.0	—	—	12.6	3.0	559	555	0.897	477	7.5	11.7	20.0	1.81
39R-1, 94–111	336.83	10	30.0	—	—	11.7		565	556	0.905					

IC = ion chromatograph, ICP = inductively coupled plasma–atomic emission spectroscopy, titr. = titration, — = not measured.

Table T9. Pore fluid minor element concentrations, Site U1414.

Core, section, interval (cm)	Depth (mbsf)	B (μM)	Li (μM)	Sr (μM)	Ba (μM)	Mn (μM)	Si (μM)
344-U1414A-							
1H-1, 51–61	0.56	474	27.3	84.5	0.48	53	573
2H-1, 131–141	3.26	535	18.9	81.3	0.70	4.8	574
2H-3, 131–141	6.08	576	16.6	78.6	1.18	2.2	580
2H-5, 131–141	8.90	570	15.7	78.9	1.19	2.0	636
3H-2, 131–141	14.17	606	18.6	73.5	1.82	1.4	664
3H-5, 131–141	18.40	607	19.6	69.5	1.13	2.8	672
4H-2, 131–141	23.67	617	20.2	68.8	1.86	3.2	676
4H-5, 132–142	27.92	642	21.5	69.7	1.35	1.2	720
5H-2, 131–141	33.17	581	21.4	70.9	1.60	0.6	695
5H-5, 131–141	37.40	581	20.9	70.0	2.40	0.5	702
6H-2, 135–145	42.75	548	21.7	73.6	1.86	0.2	691
6H-5, 135–145	47.11	529	21.4	74.7	2.19	0.4	699
7H-2, 140–150	52.35	515	22.9	75.8	1.75	0.6	725
7H-5, 140–150	56.85	507	23.8	82.2	1.75	1.3	745
8H-2, 140–150	61.85	475	25.2	78.2	1.13	2.8	739
8H-4, 105–113	64.49	443	25.4	85.1	2.57	6.1	636
9H-2, 140–150	71.35	444	28.8	84.5	0.94	4.2	738
9H-5, 140–150	75.85	422	30.6	85.3	0.73	6.2	763
10H-2, 140–150	80.85	404	34.0	88.9	0.84	8.5	775
10H-5, 140–150	85.35	389	36.3	87.4	0.83	6.4	695
11H-2, 140–150	90.35	376	39.4	91.6	0.74	6.3	816
11H-5, 140–150	94.85	368	44.1	94.9	0.90	7.0	850
12H-2, 140–150	99.85	369	47.2	93.1	0.72	7.1	881
12H-5, 140–150	104.35	364	51.2	93.6	0.96	6.8	851
13H-2, 140–150	109.35	352	57.6	96.2	0.73	7.9	902
13H-5, 140–150	113.85	364	61.4	95.8	0.69	7.8	932
14H-2, 140–150	118.85	323	67.9	102	0.74	6.4	839
14H-5, 135–150	123.33	325	71.5	98.0	0.90	3.8	829
15H-2, 140–150	128.35	315	79.7	104	0.85	3.1	925
15H-5, 140–150	132.85	306	84.7	110	0.79	2.8	881
16H-2, 110–120	137.55	291	85.7	105	0.78	1.5	945
16H-5, 140–150	142.05	299	92.8	115	0.80	2.2	997
17H-4, 135–150	150.33	315	107	131	0.92	2.7	1030
18H-5, 130–150	159.43	337	124	149	0.87	2.1	825
19H-3, 135–150	166.35	318	133	166	0.63	1.9	654
19H-6, 135–150	170.67	318	136	171	0.63	1.6	579
20H-2, 135–150	174.53	319	138	176	0.69	0.9	510
20H-5, 137–152	179.05	377	153	193	0.55	0.7	570
21H-3, 135–150	185.53	384	159.	217		0.3	631
22H-6, 70–85	198.88	431	169	267	0.96	0.3	1410
23X-2, 130–150	203.00	419	166	266	1.01	1.0	1380
23X-5, 130–150	207.50	430	170	279	0.97	0.6	1470
24X-4, 94–114	214.85	403	175	304	0.71	1.3	1450
24X-6, 130–150	217.85	393	175	306	1.21	0.9	1410
25X-2, 112–132	222.02	424	177	318	0.82	1.4	1510
25X-5, 130–150	226.52	420	182	346	0.83	1.4	1470
26X-2, 130–150	231.80	402	178	346	0.63	1.1	1450
26X-5, 130–150	236.30	413	180	358	0.62	0.8	1550
27X-3, 120–150	242.90	410	176	372	0.78	0.6	1630
28X-4, 67–97	252.93	417	175	402	1.17	0.4	1620
29X-2, 72–102	260.17	428	174	432	0.87	0.6	1520
30X-2, 79–109	269.40	428	170	468	1.15	0.3	1390
30X-4, 65–95	271.09	422	169	463	0.81	0.5	1280
31X-2, 65–100	279.05	426	174	478	0.72	0.4	825
32X-2, 91–121	288.82	431	179	489	0.69	0.2	734
34X-1, 0–14	302.17	408	148	494	1.13	0.2	612
35X-1, 15–39	307.97	358	157	710	2.32	0.2	641
36R-2, 67–92	314.01	385	132	711	4.68	0.3	558
37R-3, 74–103	319.50	413	118	861	17.56	0.3	611
38R-1, 123–145	327.44	374	111	942	17.17	0.6	563
38R-2, 66–102	328.39	447	111	908	12.86	0.2	629
39R-1, 80–94	336.67	450	103	904	9.36	0.2	708
39R-1, 94–111	336.83						

Table T10. Concentrations of methane in headspace gas samples, Hole U1414A.

Core, section, interval (cm)	Depth (mbsf)	Methane (ppmv)
344-U1414A-		
1H-2, 0–5	0.61	2.5
2H-2, 0–5	3.31	2.6
2H-4, 0–5	6.13	3.3
2H-6, 0–5	8.95	4.9
3H-3, 0–5	14.22	9.6
3H-6, 0–5	18.45	8.7
4H-3, 0–5	23.72	9.6
4H-6, 0–5	27.97	8.8
5H-3, 0–5	33.22	9.2
5H-6, 0–5	37.45	8.2
6H-3, 0–5	42.80	7.1
6H-6, 0–5	47.17	1.5
7H-3, 0–5	52.40	5.3
7H-6, 0–5	56.90	4.9
8H-3, 0–5	61.90	5.0
8H-5, 0–5	64.53	4.3
9H-3, 0–5	71.40	4.1
9H-6, 0–5	75.90	5.4
10H-3, 0–5	80.90	3.9
10H-6, 0–5	85.40	5.9
11H-3, 0–5	90.40	4.7
11H-6, 0–5	94.90	3.9
12H-3, 0–5	99.90	4.1
12H-6, 0–5	104.40	4.2
13H-3, 0–5	109.40	3.6
13H-6, 0–5	113.90	3.7
14H-3, 0–5	118.90	4.0
14H-6, 0–5	123.40	4.2
15H-6, 0–5	132.90	2.4
15H-3, 0–5	128.40	2.0
16H-3, 0–5	137.60	3.1
16H-6, 0–5	142.10	2.8
17H-5, 0–5	150.40	3.3
18H-6, 0–5	159.53	3.0
19H-4, 0–5	166.42	4.9
19H-7, 0–5	170.74	6.0
20H-3, 0–5	174.60	3.2
20H-6, 0–5	179.12	1.5
21H-4, 0–5	185.60	6.2
22H-7, 0–5	198.95	12.1
23X-3, 0–5	203.10	13.5
23X-6, 0–5	207.60	12.0
24X-5, 0–5	214.95	10.6
24X-7, 0–5	217.95	15.5
25X-3, 0–5	222.12	11.6
25X-6, 0–5	226.62	16.8
26X-3, 0–5	231.90	24.0
26X-6, 0–5	236.40	25.3
27X-4, 0–5	243.00	40.4
28X-5, 0–5	253.08	10.8
29X-3, 0–5	260.32	29.5
30X-5, 0–5	271.24	23.8
31X-3, 0–5	279.22	15.3
32X-3, 0–5	288.97	11.5
33X-1, 31–36	296.91	12.0
34X-1, 82–87	302.92	20.9
35X-1, 12–15	307.82	6.9
36R-3, 0–1	314.13	13.9
37R-5, 85–86	321.27	12.0
38R-2, 0–5	327.55	9.8
39R-2, 0–5	336.91	10.8

Table T11. Total carbon (TC), inorganic carbon (IC), total organic carbon (TOC), calcium carbonate, total nitrogen (TN), and C/N ratios, Hole U1414A. (Continued on next page.)

Core, section, interval (cm)	Depth (mbsf)	TC (wt%)	IC (wt%)	TOC (wt%)	$CaCO_3$ (wt%)	TN (wt%)	C/N ratio
344-U1414A-							
1H-1W, 49–50	0.49	2.22	0.334	1.89	2.79	0.226	8.35
1H-2W, 61–62	1.22	2.26	0.362	1.90	3.02	0.215	8.83
2H-1W, 87–88	2.77	2.54	0.868	1.67	7.24	0.180	9.29
2H-1W, 128–129	3.18	2.73	1.12	1.61	9.34	0.168	9.59
2H-3W, 129–130	6.01	2.49	0.754	1.74	6.29	0.176	9.86
2H-5W, 129–130	8.83	2.32	0.443	1.88	3.69	0.207	9.07
3H-2W, 129–130	14.10	2.75	0.592	2.16	4.94	0.220	9.81
3H-4W, 35–36	15.98	2.23	0.411	1.82	3.43	0.184	9.89
3H-5W, 129–130	18.33	1.94	0.271	1.67	2.26	0.196	8.51
4H-2W, 129–130	23.60	2.11	0.258	1.85	2.15	0.204	9.08
4H-4W, 41–42	25.55	1.69	0.439	1.25	3.66	0.159	7.87
4H-5W, 129–130	27.84	2.77	0.663	2.11	5.53	0.213	9.89
5H-2W, 130–131	33.11	2.64	0.549	2.09	4.58	0.219	9.55
5H-4W, 138–140	36.01	2.66	0.625	2.04	5.22	0.218	9.33
5H-5W, 129–130	37.33	1.98	0.285	1.70	2.38	0.203	8.35
6H-1W, 128–129	41.18	1.39	0.268	1.12	2.24	0.137	8.18
6H-2W, 133–134	42.68	2.03	0.676	1.35	5.64	0.204	6.64
6H-3W, 142–143	44.22	2.32	0.404	1.92	3.37	ND	—
7H-2, 138–139	52.28	2.20	0.741	1.46	6.18	ND	—
7H-4W, 0–0	53.90	2.23	0.296	1.93	2.47	ND	—
7H-5W, 136–136	56.76	3.15	1.44	1.71	12.0	ND	—
8H-2W, 139–140	61.79	1.75	0.590	1.16	4.92	ND	—
8H-6W, 112–113	67.15	3.43	1.53	1.90	12.8	ND	—
9H-2W, 138–139	71.28	2.98	1.39	1.59	11.6	ND	—
9H-4W, 34–35	73.24	1.99	0.712	1.28	5.94	ND	—
9H-5W, 124–125	75.64	1.58	0.542	1.04	4.52	ND	—
10H-2W, 69–70	80.09	1.52	0.435	1.09	3.62	ND	—
10H-2W, 69–70	80.09	1.50	0.582	0.92	4.85	0.111	8.27
10H-3W, 2–3	80.92	1.75	0.713	1.04	5.95	ND	—
10H-5W, 137–139	85.27	3.04	1.40	1.64	11.70	ND	—
11H-1W, 52–53	87.92	3.40	1.71	1.69	14.3	ND	—
11H-2W, 138–139	90.28	2.43	1.24	1.19	10.3	ND	—
11H-5W, 137–138	94.77	1.33	0.253	1.08	2.11	0.113	9.53
12H-2W, 125–126	99.65	2.08	0.873	1.21	7.28	ND	—
12H-3W, 102–103	100.92	1.97	0.782	1.19	6.52	ND	—
12H-5W, 138–139	104.28	2.64	1.39	1.25	11.6	ND	—
13H-1W, 110–111	107.50	1.72	0.457	1.26	3.81	0.124	10.1
13H-2W, 137–138	109.27	2.60	0.883	1.717	7.37	0.094	18.3
13H-5W, 133–134	113.73	0.72	0.191	0.529	1.60	0.049	10.8
14H-2W, 138–139	118.78	3.09	2.00	1.09	16.7	ND	—
14H-4W, 54–55	120.94	3.18	2.36	0.824	19.7	ND	—
15H-2W, 137–138	128.27	4.94	3.81	1.13	31.8	ND	—
15H-4W, 67–68	130.57	3.78	2.70	1.06	22.5	ND	—
15H-5W, 137–138	132.77	1.55	0.573	0.977	4.78	ND	—
16H-1W, 106–107	135.96	4.52	3.41	1.11	28.4	ND	—
16H-2W, 107–108	137.47	4.83	3.82	1.01	31.9	ND	—
16H-5W, 136–138	141.96	4.79	3.96	0.827	33.1	ND	—
17H-4W, 129–131	150.19	4.78	3.95	0.830	32.9	ND	—
17H-6W, 133–134	153.23	4.94	4.09	0.851	34.1	ND	—
18H-4W, 104–105	157.57	5.44	4.29	1.15	35.8	0.093	12.3
18H-5W, 127–128	159.30	6.46	5.63	0.832	46.9	0.061	13.6
19H-2W, 35–36	163.86	6.87	6.08	0.794	50.7	0.050	15.9
19H-3W, 133–134	166.25	7.04	6.16	0.883	51.4	0.054	16.3
19H-6W, 119–120	170.43	7.50	6.77	0.727	56.5	0.038	19.1
20H-2W, 120–121	174.30	8.07	7.28	0.786	60.8	0.035	22.5
20H-4W, 132–133	177.42	8.02	7.19	0.826	60.0	0.040	20.7
20H-5W, 134–135	178.94	8.49	7.71	0.781	64.3	0.033	23.7
20H-6W, 28–29	179.40	9.09	8.27	0.818	69.0	0.031	26.4
21H-3W, 131–132	185.41	10.19	9.38	0.814	78.2	0.018	45.2
21H-6W, 124–125	189.84	9.97	9.21	0.758	76.8	0.015	50.5
22H-3W, 2–3	193.62	9.93	9.22	0.709	76.9	ND	—
22H-6W, 69–70	198.79	7.13	6.50	0.626	54.3	0.023	27.2
23X-2W, 126–127	202.86	8.02	7.24	0.785	60.3	0.018	43.6
23X-3W, 148–149	204.58	10.98	10.13	0.849	84.5	ND	—
23X-5W, 122–123	207.32	9.98	9.05	0.929	75.5	0.018	51.6
24X-4W, 78–79	214.59	5.10	4.51	0.587	37.6	0.027	21.7

Table T11 (continued).

Core, section, interval (cm)	Depth (mbsf)	TC (wt%)	IC (wt%)	TOC (wt%)	$CaCO_3$ (wt%)	TN (wt%)	C/N ratio
24X-6W, 77–79	217.22	6.43	5.71	0.718	47.6	0.025	28.7
25X-2W, 110–111	221.90	8.14	6.82	1.32	56.9	0.030	44.1
25X-4W, 65–67	224.27	6.19	5.37	0.821	44.8	0.036	22.8
25X-5W, 119–120	226.31	4.41	3.33	1.08	27.8	0.058	18.7
26X-2W, 119–121	231.59	5.82	4.76	1.06	39.7	0.062	17.1
26X-3W, 104–106	232.94	4.78	4.08	0.697	34.1	0.043	16.2
26X-5W, 127–129	236.17	7.78	7.45	0.330	62.1	0.023	14.4
27X-3W, 114–115	242.64	6.31	5.38	0.927	44.9	0.047	19.7
27X-6W, 63–64	246.63	8.44	7.68	0.763	64.0	0.018	42.4
28X-4W, 59–61	252.70	10.00	9.22	0.785	76.9	ND	—
28X-5W, 144–145	254.52	10.23	9.39	0.839	78.3	ND	—
29X-2W, 55–56	259.85	9.38	8.53	0.855	71.1	0.011	77.7
29X-6W, 141–142	266.23	9.91	9.14	0.774	76.2	ND	—
30X-2W, 73–74	269.19	11.28	10.43	0.851	87.0	ND	—
30X-4W, 60–61	270.89	11.12	10.33	0.791	86.5	ND	—
30X-4W, 60–61	270.89	11.12	10.40	0.718	86.8	0.011	65.3
30X-5, 113–114	272.37	11.46	10.65	0.807	88.9	0.011	73.3
31X-2W, 63–64	278.85	10.91	10.16	0.746	84.8	ND	—
31X-6W, 81–82	284.53	11.49	10.64	0.848	88.8	0.021	40.4
32X-2W, 83–84	288.59	11.45	10.58	0.872	88.2	0.027	32.3
32X-3W, 14–15	289.11	10.89	10.16	0.729	84.8	ND	—
33X-1W, 33–34	296.93	11.23	10.38	0.849	86.6	ND	—
34X-1W, 33–34	302.43	5.67	5.08	0.590	42.3	0.028	21.1
35X-CC, 41–63	309.17	10.54	9.74	0.799	81.3	ND	—
36R-2W, 65–67	313.86	9.14	8.33	0.815	69.4	ND	—
36R-3W, 35–36	314.48	9.80	9.02	0.781	75.2	0.012	65.1
37R-4W, 40–72	319.67	9.48	8.71	0.772	72.6	0.023	33.6
37R-5W, 81–82	321.23	10.26	9.25	1.01	77.2	0.042	24.0
38R-1W, 120–121	327.30	7.88	6.86	1.02	57.2	0.082	12.4
38R-2W, 63–65	328.18	10.62	9.55	1.07	79.7	0.160	6.69
39R-1W, 79–80	336.59	6.30	5.49	0.81	45.8	0.111	7.27
39R-2W, 43–45	337.34	6.84	5.79	1.05	48.3	0.167	6.28
41R-1W, 40–43	355.60	11.66	10.46	1.20	87.3	ND	—
41R-2W, 106–107	356.99	10.35	8.17	2.19	68.1	ND	—
42R-1W, 25–26	360.35	8.58	6.90	1.68	57.6	ND	—
44R-1W, 69–71	370.49	12.79	10.57	2.22	88.1	ND	—

ND = not determined, — = incalculable.